Controlling the Epitaxial Growth of Graphene On Diamond Surfaces

Thesis

Submitted to

Aberystwyth University

by

Simon Phillip Cooil MPhys (hons)

In candidature for the degree of

Philosophæ Doctor (PhD)

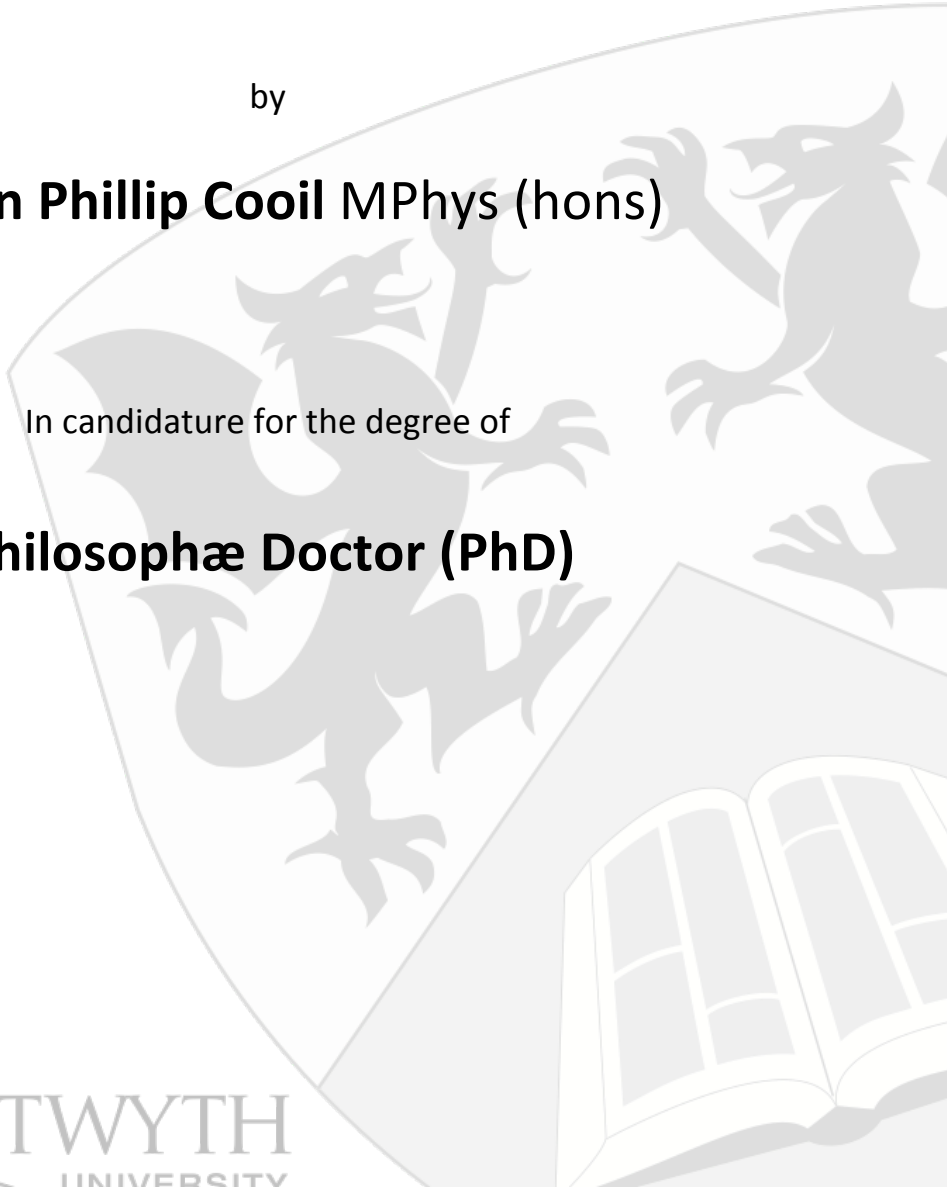

PRIFYSGOL ABERYSTWYTH UNIVERSITY

Dedicated to my parents Lesley and Jonothon,
for their love and unwavering support

Acknowledgements

I would like to take this opportunity to thank all those who have guided me through to this level of study, and helped me reach the completion of this thesis. The first is my supervisor Professor Andrew Evans, who I would like to sincerely thank for his animated and captivating discussions, which made the undertaking of this work a pleasure. I would like to extend once again my gratitude to Ass. Prof Justin Wells, who whilst not officially acting as a supervisor for the work, provided invaluable support as a colleague and friend. Dr Alexei Zakharov, Dr Yuran Niu and Dr Marco Banchi are commended for their boundless expertise and help during synchrotron beam-times, which although tiresome at times, provided some of the fondest moments of the study period.

Whilst working in Aberystwyth University I have had the pleasure of working with many people, a few of which in particular deserve mentioning. Dr David Langstaff for continued guidance on the instrumentation of the REES system. Dr Gruffudd Trefor Williams for helping me during the beginning of my studies. I would also like to thank research technician Mr. Matthew Gun and Mr Les Dean and Mr David Lewis of the electronics workshop for their support during these past years. My colleagues Mrs Rachel Cross, Mr Morgan Jones and Mr Steven Turner have made the years of study enjoyable and entertaining. Finally I would liked to thank my friends, of which I am fortunate and blessed to have too many to mention here.

Abstract

The Epitaxial nature of graphene growth on the diamond (111) surface has been investigated using real-time photoelectron spectroscopy (REES), Photoemission electron microscopy (PEEM), Angle resolved photoelectron spectroscopy (ARPES), low energy electron microscopy (LEEM) and low energy electron diffraction (LEED). Graphene regions were seen to co-exist on the reconstructed 2×1 diamond surface following a high temperature in vacuum anneal at ∼1000 °C. The graphene regions showed a π-band dispersion along K-M-K that matches well with other calculations and experimental results of quasi-free-standing graphene.

In the presence of a thin transition metal layer, the temperature at which the diamond surface undergoes conversion from sp^3 to sp^2 carbon is lowered. Here ordered films of Fe allow for the graphitisation of the diamond surface at ∼495 °C. The order of the Fe film allows for registry to be transferred between the diamond surface and resulting graphene formation on the surface. An important aspect of this work is, the application of real-time monitoring of in-situ processing. Here REES is applied as a technique, which allows for precise control of the amount of graphene grown. Whilst monitoring the growth with real-time imaging techniques such as LEEM allowed for investigation of the true growth optimum parameters. It was found that growth of graphene at 500 °C results in the formation large >100 μm regions which are strongly interacting with the substrate, displaying an n-type doping of ∼2.6 eV at the K-point. The growth of qasi-free-standing graphene began at 530 °C however the slow growth rate at this temperature resulted in the formation of small islands made up of many graphene layers and rotational domains. Growth at 560 °C allowed for lateral growth of free-standing monolayer regions across the sample surface. The grown material showed good registry to the substrate and displayed no sign of grain boundaries in LEED.

The same catalytic process has been applied to the surface of SiC 6H-(0001) and monitored using REES. Further control of the amount of graphene formed can by gained by the controlling the catalyst film thickness. A ∼0.75nm thick film of Fe is expected to grow precisely 1 monolayer of graphene, as a result of the formation of a complete FeSi layer which terminates the graphitisation process.

Contents

Chapter 1 – Introduction

Since the 2010 Nobel prize was jointly awarded to Novoselov and Geim, for the clear identification of the existence of graphene, a 2D crystal with a honeycomb arrangement of carbon atoms, and further detailing the fundamentally different characteristics of the charge carriers [1, 2], a 'gold-rush' of patents surrounding the material (for details see *Ref.*[3]) indicates just how influential, material scientists world wide expect graphene to be for future applications.

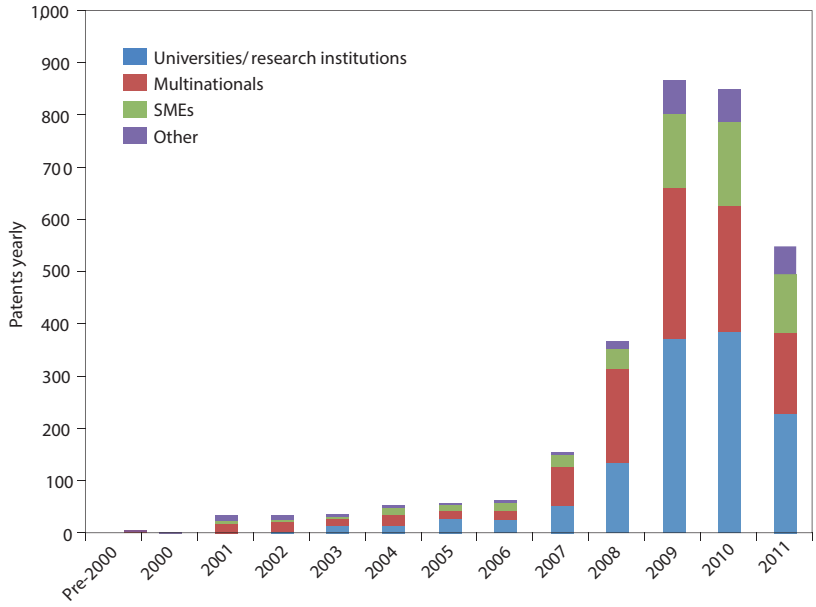

Figure 1.1 Development of graphene science and technology indicated by the number of patent applications by year. Patents can remain unpublished for extended periods therefore the last few years may be underestimated. Figure taken from *Ref.*[3]

Graphene is a single layer of graphite. Its electronic properties differ from that of its 3D counterpart, which is semi-metallic, by displaying a linear dispersion relationship of the charge carriers around the valence band maximum and conduction band minimum. In fact, for completely free-standing graphene the valence and conduction bands meet at

the Brillouin zone corners (K-point) and intersect at the Fermi-level, giving the charge carriers a massless characteristic that is best described by Dirac's relativistic equations of quantum mechanics. It is for this reason that this crossing is also known as the Dirac-point and the charge carriers as 'massless Dirac fermions'.

Alongside graphene's unique electronic properties, it displays a high optical transparency and surprising mechanical properties, which make it an ideal material for use in flexible displays and photovoltaics [4]. It posses a high thermal conductivity[5] and as a result of being a 2D material a high surface-to-volume ratio that makes it an ideal for gas sensing devices. Its ability to detect ultralow concentration of gas (down to <1ppb) has already been demonstrated [6].

Diamond represents another form of carbon that possesses extreme thermal, mechanical and electronic properties, and was recently suggested as a material that could one day supercede silicon in many high temperature, high voltage and high frequency applications [7]. The advent of CVD growth of diamond has enabled pristine samples to be manufactured in which the material properties, in contrast to natural diamonds, can be tailored to suit the necessary application[8-10].

In this work diamond is used as a substrate for the growth of graphene. On the bare surface, graphitisation, that is the solid-state transformation of the diamond surface atoms into graphitic regions, requires extreme temperatures in excess of 1200 K[11]. In the presence of a transition metal such as Ni, Co and Fe however, the graphitisation process is catalytically lowered [12, 13], and is the reverse of the process that forms

natural diamond in the Earth's molten mantle at high pressure and high temperature. This has been shown to allow the growth of high quality graphene on the metallized diamond surface [14], however a detailed understanding of the growth parameters, and resulting influence of the metal layer on the graphene, were necessary and are produced herein.

X-ray photoelectron spectroscopy has for a long time been the key tool in measuring the chemical state and evolving electronic properties of clean surfaces and interfaces. Its application in real-time has lead to further understanding of how diamond's electronic properties change with processing, such as temperature cycles, and with metal interfaces such as Al [15-17]. Here it is applied as a method to investigate and control the process of graphene production, however the technique lacks the special resolution necessary to investigate the true growth mode. Synchrotron based Photoelectron microscopy (PEEM) however represents a new frontier in the analysis of emitted photoelectrons. It is capable of producing 2D images in which the contrast is representative of the chemical state, and a lateral resolution down at the ~10 nm range provides the key spatial dimension to investigate the growth. This, along with an extremely broad range of imaging modes available in the modern SPELEEM, allows for imaging of the electronic band structure and structural properties with high precision[18] and in real-time. Angle resolved photoemission spectroscopy is still the most direct and best method used to investigating the electronic structure of solids and is therefore another key tool in the identification of graphene, as well as providing information on the energetics of the graphene-substrate interaction.

This thesis is divided in to 9 chapters. Following this introduction the techniques used throughout the following investigations will be presented. This also aids in disseminating some of the literature results indicated in chapter 3, with regard to the materials in use. Chapter 4 gives further details of the instrumentation, whilst chapters 5-7 detail and discuss the main experimental results obtained. Chapter 8 presents some other relevant work, and finally chapter 9 summarises the main conclusions of the thesis.

Chapter 2 – Techniques

This chapter aims to disseminate the theory behind the techniques used throughout this investigation, and to relay the intricacies of instruments used to perform them. Primarily the techniques employ the use of the photoelectric effect, although complementary electron beam techniques have also been used. Photoelectron spectroscopy (PES) provided one of the most revolutionary advances in understanding the underlying electronic properties of materials. Its reign has continued over the past seventy years thanks to advances in instrumentation and now photoelectron microscopy, with very good image resolution, has revamped the possibilities of the technique. Combining these with electron beam techniques such as low energy electron diffraction (LEED) and low energy electron microscopy (LEEM), it is now possible to image almost all of the information a surface scientist could require about the system/material under investigation.

2.1 Photoelectron Spectroscopy (PES)

In 1905, Einstein proposed a quantum theory of light, providing an explanation for Heinrich Hertz's earlier discovery of the photoelectric effect (1887). This led to one of the most revolutionary techniques used for the study of the electronic properties of materials. However it wasn't until the late 1960s when the first systems to accurately preform such measurements were developed by K. Seigbahn [19, 20]. Both discoveries led to Nobel awards, but furthermore led to understanding the fundamental principles of solid-state physics via experiments.

2.1.1 The principles of PES

The technique primarily allows for distinguishing the chemical composition and electronic structure at the surface of a sample. Monochromatic electromagnetic waves incident on the sample penetrate the surface and interact with electrons in the uppermost atomic layers. Several theoretical models have been proposed for treating the photoemission process, these are discussed at length in S. Hüfner's work [21, 22]. One of the earliest descriptions of the measured photoemission intensity is given in Berglund and Spicer's early work [23]. A two-stage process is described, this was later refined to a three-stage model, separating the processes involved in the initial excitation and movement of the excited electron to the surface of the material as follows:

1. The electron is excited into a higher state through absorbing the incident photons energy.
2. The electron travels through the crystal to the surface/vacuum interface.
3. The electron is ejected into vacuum.

The excited photoelectrons usually have a mean-free path length of a few nanometres within the sample, however if the photoelectrons escape into vacuum they can travel enormous distances in comparison. This allows hemispherical electron analysers (HSA's) that have large internal path lengths (typically in the region of 1 – 2m) to be utilised. This is a requirement of imaging the emitted electrons with high energy resolution.

Figure 2.1 shows the photoemission process; here electrons within then crystal are accelerated into vacuum via absorption of monochromatic photons of energy $h\nu$. The fastest electrons are those emitted come from the Fermi level where they had little binding energy and therefore a measurable kinetic energy of

$$E_{kin} = h\nu - \phi_s \qquad (Eqn - 2.1.1)$$

where ϕ_s is the sample work function, and B.E their binding energy (ground state energy) within the atom.

Those electrons that suffered energy loss due to inelastic collisions whilst traveling to the surface, contribute to the continuous energy spectra at low kinetic energies which cuts off at $E_{kin} = 0$, known as the secondary electron tail. Therefore electrons in vacuum have the kinetic energy distribution of

$$E_{kin} = \text{B.E} - h\nu - \phi_s + \text{Secondary electron continuum.} \qquad (Eqn - 2.1.2)$$

Since the analyser preforming the measurements has a work function of its own (analyser work function ϕ_A) a contact potential of $\phi_s - \phi_A$ arises between the sample and analyser due to the alignment of the Fermi levels (through electrical connection). Therefore the measured kinetic energy is offset by $\phi_s - \phi_A$ and is given by

$$E_{kin} = \text{B.E} - h\nu - \phi_s + (\phi_S - \phi_A)$$

(Eqn – 2.1.3)

$$\therefore E_{kin} = B.E - h\nu - \phi_A$$

(Eqn – 2.1.4)

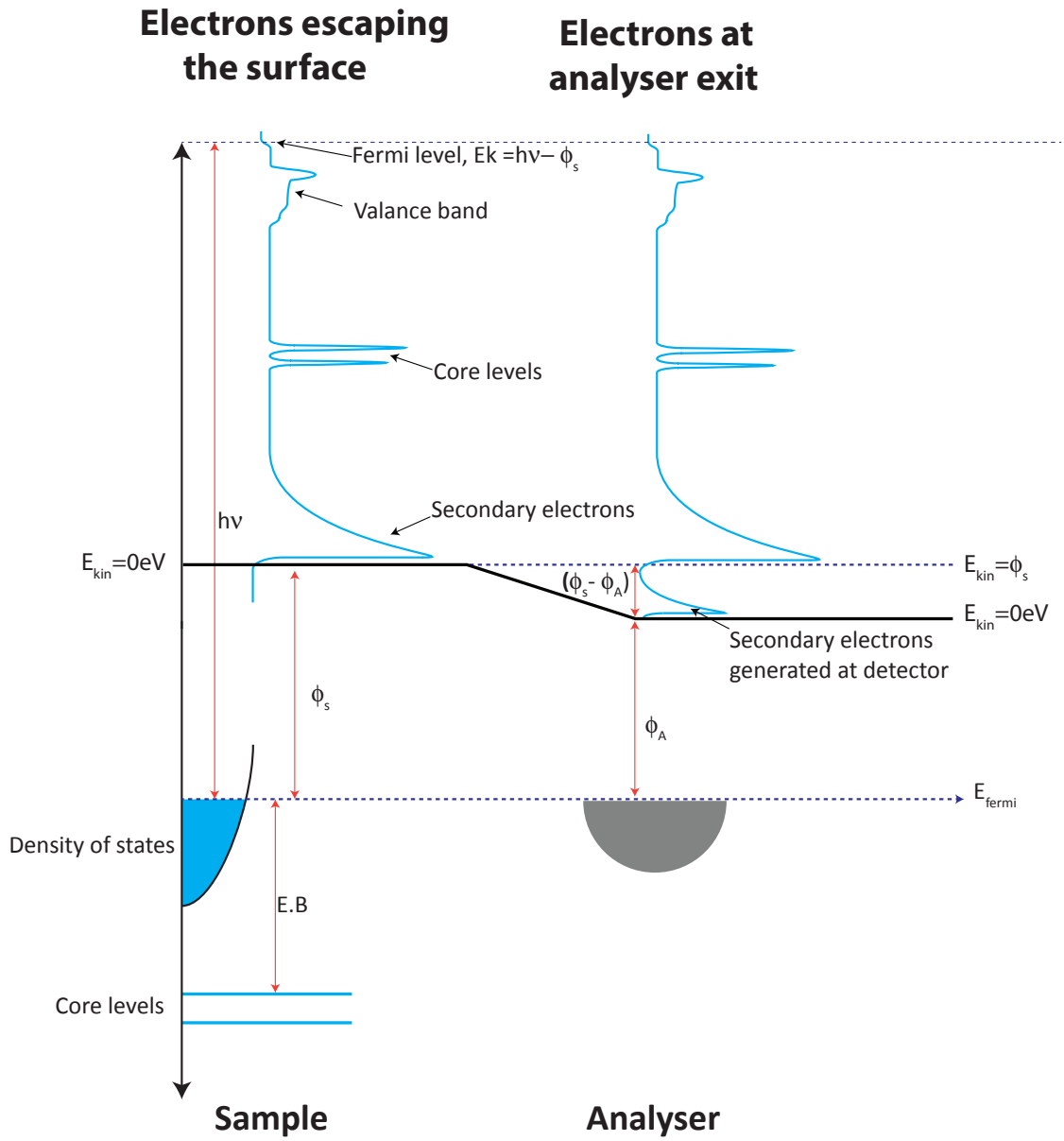

Figure 2.1 Shows the photoemission process and energy alignment between the sample and electron analyser.

2.1.2 The features of a XPS spectrum

Figure 2.2 shows an XPS survey spectrum ('widescan') taken from a single crystal (111) type 2b diamond. Primarily the well-defined peaks are due to electrons that were ejected with little scattering. Elemental composition is therefore readily available from analysing the kinetic energy of these emitted photoelectrons. Other spectral features arise due to the nature of X-ray generation in vacuum tubes (detailed in 2.2) such as satellite peaks, or the re-equilibration of the materials electronic states; Auger peaks and plasmon loss structure.

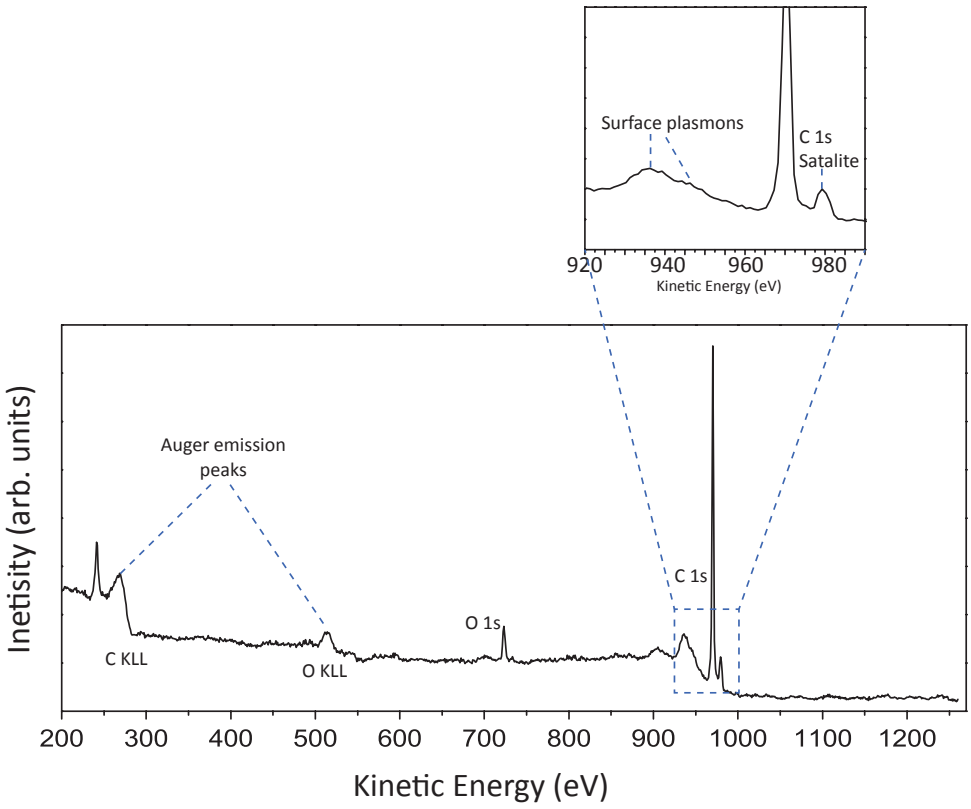

Figure 2.2 A widescan of an Oxygen terminated (111) single crystal diamond using MgKα X-ray lamp. The Mg anode has a small oxide layer which contributes a small amount of OKα X-rays generating the ghost C1s visible just left of the carbon Auger peaks.

2.1.2.1 Auger emission of electrons

The second most dominant spectral features arise due to the emission of Auger electrons. This process is due to the re-equilibration of the materials electronic structure post principle electron emission. Two possibilities exist for this renormalisation; the first gives rise to emission of an X-ray photon as an electron falls down to the hole left by the emitted electron. The second gives rise to emission of second electron; in this process the core level electron is emitted from the atom leaving a hole (for the case of carbon 1s or K-shell electron). An electron falling down from a higher shell (e.g. 2s, L-shell) to fill the hole releases enough energy in the process to emit an electron from the same or higher orbitals into vacuum.

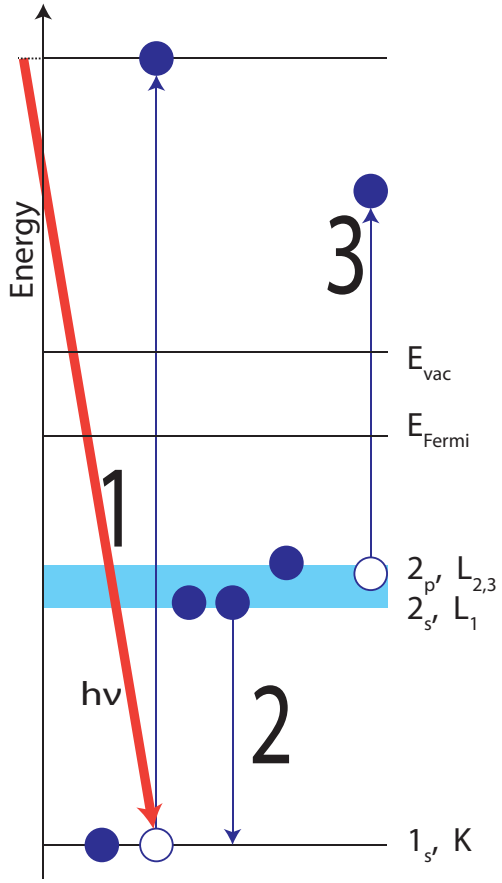

Figure 2.3 Shows the carbon KLL Auger emission process.

The benefit of these emitted electrons is that they have constant kinetic energy irrespective of photon energy expressed by

$$E_{kin} = E_{1s} - E_{2s} - E_{2p}$$

(Eqn – 2.1.5)

When labeling the Auger electron the convention is to use X-ray notation. In the case of carbon, the Auger peak (fig 2.2) is labeled C-KLL meaning that the electron hole was generated in the K-Shell, the transiting electron from the L_1 shell and the emitted Auger electron from the $L_{2,3}$ shell.

2.1.2.2 Satellites and Plasmon-loss peaks

The material under investigation is always a many-electron system; therefore excitation of the core level electrons must give rise to excitations in the remaining electronic configuration due to the Coulombic interaction. Besides the spectral features already discussed, this interaction of the excited electrons with the electronic structure gives rise to further peaks, these include; plasmon loss peaks, satellite peaks and spin orbit splitting.

Satellite peaks arise due to the non-monochromatic nature of X-ray generation in lab sources. An aluminium window is used to attenuate the non-preferential X-ray lines, however a small amount still make it through and generate their own photoelectrons. Since the measured kinetic energy is a function of hv, these peaks appear in the spectrum at different energies to those of the dominant excitation, despite originating from the same energy level. The intensity of these satellite peaks is weak in comparison to the main spectral features (insert fig 2.2), and can easily be removed within the software. Using fully monochromatic X-rays, like those achieved through synchrotron radiation,

completely removes these features. Alternatively a dirty (oxidised) X-ray anode, will also give rise to X-rays from electron transitions within oxygen. Figure 2.2 effectively shows two C1s photoelectron peaks. One excited with MgKα X-rays at 970eV and one with Okα 242eV on the lower kinetic energy side of the C-KLL Auger peak.

Plasmon peaks arise due to quantised oscillations in the valence electrons or free electrons in metals. Intrinsic and extrinsic effects give rise to these peaks as follows; the intrinsic effect is localised to the atom at which the core-hole is formed (due to the PES process described earlier)[24, 25], and is a result of the coupling between the positive core-hole and the oscillations of the valence states. This process happens simultaneously with the PES process, therefore the photoelectron is ejected with less energy. The frequency ω_p of these oscillations is different within the bulk than at the surface of the material. The emitted photoelectron will therefore be detected with an energy loss corresponding to $\hbar\omega_{pb}$ or $\hbar\omega_{ps}$ (or multiples for the higher harmonics) for the bulk and surface plasmon respectively.

Extrinsic effects relate to the coupling of the electric field of the excited photoelectron with the valence (free) electrons as it propagates to the material surface [24]. As before the electron loses energy relating to $\hbar\omega_{pb}$ or $\hbar\omega_{ps}$ (or multiples) for the bulk plasmon and surface plasmon respectively, however the process takes place away from the initial photoemission site. For diamond the bulk and surface plasmons lie at 34 – 36 eV from the main C 1s peak.

2.1.2.3 Spin-orbit splitting

Spin-orbit splitting is a consequence of electron orbital angular momentum l, and spin magnetic dipole moment, s of an electron within the atom. The result is a splitting of the electronic state where the total angular momentum is given by

$$j = |l \pm s| \text{ where } s = \frac{1}{2}$$

(Eqn – 2.1.6)

For light elements the spin orbit interaction is weak, however for larger atoms like those of transition metals, large splitting can occur. These result from *p*, *d* and *f* orbitals where l is non-zero. The ratio of the peak's area can be calculated by looking at the number of electrons in each degenerate level, given by:

$$R = \frac{2j_+ + 1}{2j_- + 1}$$

(Eqn – 2.1.7)

where j_+ & j_- correspond to the angular momentum determined by the positive or negative addition of the spin moment of the electron respectively as shown in equation 2.1.6.

Subshell	J Values	Area Ratio
s	1/2	n/a
p	1/2 3/2	1:2
d	3/2 5/2	2:3
f	5/2 7/2	3:4

Table 2.1 – Spin orbit splitting j values and respective area ratios

2.1.3 Photoelectron peak profile (Line shape)

The peak profile of the emitted photoelectron can be as informative as the recorded peak intensity and position. The peak profile is a convolution of the incident photon line shape

and contributions from the material such as, the core-hole lifetime and broadening due to atomic vibrations. Furthermore the analyser itself imparts some additional features to the emitted photoelectrons line shape. Traditionally a Voigt function line shape is used to approximate the semiconductor's photoelectron peak profile, whereas a Doniach-Sunjic line-shape is used for photoelectrons that originate within metallic atom orbitals. The Voigt function is a convolution of Gaussian and Lorentzian components and depends on a number of factors; excitation source, [where Kα X-rays have a Lorentzian nature and synchrotron radiation through an undulator having a Gaussian profile] and the intrinsic core-hole lifetime, which is assumed to be Lorentzian in nature. Some debate has been established in order to determine whether a sum of the two peak-shapes, or the product of each provides the truest form of the Voigt function, however the amount of noise present in the spectra is usually dominant in deciding which to use [26]. The Doniach-Sunjic (DS) line-shape is a Gaussian-Lorentzian peak with a modified tail on the higher binding energy side of the peak [27, 28]. This profile is commonly used for photoelectrons that originate within the atoms of a metal layer. As the photoelectron is excited through the energy levels some energy loss is occurred as discussed in 2.1.2.2. However the rich density of states at the Fermi-level for some metals (lower Z metals do not show this) means that the electron must travel through this large 'Fermi-sea' and therefore the photoelectron loses energy due to coulombic interaction, depending on the core-hole lifetime. The result is an asymmetry in the photoelectron peak where the DS line-shape takes into consideration the many possibilities for energy loss and provides a suitable fit for peak profiles.

2.1.4 Photoionization cross-section

An important parameter for quantification of XPS spectra is the photoionisation cross-section σ. It is defined as the total probability of ionisation of a system by electromagnetic radiation of a given energy. This means that the amount of electrons excited per unit time is a function of the amount of incident photons per unit area and includes all possible excitations of each orbital within the system under investigation. Fermi's golden rule relates the transition probability of electron excitation from its initial eigenstate $|i\rangle$ to a final state $|f\rangle$.

$$P_{i\to f} = \frac{2\pi}{\hbar}|\langle f|H'|i\rangle|^2\rho$$

(Eqn – 2.1.8)

Where $|\langle f|H'|i\rangle|$ is the matrix element of the perturbation for the Hamiltonian H' between the final and initial states. ρ is the density of states of the solid. Equation 2.1.8 effectively describes the lifetime of the generated electron hole within the system (aka the decay probability). It's worth noting that this equation holds true only if the initial state has not already been significantly depleted due to the photoionisation process. Scofield's early work contributed to providing a greater quantitative tool for analysis of XPS spectra by applying a relativistic Hartee-Slater model to calculate the absorption cross sections for most elements (Z= 1-92) at a number of incident photon energies [29, 30].

2.1.5 Electron attenuation length

The intensity of a photoelectron peak is a function of the depth from the surface from where it was generated; as the photoelectron has had to travel some way through the crystal before being emitted into the vacuum and its energy analysed. This is given by equation 2.1.9 at normal emission.

$$I = I_0 e^{\left(\frac{-d}{\lambda}\right)}$$

(Eqn – 2.1.9)

Where *I* is the measured substrate core level intensity, I_0 the intensity from the clean bulk substrate and d the depth of emission and λ the EAL.

During this journey due to inelastic scattering, additional intensity can be seen on the lower kinetic energy side of the spectrum. The length at which the probability of this scattering drops by e^{-1} is known as the electron attenuation length (EAL) [21] and is used as a measure of the surface sensitivity of the technique. EAL's are usually in the nanometer scale, and depend on the energy of the generated photoelectron (hence photon energy hv) and the properties of the material itself.

Calculation of the EAL is usually performed via the 'overlayer method', in which the intensity of the substrate core-level is attenuated by an overlayer of known material and thickness. Workers have determined many methods of calculating the effective EAL and by including experimental data have been able to produce databases that are capable of calculating the EAL of photoelectrons of known energy traveling through an elemental overlayer, aiding the use of XPS as a quantitative tool for analysis [31].

2.1.6 XPS quantification

From fitting the photoelectron spectra with the correct line-shape, knowing the photoionization cross-section and also the electron attenuation length of the substrate electrons as they pass through a deposited layer, the thickness of an over-layer can be calculated from the intensity of the substrate before and after deposition (equation 2.1.9). Due to the many experimental implications (i.e. moving the sample to another chamber for deposition and back, as well as the subsequent sample alignment involved) acquiring spectra before and after deposition can prove unreliable for quantification. A preferred method is therefore quantifying a single spectrum that contains both substrate and overlayer core levels (providing the overlayer is thin enough to do so) in order to provide a ratio of peak intensity to calculate thickness, or vise-versa.

For example, the ratio of Fe2p 3/2 and C1s for a monolayer of graphene on a thick iron substrate can be calculated as 42:1 respectively as follows:

Intensity of the C1s for monolayer graphene peak

$$I_{graphene} = 1 - e^{\frac{-d_{graphene}}{\lambda}} \cdot \sigma_{C1s}$$

A value of 1 is chosen to represent the infinite thickness (bulk) iron film intensity. The thickness of graphene as mentioned earlier is 0.345 nm [32], the cross section is given as 0.02228[30] for MgKα X-rays, and the EAL as 1.47 nm for $Fe2p_{3/2}$ electrons through a carbon overlayer (calculated in the NIST EAL database suite[31])

$$I_{graphene} = 4.66\times10^{-3} \text{ (arb. units)}$$

The intensity for the thick iron layer with graphene overlayer can be calculated as

$$I_{iron} = e^{\frac{-d_{graphene}}{\lambda}} \cdot \sigma_{Fe2p\ 3/2}$$

The cross section given for Fe2p photoelectrons at MgKα energy needs to be modified as only one component of the split peak is used yielding 0.2497. The EAL remains the same

$$I_{iron} = 0.1974 \text{ (arb. units)}$$

Giving

$$I_{graphene} : I_{iron}$$

$$= 1 : 42$$

2.1.7 The hemispherical electron analyser

The most important instrument of a well-equipped XPS laboratory is the electron analyser. Many principles exist for analysing the electron energy; these include (but are not limited to) time of flight analysis, retardation by a potential barrier and the dispersion through a deflecting field. Many designs also exist which include toroidal, cylindrical and hemispherical. For a full review seek the work of D. Roy and D. Tremblay [33]. Throughout this thesis one principle and design are in use, namely the photoelectron dispersion through a hemispherical deflecting field, as shown in figure 2.4. A '*SPECS Phoibos*100' hemispherical electron analyser is the primary analyser in the Aberystwyth materials physics laboratory.

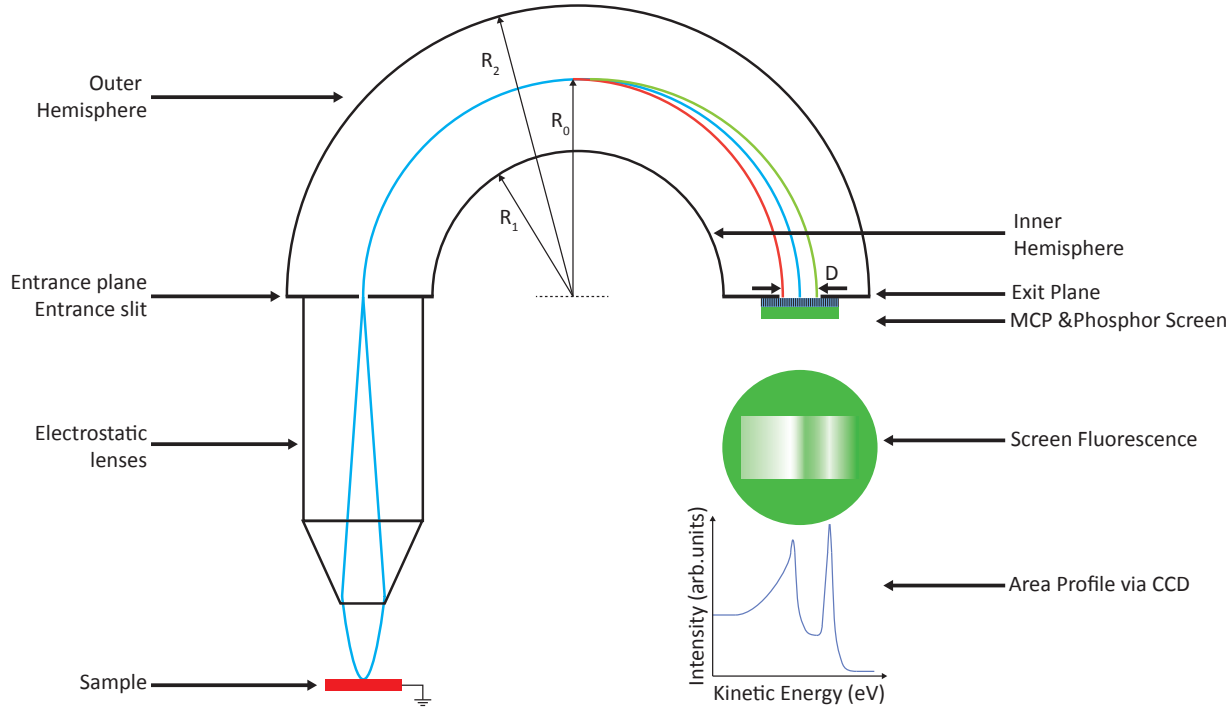

Figure 2.4 Shows the operating principles of a hemispherical electron analyser. R_1 and R_2 are the radii of the inner and outer hemispheres respectively, whilst R_0 the mean path of the electron beam. The energy of the higher (lower) kinetic energy electrons trajectory through the analyser is in green (red).

In this setup photoelectrons having been excited into vacuum, are collected via electrostatic lenses and focused onto the entrance plane of the analyser. Two negative potentials V1 and V2 are applied between the two concentric hemispheres R_1 and R_2 respectively, causing an electrostatic dispersion in the photoelectron trajectories, which are then imaged at the exit plane as shown in figure 2.4. Electrons that follow a perfect circular trajectory through the analyser are determined by the pass energy of the system. The pass energy E_p is dependent on the difference in potential ΔV applied between the two hemispheres and their radii as seen in equation 2.1.10 [34].

$$E_p = (-q)\Delta V\left(\frac{R_1 R_2}{R_2^2 - R_1^2}\right) \qquad (Eqn - 2.1.10)$$

As well as focusing the electrostatic lenses must therefore also decelerate all electrons down to the pass energy chosen, their kinetic energy is then related to the retarding potential necessary to decelerate them to this energy. With the analyser functioning in this way the spectrum is acquired in what is known as a fixed analyser transmission (FAT) (historically constant analyser energy (CAE)). In order to acquire a spectrum over larger energy ranges it is necessary to scan the potential applied to the lenses. The efficiency at which the lenses deliver different energies onto the focal plane of the analyser is called the transmission function, and differs for all lens modes of the analyser. The transmission function therefore plays an important role in quantifying the intensity of collected photoelectron peaks and calibration of these tables is vital. It is usually included in the data acquisition software and transferred to the analysis software for this purpose. Other operational modes such as constant retard ratio (CRR) use the electrostatic lenses in conjunction with varying the pass energy to detect electrons at a constant ratio to their kinetic energy. The 'retard ratio' is chosen so that the many low energy kinetic electrons can be imaged with the same intensity as weaker features. This mode is most useful when preforming Auger electron spectroscopy (AES) however none was performed so the FAT mode is always used when performing XPS.

The pass energy has an effect on the energy resolution of the imaged photoelectrons. Generally small pass energies will result in low transmission but a higher energy resolution, whereas large pass energies will result in high transmission at the cost of energy resolution. For scanned data the photoelectrons are retarded via the electrostatic lenses, down to the pass energy and then emitted through the hemisphere. The energy resolution of this mode is given by

$$\Delta E = E_p \left(\frac{R_1 R_2}{2R_0 + \alpha^2} \right)$$

(Eqn – 2.1.11)

Where R_0 is the mean radii of the two hemispheres and α is the angular half aperture of the electron beam at the entrance slit and is determined by the electrostatic lens system.

Once the electrons are at the exit plane they can then be detected via several methods. Historically the channeltron detector (a type of photomultiplier tube) was the optimum detector of choice as it has three significant figures of merit, namely dynamic range, detection efficiency and lifetime. Traits that manufactures are still utilising despite other emergent detector technologies. The biggest issue with a single detector mounted at the exit plane of the analyser is that all the electrons that don't contribute to the central trajectory of the system are lost, extending the amount of time taken to capture spectra. It was then realised that having more than one exit slit /channeltron configuration would allow the spread of the spectral features to be imaged more readily and with more energy resolution. Early systems focused on one exit slit either side of the central slit, which later developed into many slit systems such as those found in the SPECS Phoibos MCD-9 detector, which has four slits either side of the central exit slit [35]. However it was still apparent that only 7% of the available energy window will be counted at any time [36] .

Position sensitive detectors (PSD's) are detectors that lie along the exit plane and comprise many parallel detectors in a row, each capable of counting the number (or luminescent intensity) of impinging electrons on the detector, aiding the efficiency and therefore time of capturing spectra. Four main types of PSD are available, namely discrete

channel detectors, coincidence array detectors, charge division detectors and optical detectors that image the luminescence of a phosphor screens [37]. Throughout this investigation only the latter method has been used, however to discuss its merits over other technologies the first method 'discrete channel detectors' will also be discussed.

For these PSD's a microchannel plate (MCP) is used to amplify the number of electrons impinging on the detector after traversing the analyser to the exit plane. An MCP is an array of photomultiplier tubes (Channel electron multiplier CEMs) in parallel to each other. The tubes are usually made from glass where the inner walls are treated in such a way as to generate many secondary electrons, and semiconducting enough to replenish the supply of electrons, by applying a high potential across the tube (usually many kilovolts)[38].

As an electron enters the CEM it will collide with the wall and generate more electrons, as the tubes are in an array, the emission onto the detector is still specially resolved in energy. Therefore only a gain in the number of electrons detected is caused via the MCP, further enhancing the time efficiency of this method of detection. Typical gains are expected of between 10^3 and 10^5 counts. It is worth noting that vacuum pressure has an effect on MCPs where, at higher pressures the possibility of generating positive ions of gas molecules increases which themselves generate secondary electrons in the CEM causing a regenerative feedback of the device [38].

Following the MCP a series of discrete channel detectors may be used to count the number of spatially (energy) resolved electrons. Obviously the number of discrete channels available will have an additional gain in counting efficiency and much effort has been dedicated to just that. Early examples consisted of around 40 channels [36],

however cross talk between channels was limiting the number of channels per device. Combining the electron counting electronics and channels into a single device allowed denser arrays to be produced, including those created at Aberystwyth University which have over the years increased from 198 channels to a staggering 1526 channel detector (currently being characterized) [39-41].

Alternately a phosphor screen and charge coupled detector (CCD) may be used to image the energy distribution optically. This setup is seen in Figure 2.4 and is the primary method of detection for all experiments carried out in this investigation. Here the electrons that are generated in the MCP are incident on a phosphor screen in turn causing luminescence. A CCD is then used to image the fluorescence.

The Energy scale of the energy-dispersed electrons at the exit plane (energy window) is then related to the position at which they appear on the screen (pixel number of the imaging camera). As the pass energy changes, the size of the energy window changes (amount of dispersion from the perfect transmission trajectory *D* in figure 2.4) a relationship for the measured kinetic energy at the screen can be described by equation 2.1.12

$$\Delta E_k = D\Delta_{pixel}$$

(Eqn – 2.1.12)

The CCD is truly one of the greatest advancements of the 20th century. It was developed by Boyle and Smith in 1970 and has uses from memory storage to image sensing [42, 43]. Conceptually the device is quite simple and is made up of an array of metal oxide semiconductor (MOS) capacitors. These capacitors are photosensitive and therefore create a charge based on the intensity of incident light. A synchronised clock (transfer

clock) is used to march the induced voltage down the rows of the array and maintain the integrity of each packet. Changing the potential well height in sync with the transfer clock pushes/pulls the charge down the rows. It is then amplified and converted into a digital signal, which is then displayed as an image.

CCD detectors have a major advantage over the other detection methods discussed, as they provide two-dimensions of information depending on the electrostatic lens mode of the electron analyser. For standard XPS (transition lens modes), the two-dimensions are energy & real space taken along the axis of the entrance slit, which can be useful during focusing and quick sample alignment issues when illuminating with lab based flood X-ray sources. Alternatively in the angular lens modes the emission angle of the photoelectron ±15° can be recorded in one image and electronic band structure maps recorded in orders of magnitude less time than previously possible (see section 2.2).

2.1.8 Real-time electron spectroscopy (REES)

As mentioned previously the hemispherical analyser projects an energy window (dependent in size on E_p) of the dispersion of photoelectrons onto its exit plane, and spectra over larger energies are captured via scanning the potential applied to the electrostatic lenses that focus the electron beam onto the entrance plane of the analyser (FAT mode). Another mode of operation is available for analysis of photoelectron peaks by performing snapshot acquisition. In this mode; the lens settings and pass energy are chosen so that a single photo excited component of the spectrum (whether it be a photoelectron from a core level/ valence band, or an Auger electron) is imaged on the detector. The image is then integrated for a number of seconds and recorded (single snapshot). The process is repeated in quick succession allowing a component evolution to

be monitored during in-situ processing such as material deposition or heating. Evans *et al* have focused much attention on investigating in-situ processes with the use of REES and developed an electron counting position sensitive detector with 768 channels that is capable of rapid collection of photoelectron spectra, whilst showing large linearity across the detector.

2.2 Angle resolved photoelectron spectroscopy (ARPES)

Amidst the numerous techniques available via analyses of emitted photoelectrons, angle resolved photoelectron spectroscopy (ARPES) emerged as the most powerful and direct method used to map the electronic band structure of semiconducting crystals. Simply a measurement of the kinetic energy of the emitted low energy electrons is taken at various emission angles. Relating the emission angle of the photoelectrons with quasimomentum k (see 2.2.1) allows the electronic dispersion within the reciprocal lattice of the crystal to be mapped. This is possible due to the conservation of the photoelectron's momentum within the crystal as it enters the vacuum. Historically these measurements were performed with single dimension detectors such as a channeltron (±0.5° acceptance angle) where it was necessary to take many energy dependent curves (EDCs) in order to produce a singular momentum dependent curve (fig 2.5) and therefore very slow to map.

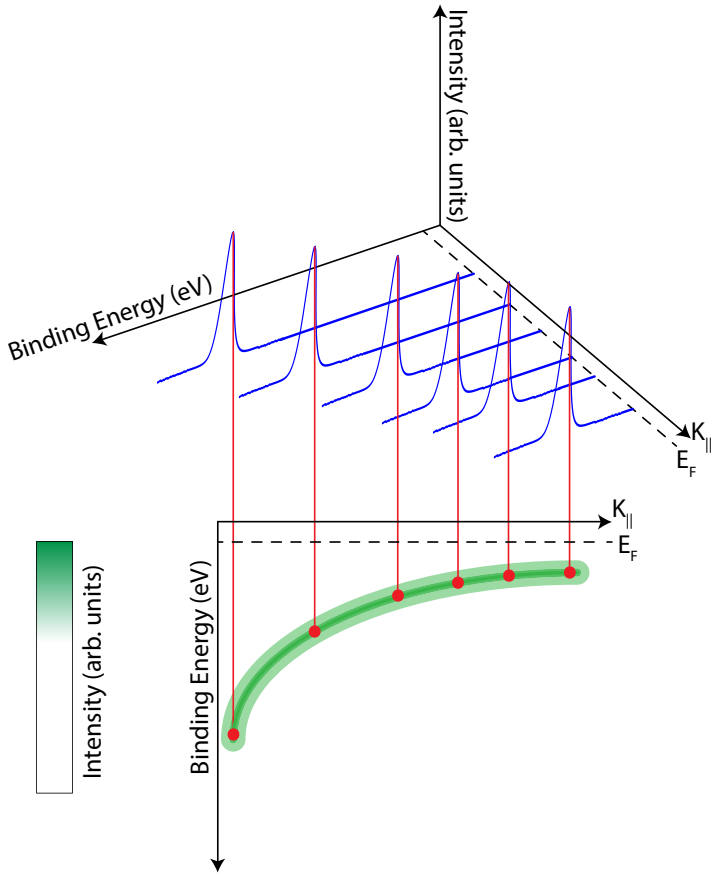

Figure 2.5 An illustrative representation of how ARPES was performed in many EDC sweeps to generate a singular MDC curve. Here each peak in EDC contributes to the MDC band. Where θ° is the emission angle, and E_f is the Fermi level.

However with the development of modern electron analysers, electron lens systems and 2D detectors it has been possible to drastically reduce the time necessary to take measurements, whilst improving the energy resolution of the technique. The technique requires precise and accurate control of the samples orientation in relation to the incident light and analyser. For this sophisticated sample manipulators are used that can control several rotational axes of the crystal. Figure 2.6 shows a schematic representation of the sample and electron analyser. The polar angle θ, is usually referenced to the manipulator axis and azimuthal angle ϕ, to a rotation around the surface normal. The analyser and lens configuration allow angular information to be

preserved (±β, where β lies along the entrance slit axis) in the non-energy dispersive plane of the analyser.

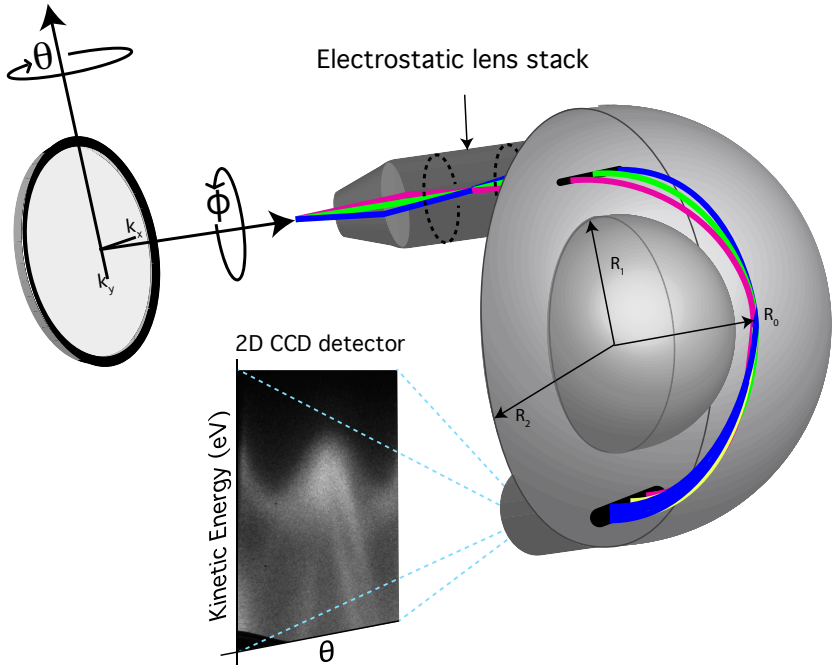

Figure 2.6 A schematic of the angular lens mode of the hemispherical electron analyser, here the CCD images the emission angle of the emitted photoelectrons whilst still maintaining energy dispersion.

2.2.1 Derivation of quasimomentum space 'k-space'

The photoelectrons momentum vector in vacuum *K* can be related to the momentum within the reciprocal lattice of the crystal if the emission angle and kinetic energy are known for it, as follows.

The magnitude of *K* in vacuum is given by

$$\vec{K} = \frac{\vec{P}}{\hbar} = \frac{\sqrt{2mE_{kin}}}{\hbar} \qquad (Eqn - 2.2.1)$$

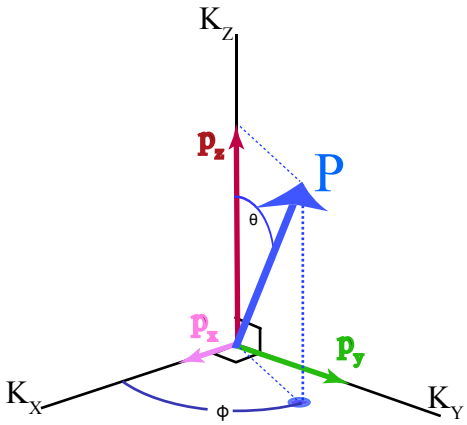

Figure 2.7 The emission vector P of a photoelectron and the angles and components corresponding to it.

From figure 2.7 it can be seen that P can be expressed in terms of its components p_x, p_y and p_z as

$$\vec{P} = \overrightarrow{p_x} + \overrightarrow{p_y} + \overrightarrow{p_z} \qquad (Eqn - 2.2.3)$$

Where

$$\overrightarrow{p_x} = \vec{P}sin\theta cos\varphi \qquad (Eqn - 2.2.3)$$

$$\overrightarrow{p_y} = \vec{P}sin\theta sin\varphi \qquad (Eqn - 2.2.4)$$

$$\overrightarrow{p_z} = \vec{P}cos\theta \qquad (Eqn - 2.2.5)$$

From equation 4.2.2 the momentum components K_x, K_y and K_z of K can be written as

$$\vec{K} = \overrightarrow{K_x} + \overrightarrow{K_y} + \overrightarrow{K_z} \qquad (Eqn - 2.2.6)$$

Where

$$\overrightarrow{K_x} = \frac{\sqrt{2mE_{kin}}}{\hbar} sin\theta cos\varphi \qquad (Eqn - 2.2.7)$$

$$\overrightarrow{K_y} = \frac{\sqrt{2mE_{kin}}}{\hbar} sin\theta sin\varphi \qquad (Eqn - 2.2.8)$$

$$\overrightarrow{K_z} = \frac{\sqrt{2mE_{kin}}}{\hbar} cos\theta$$

(*Eqn – 2.2.9)*

It is now possible to compare the momentum in vacuum K to the momentum within the crystal k by considering the symmetry conditions in plane and out of plane. The in-plane component (parallel to the sample surface) is given by

$$\overrightarrow{K_{\parallel}} = \overrightarrow{K_x} + \overrightarrow{K_y} = \sqrt{\overrightarrow{K_x^2} + \overrightarrow{K_y^2}}$$

(*Eqn – 2.2.10)*

where

$$\overrightarrow{K_{\perp}} = \overrightarrow{K_z}$$

(*Eqn – 2.2.11)*

Given that the translational symmetry of the surface potential is conserved across the surface boundary, the in-plane component of the photoelectrons momentum must be conserved, giving

$$\overrightarrow{K_{\parallel}} = \overrightarrow{k_{\parallel}}$$

(*Eqn – 2.2.12)*

From equation 2.2.10 and 2.2.7/8 it can be seen that the in plane component of the photoelectrons momentum can be fully determined by measuring the emission angle and kinetic energy as such

$$\overrightarrow{k_{\parallel}} = \frac{\sqrt{2mE_{kin}}}{\hbar} sin\theta$$

(*Eqn – 2.2.13)*

However the out of plane potential reaches a boundary at the surface and is therefore not conserved into the vacuum, therefore

$$\overrightarrow{K_{\perp}} \neq \overrightarrow{k_{\perp}}$$

(*Eqn – 2.2.14)*

That being the case it is possible to calculate the out of plane component by making some assumptions about the dispersion of the electron final states $E_f(\vec{k})$ that contribute to photoemission. Herein if the electron has large energy in relation to the vacuum level, a free-electron model can be used to approximate final state.

$$E_f(\vec{k}) = \frac{\hbar^2 \overrightarrow{k^2}}{2m} - |E_0| = \frac{\hbar^2 \left(\overrightarrow{k_\parallel^2} + \overrightarrow{k_\perp^2}\right)}{2m} - |E_0| \qquad (Eqn - 2.2.15)$$

Where E_0 is the ground state energy of the electron within the atom

Given that excited electrons are expressed by

$$E_f = E_{kin} + \phi \qquad (Eqn - 2.2.16)$$

And from rearranging equation 2.2.13

$$E_{kin} sin\theta = \frac{\hbar^2 \overrightarrow{k_\parallel^2}}{2m} \qquad (Eqn - 2.2.17)$$

The perpendicular wave vector can be expressed as

$$\overrightarrow{k_\perp} = \frac{\sqrt{2m(E_{kin} cos\theta + V_0)}}{\hbar} \qquad (Eqn - 2.2.18)$$

were V_0 is given by

$$V_0 = |E_0| + \phi \qquad (Eqn - 2.2.19)$$

V_0 is the inner potential of the material and is essentially a zero-order term expressing the potential. It can be approximated by taking data at different excitation energies and V_0 calculated with comparison to theory. The general rule is that direct transitions of $k_\perp$ can only occur at specific photon energies, therefore bands in k-space that disperse with hv

also have an electronic dispersion in k_z, and bands that do not are considered 2D in nature.

2.2.2 Building the dataset and Fermi-surface mapping

As described earlier the process of capturing a single 2D intensity dataset of $I(E_K, \phi)$ at various emission angles θ (orthogonal to ϕ) will allow the experimentalist to acquire a full map of the perpendicular electronic dispersion $K_{\parallel}$ by performing a polar scan (rotate the sample in front of the analyser in an angle orthogonal to the dispersive plane of the analyser). The now 3D data set of $I(E_K, \phi, \theta)$ exists and can be plotted as a cube of data. once K-warped (by applying the equations in section 2.2.1) looking down from the top of the data set gives both ϕ and θ, hence K_x and K_y also known as 'constant energy slice'. If the Fermi-level is chosen as the energy for this image, a Fermi-surface map can be produced. Relating this to the reciprocal LEED pattern (crystal orientation) enables the accurate mapping of electronic dispersion along key crystal axis.

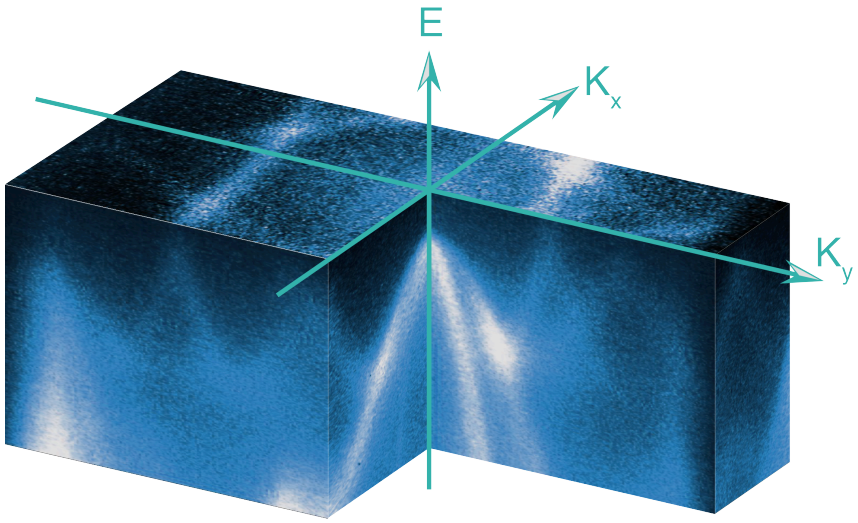

Figure 2.8 The 3D data cube of I (E,Kx,Ky). A rectangular cross section has been removed to show the energy dispersion.

2.3 Spectroscopic photoemission and low energy electron microscopy (SPELEEM)

A new form of microscopy usually always accompanies significant advances in surface science. From optical methods; optical microscopy or Raman microscopy through to the many electron-imaging techniques such as transmission electron microscopy (TEM) samples can now be imaged in a verity of ways leading to fundamentally new information. Adding lateral resolution to spectroscopic techniques has pushed them to what is now the rapidly expanding field of spectromicroscopy. Photoemission electron microscopy (PEEM), where X-rays are used as the primary illumination source, has emerged as a method of mapping the chemical composition of a surface by imaging the emitted photoelectrons (section 2.3.1). Alongside the development of PEEM, low energy electron microscopy (LEEM) where the sample is illuminated with an electron beam was also given considerable attention. The technique utilises the concentration of electrons into diffracted beams from crystalline samples, selecting one of these beams to form an image (section 2.3.2). It is capable of providing images at higher magnification and better resolution than its counterpart and is a vital tool for structural analysis. A surface feature, such as a grown nanostructure, can now be imaged containing information on the elemental composition, chemical bonding, electronic band structure, work function, crystallinity and surface terraces with resolutions of 10 – 30 nm depending on the technique and sample.

Modern instruments can be used in a variety of novel ways depending on the illumination source; whilst X-rays offer techniques such as energy filtered images for elemental

composition and local area XPS (microspectroscopy) through to more specialist techniques such as photoelectron diffraction, near-edge X-ray absorption fine structure (XAFS) (via digital subtraction of difference images), photoelectron emission angular distribution (PEEAD) and X-ray secondary electron emission microscopy (XSEEM). Illumination with an electron gun offers bright field / dark field LEEM, mirror electron microscopy (MEM) and small area low energy electron diffraction (μLEED). This section aims to give a brief background into the rise of the instrument and then discuss aspects related to the many imaging modes employed throughout this investigation.

2.3.1 Photoemission electron microscopy (PEEM)

Starting its development as system for imaging surfaces based on work function ϕ contrast, images were taken of the total yield of electrons from the surface when illuminated with monochromatic electromagnetic radiation. In 1933 Brüche successfully generated images of an array of holes in a zinc foil whilst irradiating it with UV light, a ×10 magnification at the image plane was achieved [44]. The necessary component of the setup was an axially divergent magnetic field, that enlarges the object under investigation (microscopy) whilst maintaining the energy distribution of the emitted photoelectrons (spectroscopy) hence often termed spectromicroscopy[45]. Advances to the technique were slow, principally as they followed advances in other fields such as ultra-high vacuum (UHV) and electron optics.

Poor lateral resolution was the primary concern for the technique as other imaging methods already boasted resolution in the sub 10 nm range. Advances in other electron

imaging systems such as TEM greatly enhanced the capabilities of these early PEEM instruments. Recknagel's work focused on calculating the errors associated in accelerating section of the lens system using full geometric-optical calculations, culminating in a calculation for the resolution factor of such instruments [46]:

$$\delta = \frac{e\varepsilon}{F} \qquad (Eqn - 2.3.1)$$

Where $e\varepsilon$ is the mean emission energy and *F* the field strength.

The introduction of multiple electrostatic lenses (Triodes) by W. Schaffernicht and the work of Boersch, who realised that the resolution factor was also determined by the spherical error of incident beam and by the diffraction on the imaging aperture, saw significant advances in resolution. A contrast aperture was added to the back focal plane of the instrument to significantly reduce the amount of diffraction by limiting the photoexcited electron emission angles (scattered electrons) that contribute to the image[47], (see figure 2.3.1). However it would be 25 years before the sub-micron resolution barrier was broken[48]. Further focusing of the electrostatic lenses (focused Triode) also increased the resolution [49] and was comparable to the magnetic lenses (homogeneous field calculations) initially used.

The use of X-ray illumination for spectroscopic imaging was suggested in the early 70s by J. Cazaux although initial investigations focused on imaging the secondary electrons over photoelectrons, as the yield is strongly dependent on the absorption cross section (excitation energy) in what is known as X-ray secondary electron emission microscopy (XSEEM) for E_{hv} ranging from 6 – 100eV[50]. XPEEM utilises the photoelectrons to form

images, however the high flux density available from synchrotron radiation, particularly from a beam-line equipped with an undulator insertion device [51], as well as energy filtering (with high energy resolution) are necessary for imaging with high lateral resolution. A tunable X-ray source also provides the surface sensitivity of the technique as described in 2.1.4 (EAL).

The energy resolution of XPEEM images has been shown to depend significantly on 'space charge effects'. These occur as a result of the high photon flux available at facilities such as synchrotron light sources or free electron lasers (FELs). The high intensity of electron emission from the sample generates mirror charges on the surface that broaden the energy resolution by as much as an eV. For example Bauer *et al* showed significant image blurring and energy broadening as a result of increasing photon flux. It was found that the amount of stochastic electron-electron interactions occurring as a result of the increasing coulomb interaction between the sample surface the area just above it between the objective lens was the cause[52].

The state of the art PEEM can be equipped with a number of different electron analysing instruments; from the already detailed hemispherical electron analyser, modified for better imaging capabilities[53, 54] to Wein-filters[55] and time of flight (TOF) analyser[56], which as well as high energy resolution must maintain the functionality and lateral resolution of the imaging section. Stigmators that correct for sample tilt and deflector lenses that allow scanning of the sample surface without moving its position are also in use[57]. Correcting the chromatic aberration of the accelerating objective lens has been developed [58-61] and an increase in resolution increase of 5 - 10 in comparison with

uncorrected instruments achievable. The resolution of the instruments is now approaching the theoretical limit of δ =2.5 nm [54]. Principally the aberration corrected instrument is equipped with a second magnetic beam-splitter in which the image is reflected off an electron mirror, removing aberration by symmetry. Commercial manufacturers such as Elmitec and Specs are now offering such instruments [62, 63].

2.3.2 Low energy electron microscopy (LEEM)

PEEM has proven to be an excellent tool for imaging surfaces; some structural information can be obtained if grazing incidence illumination is chosen (shadowing effects) however the use of electrons for microscopy can provide structural information at much higher resolution. As much of the development of LEEM coincided with the development of the PEEM and other electron microscopy techniques such as TEM and SEM, and has already been discussed previously; this section will begin by describing the interaction of low energy electrons with a crystal surface which has not yet been presented, before discussing how LEEM uses this effect to form a highly specially resolved image of the surface.

The kinetic energy of low energy electrons can be related to their wavelength by the use of the de Broglie relationship.

$$\lambda = \frac{h}{P} \qquad (Eqn - 2.3.2)$$

Where P is the same as equation 2.2.1 and *h* is planks constant. Electrons of 10-200eV have a wavelength of the order 1 – 2 Å or less, conveniently similar to the interatomic

spacing of crystal lattices. Diffraction will therefore occur as the electrons interact with the uppermost atomic layers of the crystalline solid, as the crystal lattice will act as a grating for the incident electron beam. Electrons, first generated by thermionic emission, are accelerated towards the sample surface at the chosen kinetic energy by a conventional electron gun. The interference pattern occurring as two electrons interact with each other due to a path difference *D,* after backscattering from adjacent lattice points on the surface at a distance '*a*' can be written as.

$$D = a\ sin\theta$$

(Eqn – 2.3.3)

Where θ is the angle of incidence to the surface plane. The intensity of the backscattered beams is dependent on electron wavelength λ, where it is at its most intense when the Bragg condition is met (equation 2.3.4). This occurs when the when the electron wavelength is equal to or an exact integer 'n' multiple of the path difference.

$$n\lambda = D\ sin\theta$$

(Eqn – 2.3.4)

As a surface is 2D in nature the crystal structure diffracts the electrons in two orthogonal directions. The interference of all the backscattered electrons from a large number of unit cells (≈1mm diameter electron beam in a conventional electron gun) then forms the diffraction pattern that is a reciprocal map of the surface structure.

The backscattered electrons in a conventional rear-view low energy electron diffraction (LEED) system are collected by a series of grids that retard secondary electrons and accelerate the backscattered electrons towards a luminescing phosphor screen. Focus of the illumination source and variable bias contrast meshes are also used to image the diffraction pattern at the screen at the best possible contrast between diffracted spots

and background intensity. Areas of poor crystallinitity will generally contribute to high background intensity in the diffraction pattern, as there will be a high percentage of other reflection angles from dislocations etc. As the wavelength of the incident electrons changes with kinetic energy so does the size of the reciprocal space pattern, and therefore the distance between spots.

In a Low energy electron microscope the high-energy electron beam, having been focused by a number of electron optics and sent through the beam-splitter and the objective lens, is decelerated down to a typical energy of 1-200eV. The backscattered electrons then pass through the objective lens for a second time where they are accelerated to the high energy of the imaging column again. The diffraction pattern that occurs as a result can be imaged at the back focal plane of the objective lens however no filtering of the secondary electrons is possible. This can be used to some extent however as an indication of the amount of light element adatoms present on the surface as they have large backscattering cross-sections at very low energies[64]. There are strong advantages to doing LEED in a low energy electron microscope; firstly, as the diffraction pattern is focused to the back focal plane and then accelerated to the fast energy E_0 of the electron imaging column, the final image has constant kinetic energy. Therefore the location of the spots does not change as the incident energy increases (and wavelength), making LEED-IV measurements much simpler. Secondly as the electron beam is bent in the magnetic beam-splitter, the specular reflected beam (00) spot is accessible (as well as all other spots). Finally inserting apertures in the illumination and imaging column means that LEED can be performed on surface regions as small as 10μm.

For the creation of a LEEM image a desired diffraction spot is chosen for imaging at the imaging plane of the system i.e all electrons that contribute to the chosen diffraction spot are imaged. This offers two possibilities; bright-field and dark-field LEEM imaging, depending on the choice of the specular reflected beam or any of the other beams respectively. The contrast in the image will therefore directly relate to the crystallinity and topography of the surface under illumination. If a dark-field LEEM image is formed by choosing the diffraction spot arising due to an atom that's undergone a surface reconstruction, then the contrast in the image will show exactly where the reconstruction occurs on the surface. The high intensity of backscattered electrons from the surface means that images can be collected in quick succession, making the technique particularly well suited to studying real-time dynamic surface processes such as film growth of sample annealing. In the latter case its worth mentioning that as a large potential difference lies between the sample and objective lens, the pressure in the sample chamber must remain very low, and can increase to dangerous levels at periods in some in-situ processing, during which time the acquisition must be stopped.

2.3.3 The SPELEEM instrument

A schematic of the SPELEEM used throughout this investigation is shown in figure 2.9 and a diagram representing the optical trajectories for different operational modes of the instrument in figure 2.10 They show the configuration of the instrument in which the sample, irradiated by normal incidence, high brilliance monochromatic synchrotron radiation from an undulator insertion device, is placed close to the objective lens and a bias of the order E_0 = -20kV applied between them (≈ 1.5 – 2mm). The large potential

difference between the sample and objective is the principal form of magnification for the specially distributed photoelectrons. This bias means that all electrons are imaged as fast electrons and therefore the difference between the sample bias and objective lens (start voltage) is varied to choose the desired kinetic energy for imaging. Located in the back focal plane of the objective lens is an aperture that can be inserted to select specific areas for analysis called the 'field-limiting aperture'. The first image is located within the beam-splitter in what is known as the intermediate image plane and transferred to the imaging column via the transfer lens TL where it is imaged in the secondary image plane behind the field lens FL (by focusing the back focal plane within it). It is at this point that a second aperture 'the contrast aperture' can be inserted to limit the angular distribution of electrons hence aberration. Until this point the optical path for each analysis mode is the same as shown in figure 2.9. The primary function of the intermediate lens IL is to focus the image (via the use of the first projector lens P1) or back focal plane into the entrance plane of the analyser for μARPES and XPEEM respectively. Placing the image at the entrance plane of the analyser (located at the analyser retarding lens R1), means that the back focal plane is energy filtered. Placing the image in the center of the analyser will provide an energy-filtered XPEEM image of the sample surface from EP1 just behind the second projection lens P2, and the diffraction image of EP2 at the dispersive plane of the analyser. Both XPEEM and μARPES require the use of the tunable energy slit to choose the energy window of the emitted electrons, which can be tuned between 0.5eV and few eV by adjusting its width. The analyser dispersive plane can be viewed by fully removing the energy slits and exciting the projection lenses in such a way as to image the dispersion at the screen, XPS spectra are collected in this way[65, 66].

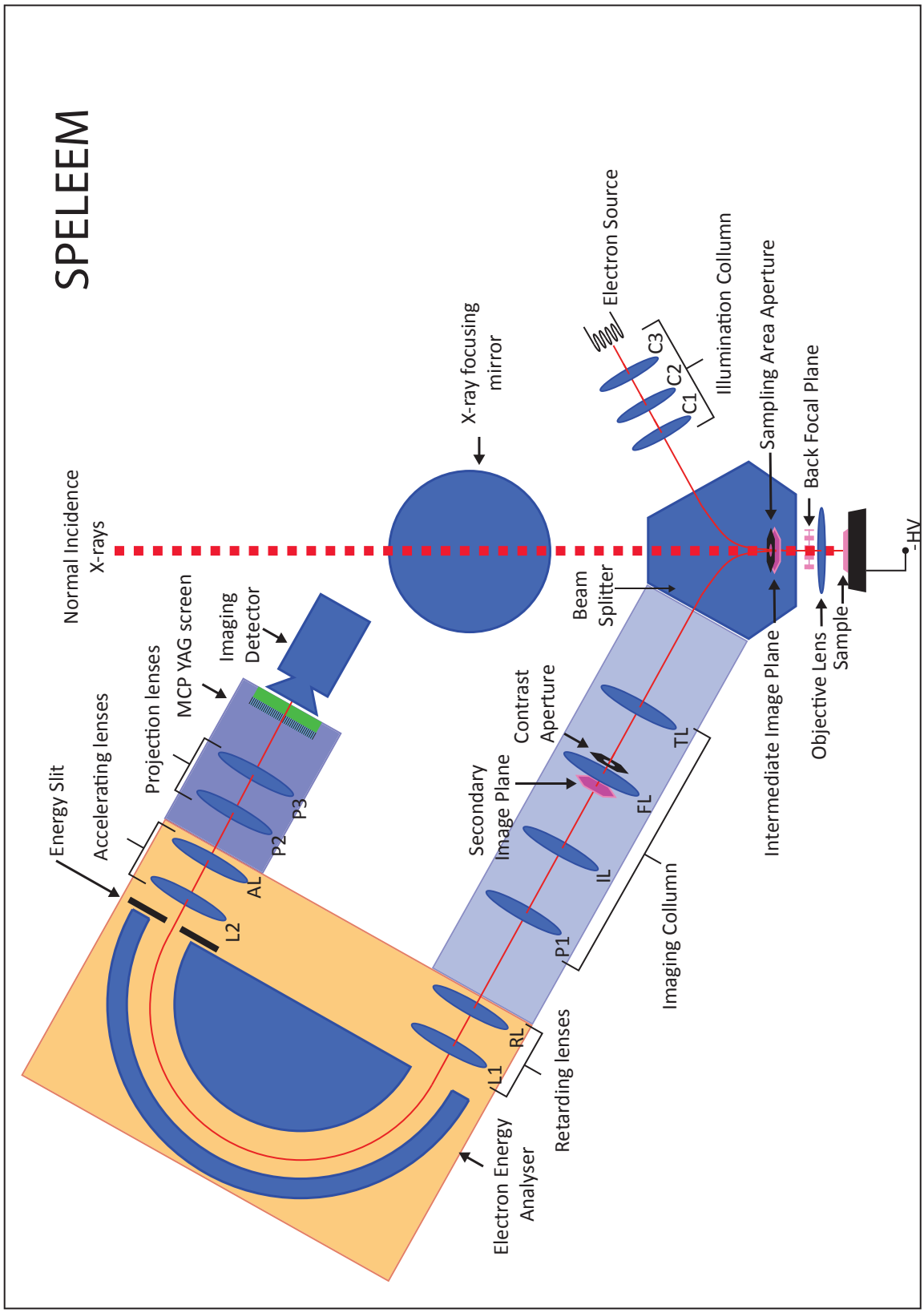

Figure 2.9 Shows the instrument components present in the 'Elmitec SPLEEM II' at beamline I311 MaxLab, the primary microscope used during these investigations. For full details see the text.

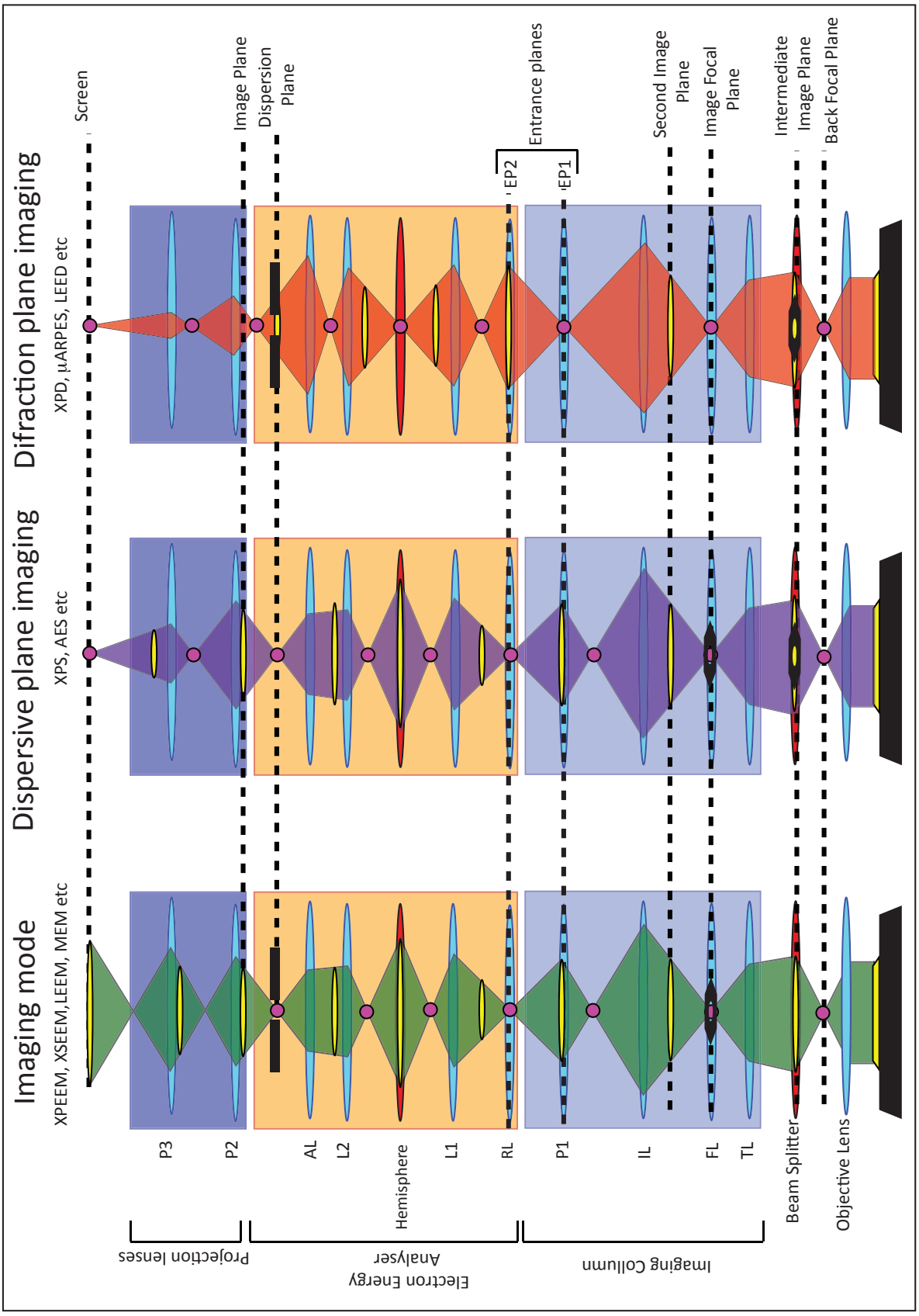

Figure 2.10 A schematic of the optical trajectories used for different imaging modes. For simplicity the hemispherical section of the analyser and beam-splitter are represented as lenses (in red). Images of the sample surface planes are shown as yellow disks, whilst images of the back focal plane are red circles. The direction of the images is not shown; however it is worth noting that for XPEEM mode the image arrives on the screen at different rotations dependent on the field of view (FOV) used. For full details see text. Image adapted from [38].

The imaging modes XPEEM, XSEEM, LEEM and diffraction mode LEED have already been discussed, however as briefly mentioned earlier other complementary modes of operation are also available. Namely, XPD, μARPES, MEM, LEEM-IV, XPS and phase contrast LEEM. The Latter mode 'phase contrast LEEM' utilizes the many phase shifts and interference differences occurring from electrons reflected from the opposing sides of stepped terraces, however no use of this mode was made during these investigations and shall therefore be discussed no further.

Being able to energy filter and image the back focal plane when illuminating the sample with X-rays opens up the ability to image the diffraction information that forms as photoelectrons are excited into the vacuum. Depending on the energy of the incident photons, two regimes exist for analysis XPD and μARPES. Photon energies above the absorption edge of a core level electron gives rise to a diffraction pattern arising due to the coherent interference of directly emitted photoelectrons with those elastically scattered from structural components. As the back focal plane contains interference from all emission angles, a 2D diffraction pattern of the photoelectrons in $K_{\parallel}$ space is observed. The variation in photoelectron intensity as a function of emission angle in turn provides structural information[67]. To the same respect if the appropriate photon energy is chosen, then the angular distribution of photoelectrons excited from the valence band of the sample can be imaged. As there is a field-limiting aperture that can be inserted, the angular distribution of valence electrons can be taken from a single island or surface feature down to ≈ 10μm, and usually given the term μARPES. Placing the adjustable slit at the dispersive plane of the analyser allows for energy filtering. Due to low intensity of photoelectrons in comparison with electrons (when using an electron gun to illuminate),

acquiring either XPD or μARPES with high intensity contrast takes significantly longer than LEED.

Mirror electron Microscopy (MEM) also provides spatially resolved images of the surface for which the contrast relates to the topography and work function. The image is created as the illumination electrons are reflected from an area near the sample surface, due to making the sample more negative in relation to the electron source (a negative start voltage). As the electrons do not interfere with the sample surface no diffraction takes place meaning that crystallinity is not a prerequisite of the sample for imaging. Although the mechanisms are complex the basic understanding is that variations in surface work function and height result in a small changes in the imaged electrons energy and reflected trajectory respectively [68].

Acquiring photoelectron peak profiles from XPEEM images is possible by varying the kinetic energy of the detected electrons and plotting the image intensity, however as the acquisition of each image takes around a minute, and the number of images necessary to provide good energy resolution is high spectra are not recorded like this. Alternatively the back focal plane is imaged in the dispersive plane of the analyser and projected on to the screen. The ability to use the selective area aperture also enables selected area XPS to be performed on grown islands of ≈ 10μm in size. However as the size of the X-ray beam cannot be collimated in the same way as the electron illumination column, stray light from around the selected area can impinge on the reliability of such small area XPS measurements.

LEEM-IV is the final technique to be discussed as it provides a remarkable way of distinguishing the number of graphene sheets present on the substrate surface. Yamaguchi *et al* discuss the mechanism of how very low energy electrons (between 0 -10 eV) show discrete oscillations that relate to the number of graphene layers formed via thermal desorption of Si from hexagonal SiC substrates[69]. The mathematics is presented therein but essentially, the illumination electrons interacting with the discrete energy bands in the graphene sheets conduction band causes resonance at specific energies. This resonance enables the electrons to transmit through the sheet into the substrate causing a dip in the intensity of reflected electrons. Each dip in intensity between this energy range can be directly related to the number of graphene layers formed.

Chapter 3 – Materials

This chapter will present an introduction to the key materials used throughout this investigation. The focus will primarily be on semiconducting diamond ($C_{diamond}$), its structure, electronic properties and how these vary in the presence of adsorbed gas species and transition metal interfaces. Graphene's physical and electronic structure, unique properties and the methods of production will also be reviewed. Silicon Carbide (SiC) as a substrate for the production of graphene has already been given significant attention, however a new method will be detailed in the following chapters, therefore aspects of its growth on this substrate shall also be addressed.

3.1 Diamond

Diamond research has been a focus of materials scientists worldwide for the past sixty-five years. The superior hardness, chemical stability and thermodynamic properties have all been well established; however advances in perfecting the growth of synthetic diamond has seen a renewed interest in the material as a semiconducting substrate for electronic applications[70] and as a coating for biomedical implants[71]. Diamond as a material will be introduced before discussing the crystal faces used for this project, the growth of synthetic diamond, its specific electronic properties in relation to dopants, various atomic gas-species surface terminations, reconstructions and finally how transition metal interfaces react at elevated temperature.

3.1.1 History, electronic and crystallographic structure

Diamond, like graphite, carbon nanotubes and Buckminster-fullerene (C_{60}) is an allotrope of carbon. It is in a metastable phase at atmospheric pressures and room temperature, for which the most favourable structure of carbon is graphite. Diamond's existence at these pressures and temperatures (kinetic stability) is a result of the massive activation energy required to naturally form carbon of this type.

In order to understand diamond's structure it is important to understand the various valence and hybridisation states that can occur via combination of the valence electron wave-functions in carbon where, in diamond, due to the overlap of the wave-functions with neighbouring atomic sites within the lattice, a combination of s and p like character functions arise from the L-shell of the ground-state atom ($2s^2 2p^2$). (organic chemistry notation is commonly used that relates the physical structure to the electronic states and

denotes these wavefunctions 'sp' electrons. However this is a rather limited picture). This means that four independent valence electron states are now available for bonding, which in the case of diamond bond to four neighbouring carbon atoms (sp^3-bonded) creating the tetrahedral symmetry and configuration shown in figure 3.1a. The resulting crystal structure is two interpenetrating FCC lattices (a_0= 3.57 Å) with a C-C spacing of 1.54Å.

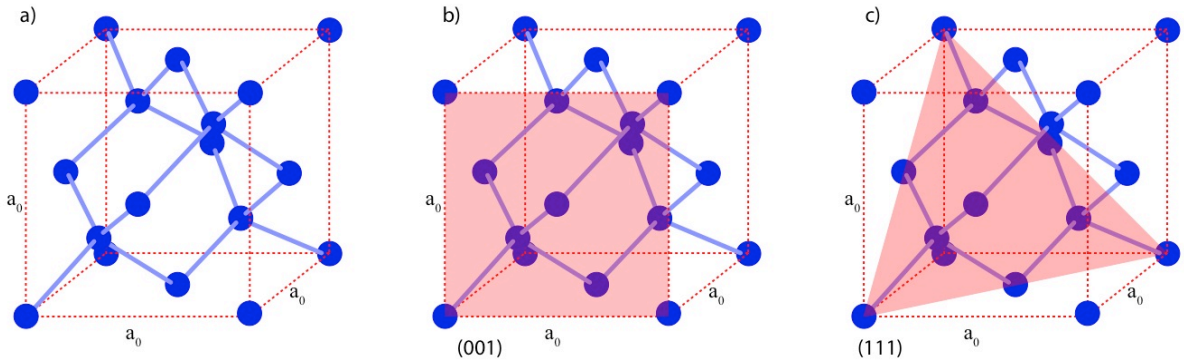

Figure 3.1 a) The diamond structure, the 001 and 111 crystallographic orientations are shown in b) and c) respectively.

This very densely packed structure of carbon atoms is what gives rise to many of diamond's remarkable properties. As a stone diamond boasts one of the highest refractive indices (2.417), giving it the desired lustre and brilliance for fine-gem making. In its bulk form it is one the hardest natural materials, with an extreme mechanical hardness to wear of ~170GPa for the (111) surface[72] . The other extreme properties of diamond are listed in table 3.1 (Taken from[73, 74]).

- highest bulk modulus (1.2 Å~ 1012 N m−2)
- lowest compressibility (8.3 Å~ 10−13 m2 N−1)
- highest room temperature thermal conductivity (2 Å~ 103 Wm−1 K−1)
- thermal expansion coefficient at room temperature very low (1 Å~ 10−6 K)
- broad optical transparency from the deep ultraviolet to the far infrared
- highest sound propagation velocity (17.5 km s−1)
- very good electrical insulator (room temperature resistivity is ca. 1013 Ω cm)
- diamond can be doped, becoming a semiconductor with a wide bad (5.4 eV)
- very resistant to chemical corrosion
- some surfaces exhibit very low or 'negative' electron affinity

Table 3.1 The remaining properties of diamond- – taken from [4,5]

Natural diamond is insulating, as its band-gap is large (E_g=5.5 eV). Defects and impurities that form during its growth are always present; therefore stringent guidelines are in place for the classification of natural stones. Two types were first distinguished by Martin, Robertson and Fox as a small number of diamonds showed lack of absorption in the infra-red and the ultraviolet, in comparison to the majority of diamonds studied. So-called 'transparent' diamonds were classified 'Type II' and the majority 'type I' [75]. It was found that the lack of nitrogen was responsible for the deviation in spectroscopic absorption where natural diamonds of type 1 contain around 0.3% nitrogen and type II virtually none. Further subcategories were added when phosphorescence and conductivity was apparent in a tiny fraction of the stones studied by Custer[76]. Boron substitutions in the lattice were responsible for this observed conductivity. Four categories now exist as shown in table 3.2.

• Type Ia – Nitrogen content of around 0.3%:	Most common
• Type Ib – Very low nitrogen content around few hundred ppm:	Rare
• Type IIa – Undetectable amount of nitrogen:	Very rare
• Type IIb – Naturally boron doped, semiconducting:	Extremely rare

Table 3.2 The current classification categories of natural diamonds

The current industrial needs of the world for diamond-based material require the production of synthetic diamond. A high-pressure high-temperature (HPHT) method emerged for the production of the first synthetic crystals in the 1950's. General electric successfully subjected graphite to extreme pressures in a pressure cell full of transition metal at high temperatures (>2000K)[77]. The diamonds produced were small, but due to the material properties perfect for abrasives for drilling and polishing, with hardness capable of polishing even some diamond surfaces, due to hardness increasing as grain size decreases as described by the Hall–Petch effect[72]. Larger crystals are now being produced, and are either ground down for the same purpose or used as extremely hard cutting bits for machining. The abundance of nitrogen defects in diamonds created this way meant that substrates for electronic applications were not available via this growth method.

Alongside the industrial use of HPHT diamond, researchers were devoted to producing thin films of diamond that met the stringent requirements for semiconducting applications; namely good crystallinity (polycrystalline or monocrystalline), low nitrogen content (for transparency), selective dopant levels (to vary the conductivity) and large

wafers for industrial processing of devices. A vast variety of chemical vapour deposition (CVD) methods emerged for producing diamond thin films. For a thorough review see *Refs*[10, 78]. The process involves some initial gas phase chemistry, in which the reactant gas(gases) is(are) activated into the atomic state, and then incident onto a substrate for epitaxial growth.

Earlier diamond was described as the less favourable form of carbon at low pressures at which sp^2 carbon dominates. The presence of atomic hydrogen has been found to play an important role formation of sp^3 bonded carbon at low pressures due to the creation of stable methane radicals in the gas phase that don't effect the growth, and radical H^+ ions that can saturate the carbon dangling bonds at the growing diamond surface stopping them from reconstructing into graphite like domains. The growth mechanism relies on the different bond strengths between the gas species, where H-H > C-H > C-C. Therefore removal of the hydrogen atom from the terminated dangling bond can only occur by its combination with another H^+ radical, which in turn makes this site available to a carbon containing species (predominately CH_3 [79]) and hence growth of the diamond domain. As the etch rate of graphite with atomic hydrogen is much higher at these temperatures and pressures than for diamond, the production of pure diamond films is possible. Two main types of diamond reactor are used for growth in this way, thermal and plasma; the first uses a hot filament to crack the gaseous species into its constituent radicals, and in the second a plasma of the gas species is activated above the sample held at high temperatures (around 1000-1400 K). In the case of the samples used throughout this investigation the gas was excited by microwaves, which is now the most common technique for producing CVD diamonds, microwave plasma CVD (MPCVD), however for a

full review of the various growth techniques and apparatus see[78]. The added advantage of doping the material during growth with boron means that it is possible to produce p-type semiconducting and even superconducting diamond wafers [80-82].

The growth dominates on the two crystallographic planes (001) and (111)[83] however (001) is the preferential growth direction[78] as stacking faults along the (111) direction are more probable. The best substrate for (111) growth is a high quality HPHT diamond with the corresponding face[84, 85] whilst (001) crystals can be grown on a variety of substrates such as single crystal metals that are capable of withstanding the high temperatures produced during growth e.g. molybdenum[73] and tungsten carbide[10], single crystal silicon[73, 78] and HPHT diamonds[85]. Large (10 x 10mm) single crystals are now commercially available from companies such as Element six (UK)[86].

3.1.2 Diamond Surfaces

The use of diamond for electronic devices requires an in-depth understanding of the various band gap states that can be induced and utilised for device manufacture. As with most semiconductors these states can be created by passivation of the surface dangling bonds with various gas atom terminations or reconstructions. The resultant gap states are usually referred to as 'surface states 'as the wavefunctions responsible are localised to the surface only. The crystallographic planes used throughout this investigation are (001) and (111), the slice through the bulk lattice is illustrated in figure 3.1 b and c respectively (red shaded area) and the bulk Brillouin zone with nomenclature in figure 3.2. It is worth noting that when a study of a particular surface is performed, the centre of the surface Brillouin zone is notated as $\bar{\Gamma}$ as it contains the projection of the bulk state Γ. The Surface

structure present for these crystallographic planes is shown in figures 3.3a and 3.4a respectively, in addition the reciprocal space pattern for each case.

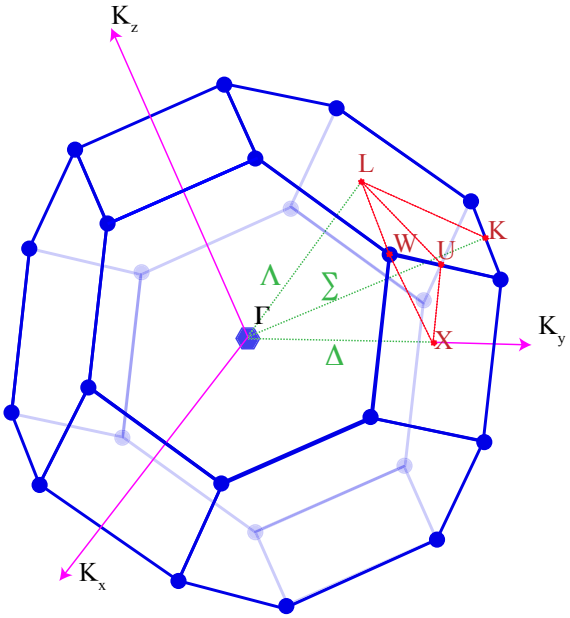

Figure 3.2 The bulk Brillouin zone of carbon in the diamond lattice. L and X lie at the centre of 001 and 111 faces respectively. The corner of the square lattice that intercepts a hexagon is labelled W, where half way along the edge of each surface Brillouin zone are labelled U and K for the 001 and 111 faces respectively.

The atomic spacing of the surface atoms is $\frac{a}{\sqrt{2}} = 2.523\text{Å}$ for both surfaces. Surface dangling bonds in these illustrations are saturated with adatoms, leading to a (1x1) reciprocal lattice pattern in LEED. In reality a number of gas-species can be adsorbed onto the diamond surface and more complex arrangements of bonds and structures will be discussed later.

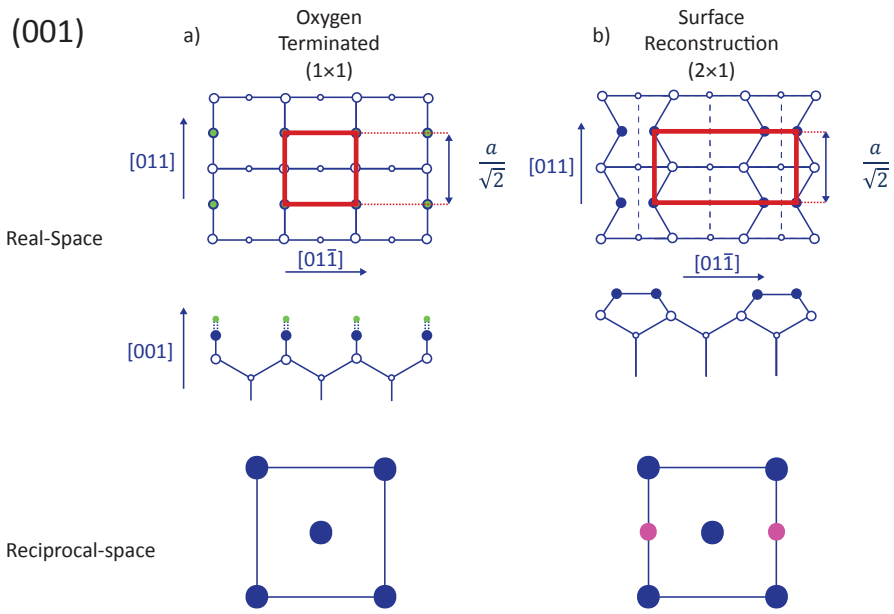

Figure 3.3 Shown here is the real space and reciprocal space lattices of the (001) plane of diamond for a) hydrogen terminated surface (1x1) and b) the reconstructed surface following high temperature removal of surface adatoms. The atoms subtended by red represent the unit cell. The surface reconstruction positions in reciprocal space are in pink.

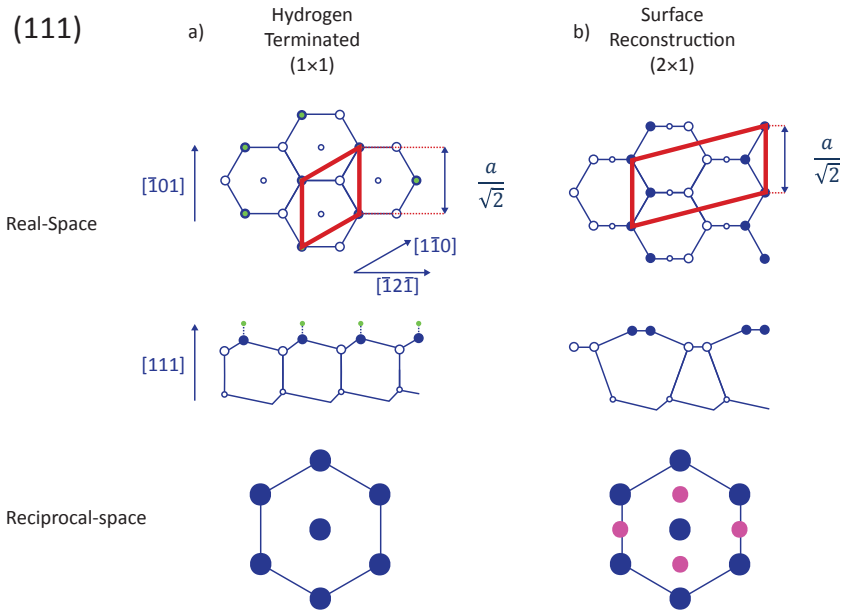

Figure 3.4 Shown here is the real space and reciprocal space lattices of the (111) plane of diamond for a) hydrogen terminated surface (1x1) and b) the reconstructed surface following high temperature removal of surface adatoms. The atoms that are subtended by red represent the unit cell. The surface reconstructed atoms in reciprocal space are in pink.

Before discussing these surface terminations, the nature of the two diamond surfaces at high temperature will first be discussed. The activation barrier mentioned for forming diamond provides high thermal stability for diamond's bulk lattice where a temperature

in excess of 3000K is necessary for the transformation of sp^3 diamond into sp^2 graphite. However it is possible to remove the surface adatoms that terminate the dangling bonds at the surface via high temperature annealing in an ultra-high vacuum environment. The now 'free' dangling bonds mean that the surface is in an energetically unfavourable state, and the atoms must relocate until the surfaces reaches its lowest energy configuration. Although these reconstructions minimise the free energy of the system, some surfaces are inherently unstable and the presence of very few adatoms sufficient to remove it. It is for this reason that a reconstructed surface can be said to be completely free of contamination species or 'clean', which is important when studying interfaces between substrate and grown thin films.

The surface reconstructions of diamond's [001] and [111] face are illustrated in figure 3.3 b, and figure 3.4b respectively. For the case of the (001) surface, two dangling bonds exist for each surface carbon atom. In this case they are saturated with oxygen, giving the (1X1) reciprocal pattern shown, however other terminations are possible (see 3.1.3). Upon removal of these atoms the surface undergoes a reconstruction to a (2×1) structure, in which rows of stable unbuckled symmetric dimers are formed along the (011) axis on the surface with a spacing of d(C-C) 1.37Â, a distance of $\frac{a}{\sqrt{2}} = 2.523$ Å is still observed in one direction. The resultant electronic configuration results in an indirect surface band gap of 1.3 eV(although theoretical calculations put it at ~1 eV) [87] at $\overline{Y}$, half way along the short edge of the reconstructed surface Brillouin zone when a cut is taken from the Brillouin zone centre $\overline{\Gamma}$ along the [110] direction[88] (real space direction along the surface dimers). As the surface has a twofold symmetry ($\theta_{\text{mirror plane}}$=90°) the reconstruction is equally likely to occur along the $[01\overline{1}]$ direction, meaning two rotational

domains of the reconstruction are usually observed (figure 3.5) [88] as opposed to the ideal case shown in figure 3.2b.

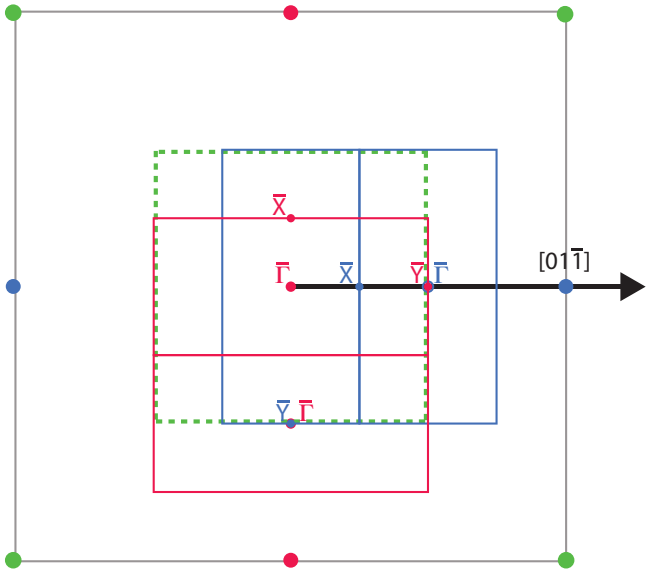

Figure 3.5 A schematic of the reciprocal position of the (1x1) bulk structure (green) and the two rotations of the (2x1) surface reconstructions (red and blue) along with their respective Brillouin zones in matching colours

Within the bulk the (111) plane is terminated on one side with 3 bonds (3db) and a single bond on the other (1db) that make up the tetrahedral crystal lattice. The natural cleavage plane has been found to be the 1db surface [89] in the case illustrated in 3.4a each dangling bond is saturate with a single hydrogen providing a (1x1) structure. The hexagonal ring formed from the two surface layers is corrugated, which leads to characteristically different intensity variation of the diffracted low energy electron beam with electron energy (LEED-IV). As there will be a different energy required to reach the Bragg condition (maximum intensity) for each layer of the corrugated ring. Early calculations of the electronic band structure for the (1x1) (111) surface were initially undertaken by Painter, Lubinski and Ellis (1971) [90], for which an ab-initio method was employed, and experimentally investigated via ARPES by Himpsel, van der Veer and

Eastman (1980) [91]. The bulk band structure was found to be fairly primitive with only feature that approaches the E_f at $\bar{\Gamma}$ as a result of direct band-to-band photoemission transitions. A difference of ~1 eV was found for the position of the valence band maximum (VBM) below E_f that contradicts the calculation.

Upon removal of these adatoms via annealing of the sample in vacuum at ~1000 K, the surface will undergo a reconstruction into chains of π-bonded dimers formed from the upper most surface atoms along the $[\bar{1}01]$ direction as initially proposed by Pandey in 1982[92], whilst the second atomic layer also forms chains in the same direction but below. The C-C spacing along these dimers is now d(C-C) = 1.43Å which is remarkably close to that of graphite (C-C = 1.425Å. The result (as with graphite see section 3.2) is out of plane P_z orbitals perpendicular to the surface that result in out of plane π-bands being formed along the rows parallel to them. The distance between chains (4.37Å along the $[\bar{1}21]$ direction figure 3.4b) is large enough to minimise the interaction between them, leading to electron interaction being confined within the chain. Due to the symmetry of the 111 surface ($\theta_{\text{mirror plane}}$ = 120°), Pandey chains are equally likely to form along the $[01\bar{1}]$ and $[\bar{1}01]$ direction and is indeed the case often viewed experimentally [88, 93], with only one reference in literature of the Pandey chain forming solely in one direction[94]. The LEED pattern that emerges from these three rotational domains can be easily misconstrued into thinking a (2 x 2) reconstruction of the surface had occurred and much debate as to the exact configuration was undertaken [93].

The electronic structure that emerges as a result of reconstructing the surface has been vigorously investigated in order to try and fix issues with the model proposed by Pandey,

for which the biggest concern was the lack of a metallic surface state that cuts E_f as a result of the sp^2 nature of the carbon atoms within the reconstruction. The reconstructed surface in reciprocal space, along with the three rotational domains of the surface Brillouin zones with respect to that of the (1x1) surface is shown in figure 3.6 (adapted from[88]) .

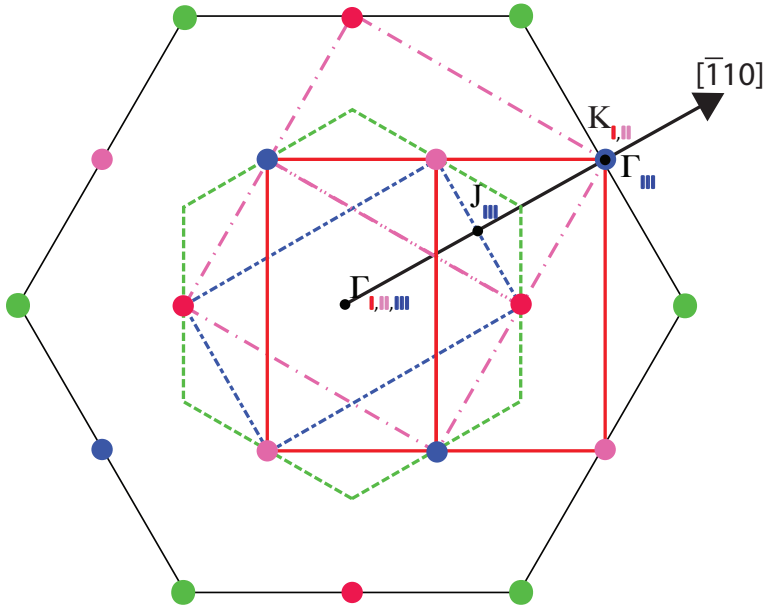

Figure 3.6 A schematic of the (1x1) reciprocal space pattern (green) along with the three rotational domains of the reconstructed (2x1) Pandey chain surface (red_I, $Pink_{II}$, and $blue_{III}$) with their Brillouin zones in matching colours. Adapted from [20].

The surface states created as a result of the reconstruction show strong dispersion along the Γ – J direction and only week dispersion perpendicular to it. A merging of the states at the corner 'K' of two rotations of the surface Brillouin zone (I and II figure 3.6) leads to a surface state that should theoretically cut E_f according to the calculations of Pandey[92], representing a metallic-like surface. The experimental data however is not in agreement with this calculation as a clear gap of 1.0 eV and 0.5 eV is seen in the work of Himpsel and Graupner's, between the valence band maximum and E_f. Pandey and Ristein suggest that differences in the tilt of reconstructed chains will result in an opening of the gap and a

more semiconducting nature for the surface. Furthermore Pandey also suggests that the variation in surface dimer length will have a profound effect on the surface state at $\bar{\Gamma}$ where a gap is increased (decreased) for decreasing (increasing) bond-length[92]. The metallic surface states predicted lead to the postulation of graphitisation at the surface-vacuum interface, as graphite/graphene show similar features. Graphitisation of the surface, i.e. "The solid state transformation of the surface (or areas of the surface) from sp^3 to sp^2 carbon" has also been discussed; Phillips states that the temperature required for reconstruction of the (111) surface is higher than that necessary to graphitise the same surface[95]. Contrary to this Lander and Morrison [96] state that no graphitisation of the surface is apparent even at temperatures above 1500 °C, where for the same surface reconstruction was apparent after 5 minutes at 900 °C in UHV environment. Theoretical modelling (via the tight binding molecular dynamics TB- MD method) of the graphitisation has been implemented by Jungnickel et al [11, 97] in which the presence of (111) twins interpenetrating the surface was key to the de-lamination of the surface (diamond) carbon atoms into free-standing graphitic surface.

3.1.3 Surface terminations

The nature of the clean and reconstructed diamond surfaces are primarily well understood with the exception of possible metallic surface states/graphitisation of the (111) plane. Surface terminations with gas species have also been shown to have an interesting effect on the electronic structure of diamond surface, where different adsorbents primarily affect the electron affinity at the surface. Hydrogen is probably the most important surface adsorbent for diamond as it is one of the precursor gases for

diamond growth and diamonds that emerge from the reactor are always H-terminated. Post-growth termination of the surface is possible via several methods; mechanical polishing in olive oil leads to a highly stable H-terminated surface with E_f pinned for this surface [94, 98, 99]. Acid etch procedures often involve an oxidising reaction rendering the surface O-terminated. In-situ plasma treatment of the surface has also been used extensively for in-situ termination of diamond surfaces, however Shirafuji suggests that the majority of in-situ plasma treatments do not fully terminate the surface [100].

It has been shown that a monolayer of atomic hydrogen provides a mechanism for complete removal of the (2x1) surface reconstruction (de-reconstruction) for (111) surfaces but not for the (001) surface [87, 94, 101]. In order to de-reconstruct the (001) surface both of the surface dangling bonds are required to be terminated. Atomic hydrogen could provide such a termination however the structure formed is closely packed and a strong steric repulsion of the hydrogen atoms prevent the dihydride (1x1) surface from forming [89]. Although theoretically postulated by Kawarada[99] no experimental evidence of this surface (100)1x1:H is observed, only the (100)2x1:H surface. Oxygen provides the necessary bonding mechanism to de-reconstruct the surface. Denoted as the (100)1x1:O surface two possible bonding states emerge as ketone (top site) and ether (bridging) models. The former of the two models represents a surface where a single oxygen atom fixed above each surface carbon atom by means of a double bond. The latter predicts a bridging of the oxygen atom between two adjacent carbon sites, although there is little difference in the relaxed energy of these differing surfaces. Experimental LEED-IV measurements performed by Wang show better agreement with the Ether model [102].

As mentioned earlier, an induced change of electron affinity is possible via surface termination with different gasses. The adsorption of hydrogen on diamond is of particular interest due to the induced negative electron affinity [103-106] that is rarely seen for other semiconducting surfaces. The electron affinity of a sample is a measure of the minimum energy required to escape from the conduction band minimum (CBM) into vacuum outside the crystal E_{vac}, often denoted as E_{EA} or χ where

$$\chi = E_{Vac} - E_{CBM} \qquad (Eqn - 3.1.1)$$

As equation 3.1.1 suggests, in most semiconductor surfaces the conduction band minimum lies above the vacuum level. However via termination of the diamond surface with atomic hydrogen, a surface dipole (as a result of the two different electron affinities of C and H) is created that results in a net movement of charge towards C that forces the vacuum level within the band-gap (due to band bending) hence any electron that is excited into the conduction band is free to leave the surface without the need for additional energy. Experimentally hydrogen adsorption on the surface (cannot ionise H for XPS) can be examined by investigation of the sample work-function (cut-off) via PES[93, 105], the addition of components within the C1s photoelectron peak[106] and the increase of electron total yield (secondary electron emission) from the sample for the reasons described above. A shift of the vacuum level in relation to E_F by 1.65 eV by the induced surface dipole results in a value of χ = -1.27 eV for the electron affinity of the (111)1x1:H surface[107]. At higher pressures Hydrogen has also been seen to smooth diamond surfaces at elevated substrate temperatures (650-850°C) [108].

3.1.4 Diamond –metal interfaces

The role of metal–diamond interfaces is an important aspect of not only this project, but also play a role in polishing of diamond surfaces[98, 109], high temperature machining with diamond bits[12], and the formation of electrical contacts for diamond devices [15, 16]. Three types of metal–diamond interfaces exist and can be categorised as follows; inert metal interfaces such as Au, Pt and Ag that form diode-characteristics that depend on the materials work-function and surface electron affinity, where high work-function materials on H-terminated diamonds surfaces provides an ohmic contact for devices[110]. Carbide forming metals such as Al, Ti, Mo, Ta and V which are initially Schottky-barrier forming but upon annealing are accompanied by a phase transition to more ohmic diode characteristics[15, 16, 110, 111]. The third are Graphitising transition-metal interfaces such as Fe, Ni and Co which upon annealing reduce the activation energy required to break sp^3 diamond bonds and form more favourable forms [12, 14, 15, 112]. The latter category is of particular interest in the scope of this project as these metals may provide a method for producing thin films of graphene / graphite, so the relevant literature will be reviewed.

Transition metals, key for the natural formation of diamond (Co, Ni, Fe) have been shown to reduce the temperature required to break the sp^3-bonded carbon allowing the atoms to rearrange into more favourable sp^2-bonded forms. Earlier 'graphitisation' was used as a term to describe the solid-state transformation of the diamond surface into graphite, as this process is also a solid-state reaction (although now involving ferrous metal) it is still an apt term for use and will be referred to as 'catalytic graphitisation' henceforth. Reports of transition metal inclusions graphitising their surrounding diamond surfaces within

synthetic diamonds account for the first known cases, however diamond coated steel drill bits becoming blunt as a result of the high temperatures (achied through friction) of machining, brought new interest to the field. Fyfe and Evans completed a thorough study of the activation energies of Ni, Co and Fe on diamond (111) surfaces and found that the activation energies 175±20, 144±16 and 139±18 $kJmol^{-1}$ and graphitisation onset temperatures of 809±14, 818±8 and 790±5 K respectively. The temperature required for graphitisation in the presence of transition metals is therefore significantly reduced than of the bare surface around 1000 K. A strong relationship between crystal surface and epitaxy of the overlayer was linked to the strength of each catalyst to undergo this reaction [17].

Epitaxial Nickel has been shown to grown with good epitaxy on all three low index surfaces of diamond [113] when the substrate was held at 600-800 °C. Subsequent annealing of these metal/diamond interfaces resulted in graphitic growth at the surface, indicated by carbon Auger spectroscopy, however epitaxy of the graphitic layers was only found on the (001) surface. The lattice constants of (111) Fe and Co are also comparable in length to that of diamond[114] and epitaxial growth on the 111 surface is expected for all interfaces although few results are present in the literature. Ordered graphitic layers were also catalytically grown with Fe on (100) CVD diamond surfaces, and investigated by means of angle resolved near edge X-ray absorption fine structure (NEXAFS) measurements. It was shown that the out of plane π orbitals of the grown layer lay parallel to the surface, hence confirming the graphitic nature of the grown material [115].

3.2 Graphene

Graphene represents a new class of material, it is in fact only a surface and hence classified as a 2D-crystal. It is the latest allotrope of carbon to be discovered and first of its classification, others include the 0D fullerenes, 1D carbon nanotubes and of course the well-known 3D forms of carbon diamond and graphite. Graphene exists as an sp^2 hybridised closely packed honeycomb configuration of carbon. For many materials, approaching a monolayer generally has a detrimental effect on its properties, for the case of graphite however the production an atomically thin layer has unique effect on its electronic properties that make it distinct from other electronic, spintronic and optical materials. It is for this reason that it has attracted so much theoretical, experimental and industrial attention over almost the past ten years. Here a background of graphene's early discovery shall be presented alongside its structural and electronic configuration, before discussing the aspects of its production that this thesis aims to address.

3.2.1 History, electronic and crystallographic structure

Graphene has been theoretically studied for over sixty years as it provided a mechanism for describing many of the electronic properties of graphitic materials[116, 117], however it was thought physically improbable to exist as large crystallites (greater than a few nm) as low dimensional materials are usually thermodynamically unstable and prefer more curved structures under ambient conditions[118, 119]. In 2004 Andre Geim and Konstantin Novoselov produced and investigated graphene exfoliated from a highly orientated pyrolytic graphite (HOPG) crystal [2] for which they were jointly awarded the Nobel prize in physics in 2010. The work found that the material was indeed stable under

ambient conditions, contrary to the previous theoretical predictions. It also displayed unprecedented conductivity for such a material with an estimated 10^{13} cm^{-2} electrons available for conduction with carrier mobilities ~10,000 cm^2V^{-1}. The value of, the carrier mobility in this case was measured by creating a graphene transistor device, and performing field effect and magnetoresistance measurements. Advances in recent years towards better detection methods [120], production of large scale material, chemical-state doping of its bandgap for n and p-type characteristics [121, 122], its fundamental electrical[123-126], optical [127], thermal [5] and spintronic [128, 129] properties as well as its mechanical properties [130, 131] have led to a 'gold rush' of publications, of which there is insufficient space to represent the significant effort that's been undertaken by materials scientists worldwide into realising this material's abilities. Applications that have already been demonstrated for the materials include; transparent conductive layers in photovoltaics and displays [4, 132], gas sensing[6, 133] electrochemistry[134, 135], whilst the future holds promise for quantum computing[1, 136]. The reviews and articles listed above and the references therein represent a decent cross section of the work already conducted. The scope of this work does allow for a larger review on the growth of graphene however, which will follow in section 3.2.2. As with diamond, graphene's crystallographic structure and how it relates to its electronic structure shall first be presented.

Graphene as its name suggests is a graphitic material in which the hybridisation allows for the valence electrons ($2s^22p^2$) wave vectors to overlap into four independent electrons for binding. However unlike the bonding described for diamond previously, the lattice of graphene consists of three in-plane (p_x, p_y) σ-bonds to neighbouring carbon atoms, and

one out of plane π-bond (p_z) which due to the in-plane structure forms out of plane π-orbitals parallel to it (π and π*) which saturates all of the bonding requirements and consequently making the material very chemically stable. The resultant lattice is configured so that neighbouring carbon atoms are in inequivalent sites creating two interpenetrating triangular lattices (pink and blue points Figure 3.7a). The unit cell vector a has a length =2.46Å where the interatomic spacing δ =1.42Å[137].

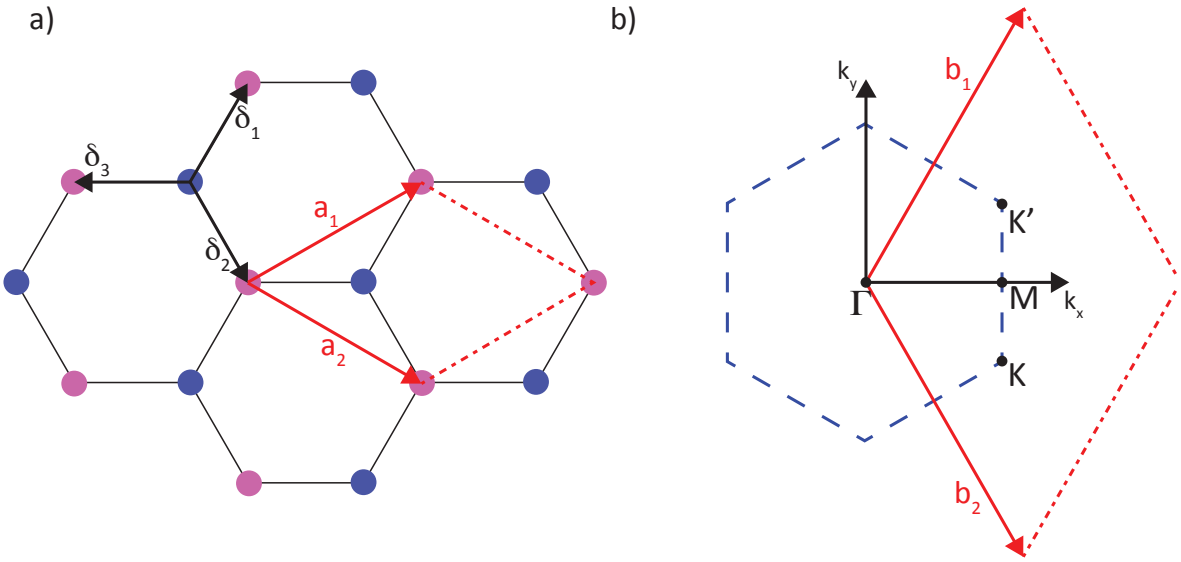

Figure 3.7 a) The real-space honeycomb structure of graphene. The inequivalent lattice points are represented by blue and pink circles, the unit cell vectors a_1 and a_2 of the two interpenetrating triangular lattices are in red (where $a_1 = a_2 = a$). The nearest neighbor vectors δ_1,δ_2 and δ_3 are also shown ($\delta_1=\delta_2=\delta_3=\delta=a/\sqrt{3}$) b) The hexagonal Brillouin zone of graphene with the high symmetry points and the reciprocal unit vectors b_1 and b_2 (where $b_1 = b_2 = b$) in red.

The theory that graphene could only exist as a 2D material whilst on a substrate, due to substrate-graphene interactions such as van der Waals forces, was finally disproved when free standing samples were exfoliated from HOPG and investigated via TEM. Here intrinsic surface roughening in which ripples in the surface of up to 1 nm height were observed and are attributed to helping the thermodynamic stability of samples up to few a μm in size[138].

The electronic structure that arises due to this atomic configuration is a special case in semiconductor physics. Here the conduction and valence band intersect at the Fermi level around each of the K-points (K and K') of the Brillouin zone (figure 3.7b, 3.8) leading to the high conductivity of the material and for this reason often referred to as a semimetal or a 0 eV band-gap semiconductor. What is unusual about the π-bands near the K-points in graphene is that their position in k-space displays a linear relationship with binding energy (figure 3.8), as opposed to the parabolic relationship usually observed in other semiconductors. The energy-momentum relationship for linear bands is described by,

$$E = \hbar V_f k \qquad \textit{(Eqn – 3.2.1)}$$

and the effective mass for the linear dispersion is given by $m^* \cong \frac{E}{V_g V_p} \cong \frac{\hbar k}{V_f}$ where V_g, V_p and V_f are the group, phase and Fermi velocities respectively (see references [139, 140] for details). Whereas the classical parabolic dispersion relation is given by

$$E = \frac{\hbar^2 k^2}{2m^*} \qquad \textit{(Eqn – 3.2.2)}$$

and the electron mass $m^* = \frac{1}{\partial^2 E/\partial k^2}$ [141] see figure 3.9.

Equation 3.2.1 and the definition of the effective mass means that as $E \to 0$ and $k \to 0$ so does the effective mass. If this is true then the charge carriers in graphene exhibit no effective mass at the K-point and therefore are best described by a 2D case of the quantum theory introduced by Dirac, in which massless-fermions are the charge carriers. It is for this reason that the charge carriers in graphene are often called 'massless Dirac fermions' and the point of valence-conduction band intersection around K (K') points called 'Dirac points'. For a full derivation of the theory used to calculate the band

structure of graphene see the early work of Wallace [117] and more recently Castro *et al*[142].

One of the main distinguishing characteristics of these quasiparticles is the dependence on the cyclotron mass with the square root of the electron density (Schrödinger-like dispersion describing a constant cyclotron mass), which has indeed been observed experimentally [143]. Recent investigations [144, 145] show discrepancies in the linearity of the bands at the K-point from this basic outline presented here. It was shown that due to electron-electron (e-e) interaction at the neutrality point V_f increased to as much as $3x10^6$ ms^{-1}, much larger than that usually reported in literature of V_f = c/300[146]. However the techniques necessary to distinguish this (via analysis of Shubnikov-de Haas oscillations SdHO) are not used throughout this investigation and therefore the bands will still appear linear within experimental limits. Nevertheless this difference from classical electrons promises yet more exotic properties such as the trademark integer quantum hall effect (IQHE) at room temperature, observed experimentally in 2007 [147], Klien paradox (tunnelling of charge carriers with a probability of 1), Zitterbewegung (jittery motion of the Dirac wavefunctions) are also observed[142], offering the possibility for fundamental investigations into this type quasiparticle truly a first for condensed matter physicists.

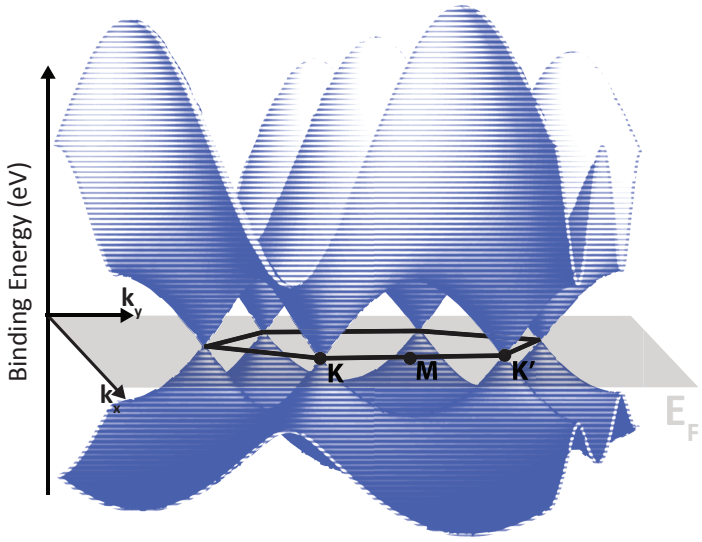

Figure 3.8 Tight-binding approximation of 1.5 x graphene's Brillouin zone, band structure calculated using Wolfram demonstration software available online (see ref [148] for details).

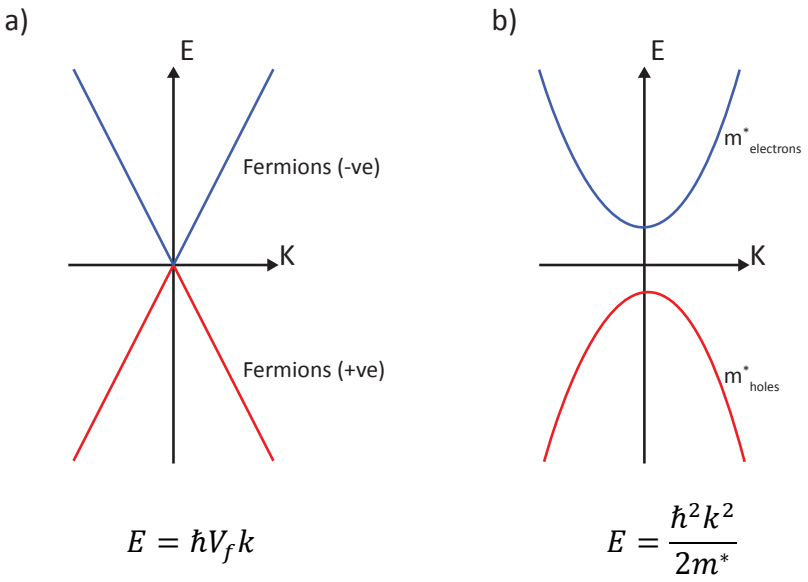

Figure 3.9 Dispersion relations around E_f for a) the linear bands observed around a Dirac-point of graphene, and b) that around the direct bandgap of a standard semiconductor

The electronic properties of a graphene bi-layer are expected to be different for graphene due to out of plane hopping of the electrons between sheets, beli ed to behave as massive chiral quasiparticles[149, 150] that show different IQHE properties to the

monolayer. However this variance in electronic structure is not detrimental for device manufacture as it offers the possibility of opening a tunable band gap in the material via the application of an external bias between layers [151] . This makes a graphene bi-layer the only semiconductor in which the band gap can be tuned by an external bias.

Edge effects, also referred to as 'surface states' occur due to the different configuration of atoms available at the edge of a graphene sheet, named zig-zag or armchair (figure 3.10) and have an effect on the electronic structure of graphene nano-ribbons (GNR) [152], where a band gap can be tuned between 0.2 and 1.4 ev by varying the width and edge configuration of the GNR.

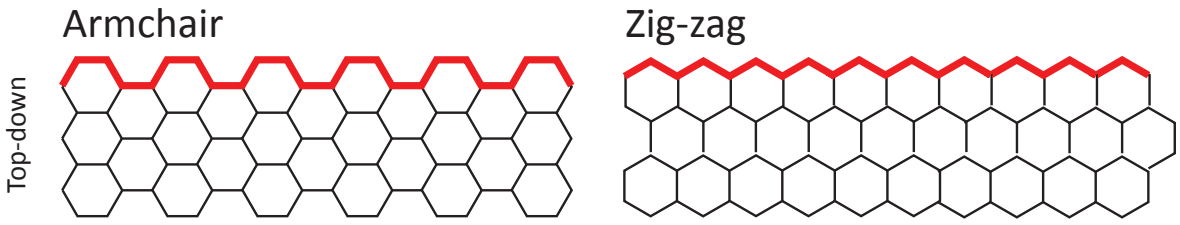

Figure 3.10 Edge terminations of graphene nano-ribbons.

Defects play a crucial role in the properties of graphene [152, 153] dislocations that lead to the formation of pentagon, heptagon or octagon (known as haeckelites) inclusions in the graphene lattice can lead to massive out of plane warping of the sheet[152]. Stone-Wales (SW) defects (pentagon-heptagon pair) caused by a 90° rotation of two carbon atoms with respect to the midpoint, are thought to be one of the defects that causes graphene to buckle or roll up into nanotubes [154]. Theory shows that defects in the lattice generally cause a splitting of the band-gap that increases proportional to the

number of defects present[155]. Pairs of SW defects (5-7-7-5) can lead to grain boundaries between zig-zag and arm-chair terminated sections in graphene sheets [156].

3.2.2 Graphene growth

Since its initial production via the micromechanical exfoliation of HOPG in 2004, graphene growth has been explored via solid-state[137, 157-159], CVD[160], chemical exfoliation[161], gas phase [162] and wet-chemistry [163] processes, as well as many more. The abundance of methods already capable of producing low-cost large area graphene begs the question as to why more research is being devoted to such a task, and the answer lies in the quality of the material produced. Processes such as the micromechanical cleavage of graphite still yield the highest quality crystals of graphene, and for this reason have been primarily used for fundamental studies of graphene's electronic properties [1, 2, 138, 143, 145, 147]. However the small size of crystals available means that large area production in this manner is unachievable; never the less cleaved graphene is the measure of quality for all other production methods. In most cases the quality of the graphene necessary for production is linked to the end application, where applications such as transparent conductive coating can be made from wet-chemical methods, which due to production environment is usually accompanied by large number of defects including sp^3 inclusions [32, 164] and a large number of grain boundaries due to the small crystal domains. This type of graphene is however still conductive enough to compete with current materials such as indium tin oxide (ITO) glass[165]. The number of active sites on graphene oxide prepared in this way makes the functionalization of the material with other nanoparticles or polymers possible which opens another exciting avenue to pursue for this type of material [134]. Applications that

utilise some of graphene's more exotic electronic properties, such as its spin-transport potential[128], require the production of extremely high quality graphene. Two methods of production have shown promise in growing material with such quality; the high temperature sublimation of silicon from silicon carbide (SiC), and the chemical vapour deposition of carbonaceous gasses such as methane on to both single crystal and polycrystalline metal substrates. A review of both methods will be presented here.

3.2.2.1 Sublimation of Si from SiC at high temperatures

Silicon carbide (SiC) is a wide band-gap semiconductor composed of silicon and carbon in an equal stoichiometric ratio. The crystal structure is the same as diamond however each element is bonded to four of the opposite element in a tetrahedral configuration. The stacking of these two tetrahedrons (C-Si_4 and Si-C_4) within the lattice allows for rotation between the crystal planes. The structure can therefore take on a zinc-blend, wurtzite or rhombohedral lattice (of which there are numerous possibilities). This phenomenon is known as polytypism and defined as 'the phenomenon of taking different crystal structures in one-dimensional variation with the same chemical composition [166]. At least 11 were known of before the 1960's [167] and over 200 are now known [166]. The poly-types are expressed using Ramsdell's notation as the number of Si-C layers in the unit cell together with a symbol that denotes the crystal structure, C, H and R for cubic, hexagonal and rombohedral respectively. The three most technologically important polymorphs of SiC are 3C-SiC, 4H-SiC and 6H-SiC [168]. Hexagonal crystallographic notation is used to describe the surfaces where the four Miller-Bravais indices are the in-plane vectors a_1,a_2 and a_3 where $a_1+a_2+a_3=0$ and the out of plane vector 'c' to the next

layer (perpendicular to a_i where i =1,2 or 3) , given as ($a_1a_2a_3c$) where (0001) and ($000\bar{1}$) are the Silicon and Carbon terminated surfaces respectively.

Single crystal SiC was therefore difficult to grow as a mixture of many polytypes often occurred, an control over the growth of a single polytype was vital for producing highly monocrystalline substrates of SiC for electronic applications[168]. Step-controlled epitaxy emerged as way to produce the desired polymorph by CVD process onto an off axis substrate of the same orientation. The steps formed in the bilayers due to the off axis cut provide the necessary template for epitaxial growth. Due to this process the growth of high quality single crystal wafers of a single polytype is now possible at industrial scale (see the review of Matsunami [166] and references therein for more details).

The graphitisation of SiC surfaces for the production of graphene has seen a renewed interest in the field, as it was already well known that the surfaces of SiC undergo graphitisation at temperatures elevated above 1250 °C [169-172]. This is due to the solid-state decomposition and sublimation of Si from the surface at high temperature. The abundance of carbon atoms left behind on this surface then re-crystallises to form graphitic surfaces.

The production of ultrathin graphite on the (0001) Si-terminated surface of 6H-SiC, as a route towards the production of graphene based nanoelectronics was undertaken by Berger et al in 2004, separate to the now Nobel prize winning efforts of Geim and Novoselov [173].

Both polar faces of the 6H and 4H SiC have been investigated for the production of high quality graphene, however graphitisation of the C-terminated ($000\bar{1}$) surface results in a

much more complicated evolution of the reconstructions and higher decomposition temperature[174] and results in stacking faults and many rotational domains of the graphene[175]. For this reason this review mainly focuses on the Si-terminated (0001) face of hexagonal SiC.

The first layer of graphene grown on the surface of 6H-SiC (0001) is identifiable via a$\left(6\sqrt{3}\times6\sqrt{3}\right)R30°$ reconstruction observed in LEED and STM [157, 172]. This carbon rich surface forms the template for subsequent graphene layers to grow and is often referred to as 'layer 0' or 'the buffer layer' [137, 158]. The buffer layer is still strongly interacting with the SiC substrate as 33 ± 4% of the carbon atoms making up the reconstruction are covalently boned to the bulk SiC structure. This layer does not display any of the electronic characteristics of graphene[176]. ARPES band mapping of both surfaces revealed that the σ-band of the buffer layer was at 3.2 eV higher binding energy than that of free standing graphene indicative of covalently coupled p_z orbitals[175]. Further annealing of this surface at 1250 °C leads to the formation of subsequent layers that give rise to the linear dispersion characteristics of graphene, the buffer layer persisting at the interface between the SiC(0001) surface and the graphene stack. Some interaction between graphene and substrate is apparent as the K-point of first graphene layer is still situated 0.4 eV below E_f indicating n-type doping due to charge transfer to the substrate[177]. Hydrogen has been shown to intercalate under graphene monolayer on SiC to produce a 'quasi-free standing' in which the electronic structure closely resembles that of exfoliated graphene [178, 179]. Annealing the sample at around 700 °C in an atomic Hydrogen atmosphere (10^{-6} mbar) enables hydrogen to intercalate (most likely through defects or grain boundaries) under the graphene buffer-layer and terminate the

underlying Si surface creating bi-layer quasi-free standing graphene. In the same way the buffer-layer alone can be promoted to monolayer quasi-free standing graphene [178]. Irregular shaped single crystal grains of graphene prepared in this way were found up to 20μm in size [137], however they coexisted with graphene bi-layers and uncovered regions of the $\left(6\sqrt{3}\times6\sqrt{3}\right)R30°$ reconstruction [69, 175]. Larger area crystals have been obtained via annealing a Si-terminated SiC substrate in an Argon atmosphere at atmospheric pressure (1bar) [180], where it was shown that the size of the graphene grown was limited to the length and width of the terraces on the SiC surface.

Graphene prepared in this way has the benefit of growing directly onto a wide-bandgap (semi-insulating) substrate and therefore its electronic properties should not be inhibited by interactions with the substrate. Experimentally the integer quantum hall effect has been observed in graphene prepared in this manner[181] showing that this material is of a comparable structural quality to that prepared via mechanical exfoliation. The main drawback of quasi-free standing graphene prepared in this way is the temperature dependence of Hydrogen desorption from under the material (around 750°C) and a return of the quasi-free standing material back to the non graphene-like electronic structure of the $\left(6\sqrt{3}\times6\sqrt{3}\right)R30°$ reconstruction[137, 178].

3.2.2.2 Chemical vapour deposition (CVD) on transition metals substrates

One of the most attractive methods of producing graphene is the inexpensive and readily accessible method of chemical vapour deposition [182]. Much of the early work focusing around structural carbon on metal surfaces, derives from investigating potentially

annoying forms carbon (contaminants) segregating from metal substrates at high temperatures[183, 184] where it was observed that a stable carbon monolayer was present on the surface if held at 100K above the temperature required to dissolve carbon in Ni(111). Further growth of graphite multilayers occurred upon cooling as a result of residual carbon precipitation, a method of graphene production now known as 'controlled carbon precipitation method' [159]. However the formation of structurally stable carbon via the dissociation of hydrocarbon gasses on hot single crystal of a Pt(100) in 1968 [185], provides some of the earliest evidence on the existence of 2D graphene from CVD methods. Graphene formation by decomposition of hydrocarbons on the surface of Pt(111) (described as single layer graphite) was investigated by STM as early as 1991[186].

Production of graphene on transition metals substrates via CVD is now a thriving research field, with graphene growth being demonstrated on polycrystalline and single crystal faces of various metals including Ruthenium[187], Nickel[188], Gold[189] Platinum[190], Copper[191], Rhenium [192], Rhodium[193], Palladium[194], Iridium[195] and Cobalt[196]. The review of J. Wintterlin covers the work up until 2008 [197] and that of M. Batzil up to 2012[198].

Two methods for producing graphene via CVD exist; a top down approach in which de-hydrogenation of the gas species is catalytically favourable on the metal surface allowing carbon to aggregate on the surface to form graphene. This process is self-limiting as a fully covered graphene surface removes the catalysis metal and hinders de-hydrogenation of the gas species[199]. The second method is a bottom up approach in which atomic carbon is forced into the metal substrate at high temperature and the

carbon precipitation controlled during cooling to form monolayer graphene. The driving force of carbon segregation to the surface is the lower energy at the surface than within the hot lattice; a fully terminated graphene surface would lower this surface energy of the metal. The control over monolayer coverage is possible as subsequent graphene growth does not lower the surface energy further, hence subsequent growth ceases as the driving force of precipitation is removed [198].

One of the determining factors in whether the graphene growth is top down or bottom up is the carbon solubility within the substrate. It is well known for single wall carbon nanotube (SWCNT) growth, that transition metal catalysts have a temperature dependent carbon solubility, and that control over the metal particle size (when using metal nanoparticles) and reaction temperature has large implications towards the quality and size of the carbon nanotube produced[200]. To translate to 2D graphene growth, the use of single crystal metals with large grains is used to grow laterally (opposed to the nanoparticles used for vertical nanotube growth), whilst controlling the substrate temperature (hence solubility) is vital. It is for this reason that low temperature methods can be used for top-down growth as little to no carbon dissolves into the substrate hence lateral covering of the surface is favourable[199]. For the carbon segregation method, carbon is accepted interstitially into the substrate lattice at high temperature due to the increased carbon solubility of the metal; once the carbon solubility limit is reached (fully saturated) solid carbon growth on the surface can occur. Alternately if the solubility is lowered (by lowering the substrate temperature) carbon will precipitate back out of the metal lattice and re-crystallise on the surface to form 2D graphene [159]. Modifying the

substrate thickness of increasing the strain has been proposed as a method of reducing the carbon segregation into the bulk[201]

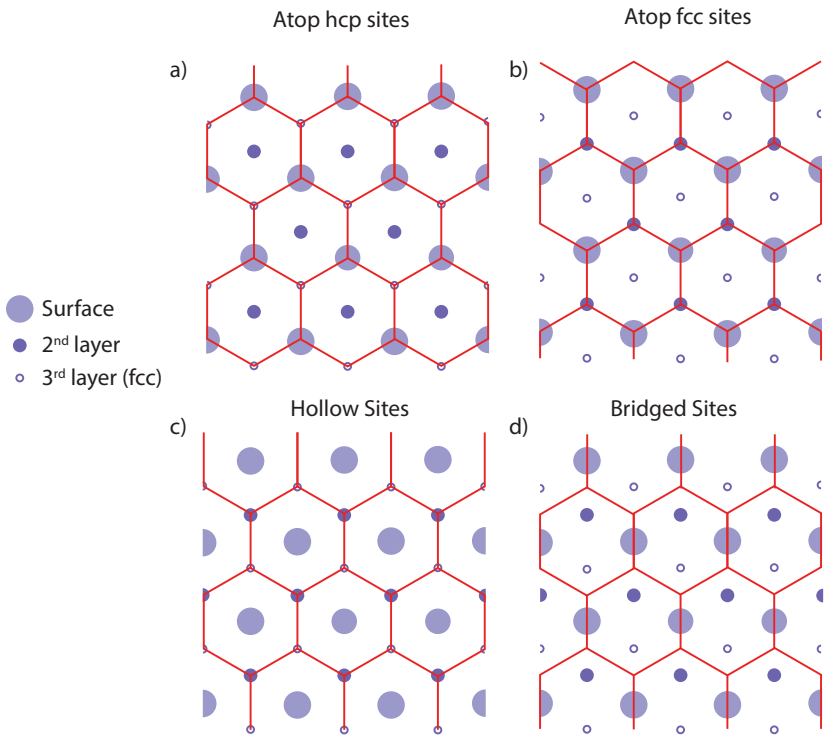

Figure 3.11 A schematic representation of the basic epitaxial positioning of graphene on fcc(111) and hcp(0001) metal surfaces. Graphene is represented by the red hexagonal lattice whereas the metal atoms are drawn as circles (figure adapted from the review of M. Batzil see *Ref.* [198])

The interaction between graphene and its metal substrate has implications on the quality of the material grown and its electronic structure. A lattice mismatched system, where the graphene overlayer and substrate lattice are incommensurate, results in moiré pattern due to the periodic nature of the mismatch [202]. Figure 3.11 shows the basic epitaxial positioning of graphene on metal surfaces; for graphene grown on hcp(0001) and fcc(111) the carbon atoms alternately occupy the atop-metal surface atoms and the respective surface hollow sites, a and b respectively and is the case for Co(0001)[196] Ni(111)[203]. The possibility of graphene growing in which all of its lattice points occupy

hollow spaces on the surface also exists i.e. each hexagon surrounds a surface metal atom as shown in c, this structure is seen for graphene grown on Ru(0001) substrates[187]. The final absorption structure to mention is that of a bridged graphene surface (d in figure 3.11). In this structure a third of the bonds making up the hexagonal lattice are centered 'atop' the metal surface atoms[198].

The metal-carbon bond length to the first graphene layer tends to be shorter than that observed for SiC, with the extremes being Ru at 1.45Å and 4HSiC(0001) at 1.65Å[204]. However whilst this makes a stronger influence on graphene's electronic structure, it aids the growth of its physical structure by constraining the carbon position at the metal lattice sites (or hollows). The large number of graphene nucleation points on the surface (i.e. around crystal grain boundaries) has been suggested as the dominating factor for small, <100µm, area graphene regions (although often quoted as 'large area' in comparison to that of its exfoliated counterpart) [205]. Reducing the number of graphene nucleation points on the surface can result in extremely large or 'ultra-large' areas of graphene growth. Electrochemical polishing of a copper foil followed by a lengthy 7 hour anneal in high pressure hydrogen atmosphere has been shown to significantly reduce the number of nucleation sites, enabling the production of a hexagon shaped single crystal of graphene 2.3mm in diameter. The current largest graphene single crystal to be produced measures 5mm in diameter[206] and was produced via maintaining an oxidised Cu_2O surface during the initial stages of growth. This catalytically inactive surface, as well as a high hydrogen/methane molar ration of the active gas species, reduced the graphene nucleation points to 4 nuclei per cm^2 enabling this massive single crystal to grow.

The influence of the metal substrate on the electronic structure of graphene has been investigated experimentally and from first principle DFT calculations[207]. Table 3.3 compiles information regarding the binding energy of the transition metals d-band, the clean metal work function, graphene metal separation distance and the position of K-point with respect to E_f. The information was compiled from the following articles [198, 204, 207-212]

Metal	Binding energy of d-band center relative to Fermi energy [102] (eV)	Metal Work function (eV)	Graphene–metal separation (Å)	ΔE_f of the K-point (eV)
Co(0001)	−1.17	5.44	2.1	-2.0
Ni(111)	−1.29	5.47	2.1	-2.0
Cu(111)	−2.67	5.22	3.3	-0.17
Ru(0001)	−1.41	5.84	2.1	-2.6
Rh(111)	-1.73	5.91	2.2	-2.3
Ag(111)*	-4.30	4.92	3.3	-0.32
Re(0001)	-0.51	5.88	2.1	No ARPES
Pd(111)	-1.83	5.67	2.5	0.32
Ir(111)	-2.11	5.76	3.4	0.10
Pt(111)	-2.25	6.13	3.3	0.33
Au(111)	-3.56	5.54	3.3	0.19

Table 3.3 Information relating to the interaction of graphene's electronic and physical structure in relation to that of its metal substrate/ intercalated layer.*

Table 3.3 clearly shows that with increasing binding energy of the transition metal d-band centre the distance between graphene and substrate also increases. If the distance is below 3.3Å then the graphene exhibits a p-type characteristic as charge transfer between the metal d-band and the graphene π-band is likely (K-point at higher binding energy). However metals that weakly interact with the above graphene layer such as Cu, Au, Ag and Pt show the possible conversion from p-type to n-type graphene (for which the K-point lies below the Fermi-level) as a direct result of the metal work function, where a

work function greater than 5.4 eV is necessary to make the conversion[209]. Metal halides such as AlB_3, although unstable in ambient conditions have been shown to be protected by the above graphene layer when intercalate under $C_{graphene}$/Ir(111) interface[213]. Following the intercalation the graphene layer showed a pronounced hole doping (p-doping) evident by up to a 0.4 eV rigid shift in the graphene's π band observed by ARPES.

A vital aspect of the current investigation is the interaction and growth of graphene on iron substrates. Little work to date has been undertaken in this direction, despite the Fe-C binary phase diagram being thoroughly studied during the search of new catalysis production methods for carbon nanotubes[214]. The phase diagram shows that there are a large number of stable Fe-C phases, and evidence of polytypes also exists[215]. In fact the review of M. Batzil categorically states that graphene is not easily synthesised on this metal [198]. Some evidence of graphene growth on Fe substrates via CVD is available however[216]. In this work the graphene produced showed no defect peak (D-band) in the Raman spectrum, indicative of high quality material. Unfortunately the work does not detail any evidence of the electronic interaction at the graphene – iron interface as the graphene was removed and placed on an insulating substrate for device characterisation. Further more the work of Preobajenski[217] shows that graphene grown on Fe(110) shows strong corrugations that results from the periodicity of the superstructure formed, and the strong interaction of Fe 3d states and the C 2p π-states of graphene .

Iron has also been shown to intercalate under a pre-formed layer of graphene on Ni(111) [203]. Five monolayers of Fe deposited in vacuum onto a completely covered graphene monolayer on Ni substrate were shown to fully intercalate under the graphene at a

temperature of 600K. Photoelectron spectroscopy confirmed the intercalation was not merely clustering of the Fe thin-film on the graphene surface via analysis of specific photoelectron core-level ratios, and the novel application of an oxygen atmosphere ($\sim 1\times10^{-6}$mbar), which showed that the Fe layer was protected from oxidation by the graphene layer above.

3.3 Chapter summary

This chapter has presented background information relating to the materials in use throughout the subsequent investigations. Diamond's bulk and surface properties were discussed before presenting a literature survey of the growth of synthetic diamond, its electronic structure and its reactions to surface terminations such as hydrogen, oxygen and the (111) and (001) reconstructions. A vital aspect of the following investigations is the reaction of diamond surfaces in the presence of transition metals and was therefore thoroughly reviewed. The numerous methods of graphene growth were mentioned and particular emphasis placed on the two methods that currently yield the highest quality material, sublimation of silicon from silicon carbide and chemical vapour deposition on to transition metal substrates. Despite the already numerous methods of production, research into the production of graphene should be driven towards developing processes that meet the mass production requirements of industry. The need for high quality graphene is still very apparent in the literature and new methods for its production should be sought.

Chapter 4 – Instrumentation

Although much of the instrumentation specific to photoelectron spectroscopy such as the hemispherical electron analyser, or the imaging optics of the SPELEEM system have already been mentioned. Other experimental aspects such as ultra-high vacuum, substrate heating, plasma source and controlled thin film growth and have not as yet and shall therefore be presented herein.

4.1 Ultra-high Vacuum (UHV)

The need for ultra-high vacuum has already been discussed, as a necessity for increasing the mean free path of photo and low energy electrons allowing for their possible measurement far away from their creation. However the most useful feature of UHV is that it provides a clean environment. Such an environment aids sample preparation substantially as it allows for desorption of contaminants (detailed later) and preservation of the clean sample surface. The surface needs to be able to remain contaminant free (or a few % of a monolayer coverage) during the course of an experiment. The flux of molecules to a surface determines the rate (if all molecules stick) at which the sample surface would be completely covered, from kinetic theory of gases the rate at which gas molecules arrive at the surface can be given by:

$$\Phi = \frac{1}{4} n c_a$$

(Eqn – 4.1.1)

Where n is the number density and c_a is the average velocity. The root mean squared velocity can be related to the kinetic energy of the particles mass with respect to their thermodynamic temperature by,

$$c_{rms}{}^2 = \frac{3k_B T}{m}$$

(Eqn – 4.1.2)

Where K_B is the Boltzmann constant, m the particle mass and T the absolute temperature. Finally as pressure is given by $P = nk_B T$, and the relation between the two velocities c_a and c_{rms} given by $c_a = (8/3\pi)^{1/2} \cdot c_{rms}$ an expression for the rate of adsorption in terms of pressure, mass of molecule and temperature as follows

$$\Phi = \mathrm{P}\left(\frac{1}{2\pi k_B T m}\right)^{\frac{1}{2}}$$

(Eqn – 4.1.3)

and has units of $n_{molecules}cm^{-2}s^{-1}$ As derived in *Ref.* [218]

The Langmuir *L* is a useful unit when considering the amount of contamination present on a surface after a given time in vacuum, where a single Langmuir corresponds to the exposure of a surface at a pressure of 10^{-6} for one second. Whilst the system is at its base pressure of 10^{-11} mbar, one Langmuir of the usual vacuum contaminants (H, CO and N_2) would take several hours.

From a practical point the achievement of ultra-high vacuum is not trivial. Outgassing of the chamber walls presents the largest hurdle in achieving this, and therefore a 'bake' of the entire system at temperatures above 120°C is essential. For this the system is routinely pumped down on mechanical pumps such as rotary pumps in a process known as roughing, leak tested and pumped down to high-vacuum pressures (10^{-6}mbar) by using turbo molecular pumps, leak tested for a second time and then baked for one to three days (depending on the level of outgassing observed in the first two steps). During this process contaminants with low enough vapour pressures at these temperatures can be

pumped away, aiding in eventually reducing the gas load on the pumps and achievement of UHV at a pressure of around 10^{-9}mbar. In order to decrease the pressure further the use of ion-getter pumps is required. Ion pumps are a type of 'capture pump' as the gas is collected and captured in the pumps structure [219]. The use of high voltage to ionise gas molecules and magnetic fields to direct and embed them in reactive targets (primarily titanium) is employed to reduce the pressure of the vacuum vessel. A getter or sublimation pump is then used to reapply a new layer of clean reactive metal for subsequent capture of ions, and to bury the already captured contaminants hindering the possibility of degassing back into the chamber.

The improvement of vacuum systems from those manufactured in glass has aided in the development of a semi-universal (differing only in the use of imperial of metric threads) method of creating UHV seals between chamber components known as the conflat *CF* flange [220]. To create the UHV seal a copper gasket is bitten from opposing sides by a machined 'knife edge' on the flanges. A helium leak test either by mass spectrometry attached to the vacuum chamber or a helium 'sniffer' at the discharge end of the rotary pump is performed to ensure a UHV seal has been made.

4.2 Photon sources

X-ray radiation, since its early discovery in 1985 [221] has proven to be one of the most effective tools used to explore the properties of matter for a wide range of scientific disciplines [222]. As detailed earlier, the quantification of a photoelectric peak in XPS relies on the incident X-ray photon being monochromatic and its energy known. Selecting an appropriate X-ray energy is important for returning various aspects of the sample, for

example ARPES makes use of X-ray energies around the minimum of the so called "universal curve" that relates a photoexcited electrons mean-free path to its kinetic energy [21, 223] in order to gain surface sensitivity. Many photon sources are available such as synchrotron, gas discharge lamps, anode based X-ray tube, and more recently free electron laser sources [224] and none are without their disadvantages. In the following investigations three types of X-ray source are used; the home laboratory is equipped with both a twin anode X-ray lamp and a magnetron based helium plasma source for XPS and UPS respectively, whilst frequent visits to the synchrotron provided the high energy resolution and surface sensitivity necessary for ARPES studies, and the high flux detailed as a necessity for PEEM measurement s[51, 53], aspects of all three will be discussed below.

4.1.1 – Laboratory X-ray source

Some details of the X-ray source (lamp) have already been mentioned in relation to the spectra presented in 2.1.2 namely the resulting spectrum that arises from using such an unmonochromated lamp. For the production of X-rays from this source, thermionic electrons from a hot tungsten filament are accelerated using high voltage onto a water-cooled metal anode. The two most common metals for the anode are Mg and Al with characteristic $K\alpha_{1\text{-}2}$ X-ray emission at 1253.6 *eV* and 1486.6 *eV* respectively. Both cases result from unresolved transitions between $2P_{\frac{3}{2}}$ and $2P_{\frac{1}{2}}$ to the atomic core level sate *1S* however other less intense (higher energy) X-rays are produced due to other electron transitions within the metal anode such as $K\alpha_{3\text{-}4}$. However these transitions are usually neglected as they have intensities ≤1.0% of the $K\alpha_{1\text{-}2}$ peak [225]. Figure 4.1 shows the

emitted X-ray spectrum arising from a magnesium anode where the non-monochromatic nature of X-ray generation is very apparent. The shape of the $K\alpha_{1\text{-}2}$ line is also shown, which for the home laboratory source (VG XR3E2) has a full width at half maximum of 0.7 eV and 0.9 eV for the magnesium and aluminum anode respectively. The lamp is operated at a bias of 15KV and a flux of 20mA at a distance of 25mm from the sample surface.

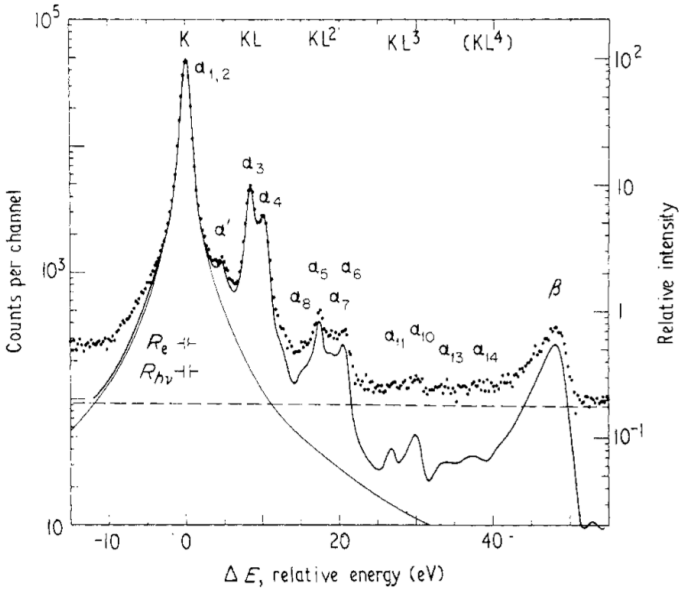

Figure 4.1 Shown is the emission spectra of a Mg anode bombarded with 6KV electrons. Dots show the raw spectrum as obtained in a PAX spectrometer, the broken line the average background height and solid curve the calculated spectra. Also indicated is the shape of the $MgK\alpha_{1\text{-}2}$ emission peak (see ref [9] for details).

Due to the high energy (>1KV) of X-rays produced in this way, core-level electrons (those not involved in chemical bonding) can be excited from the sample. In fact the photoionization cross-section of core electrons in comparison to valence electrons at these energies is so large that the intensity of these peaks dominate the spectrum, and features such as valence states are diminished. The necessity for a low energy source for the study of valence electrons is therefore paramount for the full characterisation of the material under investigation.

4.2.1 Ultraviolet Radiation Source (UV source)

Characteristic emission lines from various noble gases can be used as an excitation source for UPS/ARPES from sources known as a discharge lamps[226]. Resonant fluorescence is produced when the gas is excited and decays, emitting high intensity photons with narrow line widths [227]. A UVS300 Specs high brilliance UV source was used to generate HeI and HeII lines at 21.2 eV and 40.8 eV respectively. The generation of a high density plasma in a small region of the discharge section of the lamp is created by guiding electrons emitted from a hot filament along the lines of a strongly inhomogeneous magnetic field [228] within a partial pressure of the noble gas species required. A turbomolecular pump located between the discharge chamber and a quartz capillary used for extracting the vacuum ultraviolet radiation to the analysis chamber is used to differentially pump the instrument and ensure a working pressure of around 1×10^{-9} mbar in the analysis chamber. This UV source produces a small ≈1mm spot on the sample surface at a maximum induced photocurrent of 200nA.

4.2.2 Synchrotron Radiation

The techniques detailed in chapter 2 of the current work detailed the underlying necessity for high brilliance, tuneable and monochromatic electromagnetic radiation for the probing of different material aspects. Synchrotron radiation emitted as a result of electrons accelerated to relativistic speeds by strong magnetic fields around a evacuated ring was first observed by accident at the Electric research Laboratory on 24th of April 1947 by Pollock and Langmuir[229] although detailed earlier by Schott at Aberystwyth in 1907[230]. Pollock's system was ironically set up to generate X-rays by bombarding a suitable target material with electrons accelerated to high energy [229] and the synchrotron radiation seen as a unwanted source of energy loss in the system.

The first synchrotron radiation based experiments were considered ‘parasitic experiments’ utilising the radiation emitted during other particle physics experiment conducted at the 200 MeV Daresbury synchrotron SRS (synchrotron radiation source) in 1974[231], but never the less proved the viability of synchrotron radiation as an excitation source for photoemission studies.

4.2.2.1 Principle of operation

Clouds of electrons emitted from a hot filament (barium oxide at the MAXlab facility [232]) are accelerated via an oscillating potential along a linear accelerator (LINAC), or in the cases of the ASTRID facility at ISA, a Microtron[233] before entering the storage ring. Within the storage ring the electrons are directed in a circular path by the strong magnetic field of dipole bending magnets. Within this ring they are accelerated further by the use of radio frequency cavities and confined to their path by the increasing magnetic field of the ‘magnet lattice’ consisting of the already mentioned dipole bending magnets, beam-focusing quadrupole magnets and chromatic aberration (caused by the quadrupole focusing) correcting sextupole magnets[229]. More modern facilities add a third ring, exchanging the second rings function from a storage ring into a ‘booster’ ring, from which electrons are injected periodically into the storage ring at full energy in a operation mode known as ‘constant top up’. Facilities that run in this manner allow for the continuous use of synchrotron radiation, where older facilities must periodically dump the beam (due to energy losses within the ring) for a fresh beam insertion.

The act of accelerating electrons to relativistic speeds as they traverse a circular path causes a conical beam of electromagnetic radiation to be emitted tangentially to the path and in the same direction of as the electron motion (figure 4.2 b), as opposed to the isotropic emission observed for electrons traveling below these speeds (figure 4.2a).

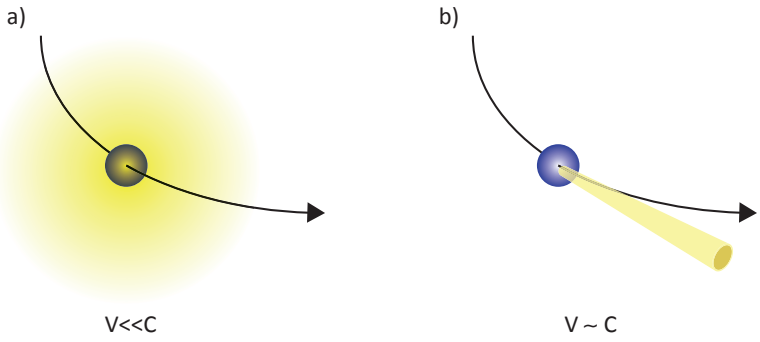

Figure 4.2 Electromagnetic radiation emitted by an accelerating electron at a) below the speed of light *C* and b) close to it.

Although a beam line and experimental station can be placed on a tangential line from the bending magnet, the intensity of such beam-lines is limited due to the flat fan-like profile of the emitted radiation, where the breadth of the fan is related to the angular change of electron path [229]. As detailed earlier the SPELEEM requires high brilliance radiation to image the sample surface at an appreciable resolution, for this reason Insertion devices (ID's) are required, hence the distinction between a 2^{nd} and 3^{rd} generation synchrotron arises[234].

Insertion devices are placed within the straight sections of the storage ring between the bending magnet arc sections; they offer the possibility of extremely high brilliance X-rays that extend far into the KeV range. Two types of insertion devices are used; wigglers and undulators and these are differentiated by the degree from which an electron is diverged

from its straight path[229]. Both devices use a periodic lattice of dipole magnets to force the electrons to oscillate as they traverse through the device (see figure 4.3) creating a forward cone of radiation at the extremities of the oscillation however the principle of amplification is different for the two types.

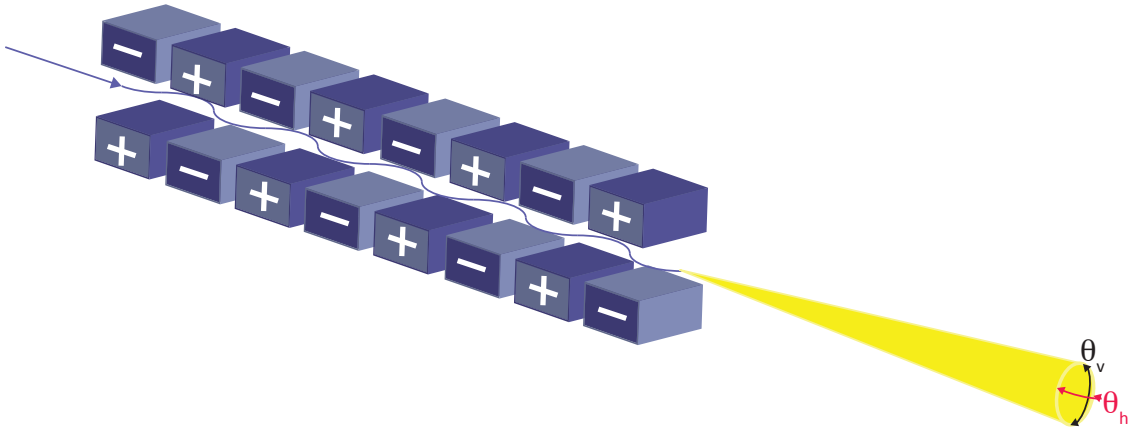

Figure 4.3 Schematic diagram of an insertion device. The angular distribution of the emitted beam is characterised in the horizontal and vertical plane by θ_h and θ_v respectively.

If the divergence angle of the electron is larger than the natural opening angle (that produced by the electron as it traverses the synchrotron) then radiation cones are produced at the extremities of the 'wiggle', as this divergence is large the radiation cones do not overlap (Figure 4.4a). For each period of the magnets the electrons are twice traveling perpendicular to the transmission axis hence the intensity of the output beam is enhanced by a factor of 2N, where *N* is the total number of periods in the wiggler. An undulator differs by utilising a small divergence angle from the natural opening angle. Here the radiation cones at the extremities of the undulation overlap and interfere with each other (Figure 4.4b).

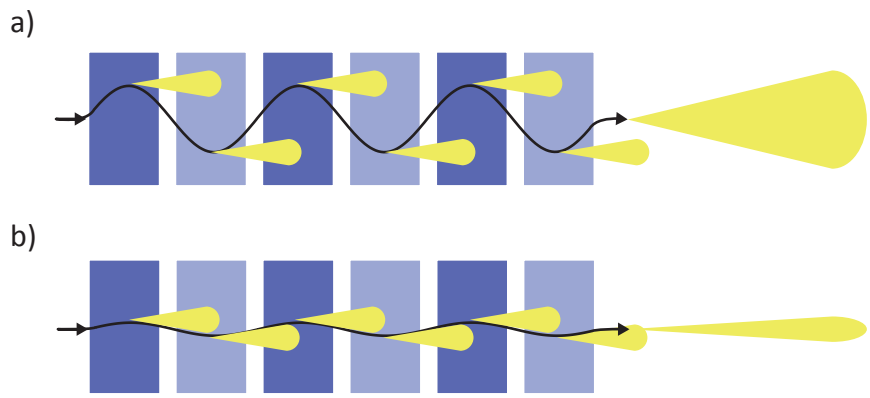

Figure 4.4 Exaggerated schematic of the divergence of electrons from a straight path as they traverse through a) a wiggler and b) an undulator (Figure adapted from *Ref.*[15])

The beam emitted from an undulator is made up of those wavelengths that constructively interfere with each other, meaning that the output spectrum consists of fundamental frequency and other higher order harmonics.

Three different synchrotrons have been used throughout the following investigations; the second generation ASTRID and third generation MAXIII sources are low energy synchrotrons with advantages for ARPES, whilst the third generation MAXII source is a higher energy and larger flux synchrotron capable of reaching the photon energies necessary for core level XPS/XAFS. The properties of each facility are detailed in table 4.1 (details taken from [235-237]). MAXIII differs from the other two sources by making use of 'magnet cells' in which correction coils, quadrupoles (machined to include a sextupole component) and the bending dipole magnet are enclosed in a single unit[238] making the synchrotron very compact. The synchrotrons second function is to act as a test bench for the magnet technology, and its feasibility towards implementation in the upcoming MAXIV 3GeV synchrotron[239].

	ASTRID	MAXII	MAXIII
Circumference (m)	40	90	36
Injection energy (MeV)	100	400	400
Operating energy (MeV)	580	1500	700
Maximum stored current (mA)	286	280	280
Electron beam lifetime (Ah)	15	4	1
Horizontal emittance (nm rad)	9	13	13
Number of straight sections	4	10	8

Table 4.1 Technical specifications of the synchrotrons used throughout the current investigations. For details see the online information available *refs*[21-23].

4.2.2.2 Beamline optics

The optics of the SGM3 and I4 beamlines of ASTRID and MAXII sources will be discussed simultaneously as they provide very similar beamlines with properties designed specifically for high resolution, low energy ARPES. They differ slightly in technical specification but not in layout. Following an undulator insertion device, vertical and horizontal focusing mirrors (VFM and HFM) place the incident radiation through the entrance slit and onto a spherical grating monochromator at grazing incidence (the HFM in the case of SGM3 also acts as a switching mirror to provide light from the undulator ID to neighbouring beamlines). The monochromator facilitates the selection of energies between 14-130(200) eV using three single period crystal gratings, a low energy grating (LEG) 410l/mm(300l/mm), a medium energy grating (MEG) at 1025l/mm(700l/mm) and high energy grating (HEG) at 2500l/mm(1500l/mm) for SGM3(I4). Following the monochromator the incident radiation passes through; in the case of SGM3, a moveable exit slit and onto a final toroidal focusing mirror (TPM) then through a pinhole (typically 300μm[240]) in order to produce a small spot size in the measurement position. Or for I4 the light first passes through a higher order light suppression (HOLS) unit located before

the exit slit and then the final focusing mirror [241] before reaching the sample with a spot profile of 0.1 mm by 0.025-1.0 mm in the horizontal and vertical directions[242].

I311 also of MAXLab although attached to the MAXII 1.5 GeV synchrotron source is capable of providing higher photon energies and the necessary flux for both high-resolution XPS/XAS and PEEM/XPD techniques. The undulator has the possibility of being run in a tapered mode, offering a smoother variation in photon intensity at higher energies, useful for sweeping the incident energy for absorption measurements [243]. Following from the undulator a cylindrical mirror focuses the beam horizontally onto a modified SX-700 plane grating monochromator. The monochromator has been modified with spherical mirror and its movement with the grating controlled to keep the image of the virtual source fixed (no movement of the exit slit position necessary). The spherical mirror also aids in increasing energy resolution, making the beam profile linear instead of curved, and allowing for the suppression of higher order diffractions (by moving the exit slit and at the cost of resolution)[243]. The monochromator is equipped with two primary gratings at 1220 lines/mm for the spectroscopic front station and 330l/mm in order to provide the high intensity necessary for PEEM. These gratings allow for photon energies of 42.5-1500 eV and 50-600 eV respectively[244]. Three spherical focusing mirrors then focus the light before reaching the analysis position in the front end-station. In order to illuminate the sample in the SPELEEM the front station is opened so that the beam can traverse through the analysis chamber and be refocused by two more mirrors before entering the SPELEEM at normal incidence to the sample surface.

4.3 Thin film growth

The manufacture of integrated structures in a single device invariably includes the deposition of materials onto one another. Even the early single MOSFET devices of the 1960's took five steps to complete, whilst the number of steps has only increased as modern devices contain more complex architectures[245]. The variations in conductivity, thermodynamic and chemical reactivity for varying film thickness, as well as exploring the differences between 3D and (quasi) 2D states of matter are some examples of more fundamental reasons for the necessity of investigating thin film materials[246]. Following a brief introduction on the growth modes that arise during deposition, the technology used to do so will be discussed.

4.3.1 Growth modes

The dynamics that take place at the interface of the two materials is of vital importance to the growth of the overlayer and final device performance. In 1958 Ernst Bauer reviewed the interaction and nucleation of materials deposited onto substrates and proposed three different growth modes [247]; Frank-van der Merwe 'layer by layer' (figure 4.5a) in which the material forms complete layers due to the strong bonding between substrate and overlayer. Volmer-Weber 'island growth' (figure 4.5b) where a complete layer is never formed, instead the material clusters and grows vertically due to weak substrate-overlayer interactions. And finally Stranski-Krastanov, in which layer-by-layer growth at the interface is followed by island growth after the initial few monolayers are formed (figure 4.5c).

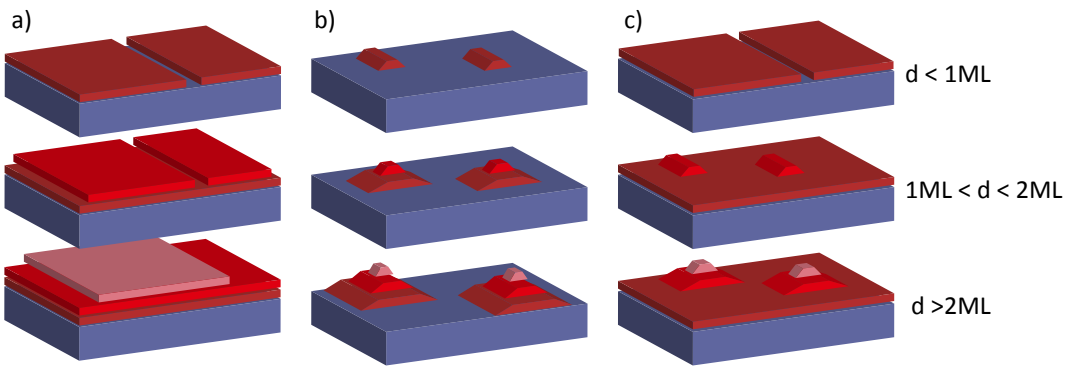

Figure 4.5 The three different overlayer growth modes described by E. Bauer, Frank-van der Merwe (a) Volmer-Webber (b) and Stranksi-Krastanov (c). d is thickness of the overlayer

The reason for the different growth modes relates to the varying surface energies of the materials used, where the bottom layer's (often the substrate's) surface energy is given by γ^B, the adlayer by γ^A and the interface by γ^I [246]. Clustering occurs when adlayer and interface surface energy are less than that of the substrate (*Eqn 4.3.1*), where layer by layer growth occurs if the combined energies are larger than that of the substrate (*Eqn. 4.3.2)*

$$\gamma^B < \gamma^A + \gamma^i \qquad (Eqn - 4.3.1)$$

$$\gamma^B > \gamma^A + \gamma^i \qquad (Eqn - 4.3.2)$$

Layer by layer growth as observed in real-time photoemission studies [15, 16] can be seen as a linear attenuation of substrate core levels when plotted on a semi-logarithmic plot of peak intensity vs. time, whereas as the persistence of the substrate core level during deposition indicates some form of clustering, as observed when monitoring C1s whilst depositing Al on diamond.

4.3.2 Evaporation Sources

There exist a large variety of deposition technologies that can facilitate the growth of materials within both industrial and laboratory environments, including thermal evaporation in vacuum, glow-discharge processes (sputtering and plasma sources etc.), gas-phase chemical processes (CVD etc.), liquid-phase chemical processes (electroplating) and more recently liquid-phase evaporation in vacuum via electrospray has been demonstrated. For more details on the above technologies the user is referred to the book of Kern and Vossen[248] and the references [249, 250]. The following investigations make use of one primary technique, thermal evaporation for physical beam deposition (PVD) in vacuum. A technique that is capable of controllable deposition for a wide range of materials including thermally stable organic molecules[251] to metals[252]. Two sources; a homemade Knudsen-cell and electron-beam evaporators (E-beam) (Specs EBE-4 and Omicron EFM3) were used for the deposition of pure Fe during the following investigations.

4.3.2.1 Knudsen-cell

The Knudsen-cell (K-cell) is a simple device to manufacture and operate. A ceramic crucible containing the desired material is heated by passing current through a Ta wire wrapped around the crucible in vacuum. Here the Ta wire was threaded into ceramic tubes to ensure electrical isolation from each other (heater assembly figure 4.6). A stainless steel shroud around the entire unit ensures that a collimated beam emerges upon the material reaching is vapour temperature within the vacuum vessel, whilst also acting as radiative heat shield. The source is then supported on stainless steel rods fixed to a CF70 vacuum flange.

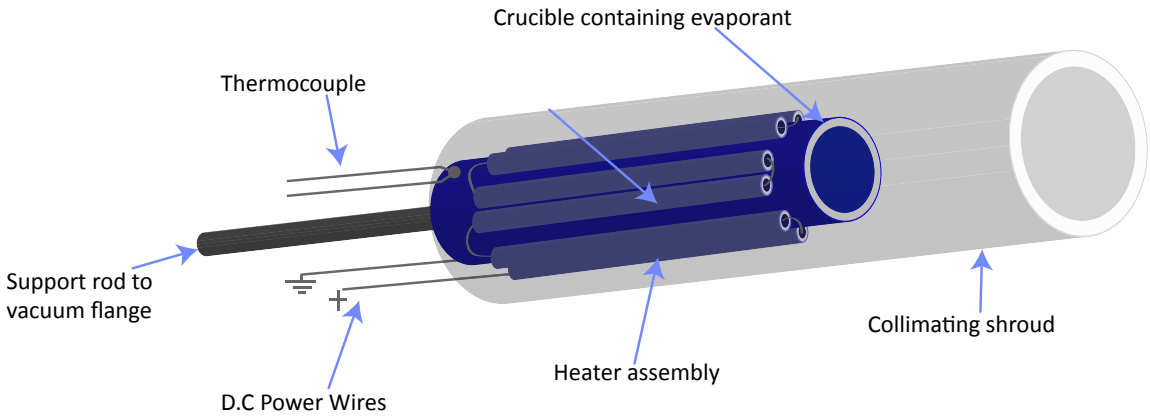

Figure 4.6 A schematic diagram of the homemade Knudsen-cell used for PVD in the Aberystwyth materials laboratory. A shutter was present at the end of the unit to enable control of the deposition time.

Whilst depositing materials with high melting temperatures such as metals, the chamber walls into which the k-cell has been inserted are likely to increase to elevated temperatures, resulting in outgassing of chamber walls and possible contamination of the deposition material. For this reason water-cooling is often employed in order to maintain the high purity of the deposition beam. Another concern for high melting temperature metals is the material of the crucible itself, where ceramics such as Alumina are not permitted due to high outgassing rates above a few hundred degrees [245].

Control over the deposition rate is simply a case of varying the temperature (power) of the K-cell, as measured by a thermocouple in contact with the crucible. Although varied deposition rates are available, a well-calibrated constant rate for a given power is important when growing material and can be calculated via use of a quartz crystal thickness monitor[253] or XPS for thin coverages [223].

4.3.2.2 Electron beam evaporators (E-beam)

Although metals can be deposited using a K-cell, the design of the instrument becomes limited for materials that have very high melting temperatures, E-beam evaporators combat this issue by producing a very localised heating at the end solid rod of material.

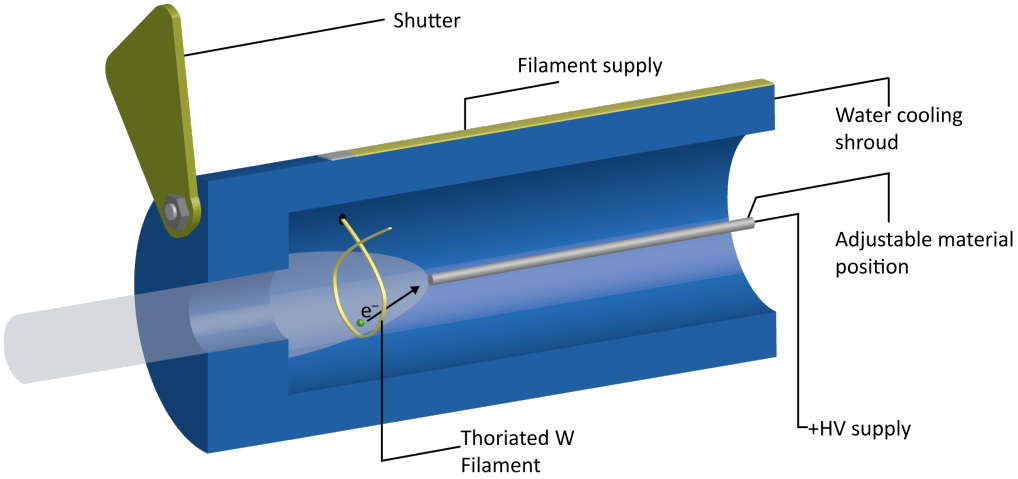

Figure 4.7 Schematic diagram of a UHV e-beam evaporator

This localised heating is achieved by accelerating a cloud of thermionically emitted electrons from a thoriated tungsten filament towards the tip of the deposition material (or crucible) by application of a positive voltage. Efficient water cooling around the evaporent chamber ensures a working pressure of around 10^{-10} mbar [254] for melting temperatures between 200 and 3000 °C, maintaining a very high purity of the material in the molecular beam. Feedback between the high voltage and emission flux allows for a higher degree of controllability than the K-cell, with the adlayer thickness controllable from 1/10 ML per min to 1000ML a second.

4.4 Surface Termination

For the termination of surfaces with specific adatoms, chemically active ionised atoms are preferred, as ground state gas molecules are often too unreactive. Several methods of

creating active gas ions exist, including those already discussed in chapter three with respect to the generation of gas-phase plasma for the CVD growth of diamond and graphene crystals. Plasma sources are categorised into two primary types, thermal and non-thermal sources and both have been used in the following investigations.

4.4.1 Home Laboratory non-thermal plasma source

The home laboratory is equipped with a custom UHV non-thermal plasma source. It is the remnants of the system used by S. Evans at Aberystwyth university during the late seventies [255], and functions much in the same way described therein. Activated hydrogen (H*) and oxygen (O*) can be created by using a source gas mixture of, 50/50 argon in hydrogen or nitric oxide (N_2O) respectively. Argon is used in the hydrogen as it lowers the striking voltage necessary to create the plasma (Paschen's law), in turn ionising the hydrogen (which has a much higher striking voltage). A plasma of N_2O gas is used for oxygen terminating diamond surfaces, as it has been shown to create a more stable flux of oxygen radicals at the sample surface than recombined molecular oxygen [255].

A schematic of the system used is shown in figure 4.8. A brass microwave cavity (MW-cavity) is placed around a quartz tube which enters the small UHV chamber and is sealed by polytetraflouroethylene (PTFE) ferrules within hoke fittings. Manipulation of the MW-cavity around the quartz capillary is possible via orthogonal micromanipulators in order to tune the cavity a tuning pin that changes the internal dimensions of the cavity (hence resonance frequency) also aids this. Compressed air forced around the capillary and cavity was used to cool the instrument during operation.

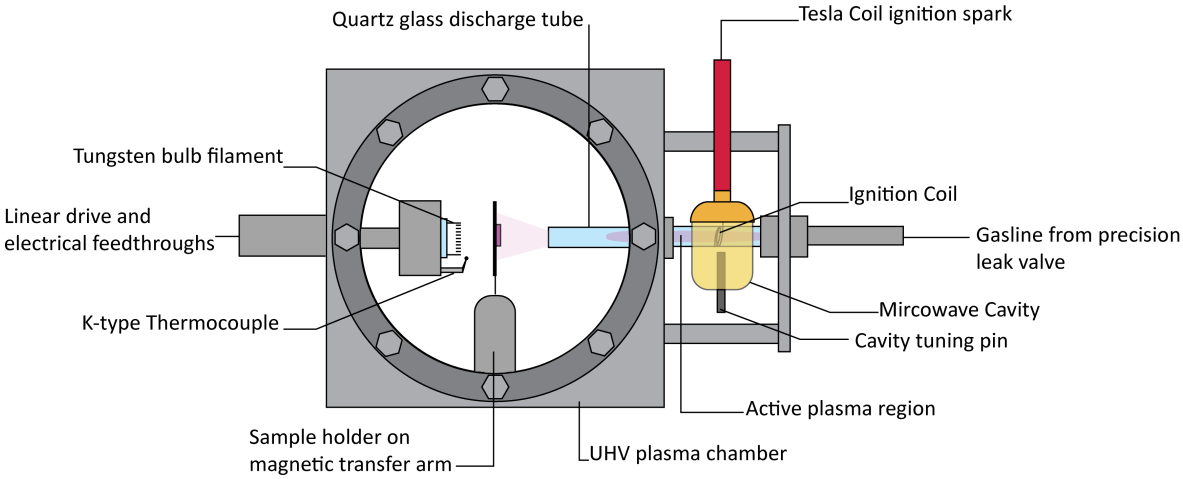

Figure 4.8 A schematic of the custom plasma system used in the Aberystwyth materials science laboratory. See text for details.

Microwaves generated by a 2.45Ghz microtron (EMS200 MKII) were coupled to a reflected microwave power meter, which was used to aid in the tuning of the cavity (lowest reflected power). The microwave cavity lies at a distance of 100mm from the sample position, whilst the end of the quartz tube is 20mm away. A tungsten bulb filament and thermocouple can approach the rear of the sample holder in order to increase the substrate temperature to ~600°C. The thermocouple is placed in good contact with the rear of the sample holder during heating. The hydrogen plasma was maintained at pressure of 6×10^{-4}mbar (measured by Pfeiffer full range cold cathode gauge) excited by 150W microwaves at a reflected power <3W. Hydrogenation of the sample was carried out as follows and is similar to the process used in [256]:

- Gas flow at a pressure of 6×10^{-4}mbar
- Substrate heating to 450°C
- Plasma ignition
- Substrate held at 450°C for 20min
- Controlled cooling of the substrate to 200°C over 20min
- Plasma off, sample cool to room temp pressure recovered to 1×10^{-9}mbar

4.4.2 Tectra H-flux

The Tectra H-flux atomic hydrogen source works by the thermal disassociation of H_2 within a hot tungsten capillary. The advantage of this device is the nearly 100% cracking efficiency of H_2 into H^*[257], however the tungsten filament operates at a temperature of ~2000K and therefore a carries a risk of possible tungsten deposition of on the sample surface. A water-cooling jacket around the source allows the device to deliver a flux of atomic hydrogen $\sim 5\times10^{13}$ atoms cm^{-1} at a pressure in the 10^{-9}mbar scale. A similar temperature profile as to that described above was used during surface termination with this source.

4.5 Sample mounting and heating

Having the sample in good thermal contact with the heater is vital for accurate control of the sample temperature. A custom sample stage and mounting method is used at the home laboratory, whilst at synchrotron beam-time e-beam heating was the primary method of sample heating. Table 4.2 shows the heating methods used in each location.

Location	Heating type	Comments
Home Laboratory	Resistive heating of Boralectric® element	Slow cooling rate below 250°C
I4 - Maxlab	Resistive heating of thin Ta envelope	Often resulted in tilted sampled
I311- Maxlab	ELMITECH E-beam cartridge	Grounded sample, –ve bias filament
SGM3 - ISA	E-Beam	Not possible to heat during measurements (biased sample)

Table 4.2 The different heating methods used at each location for the following investigations.

Figure 4.9 depicts the custom-made sample holder used in the home laboratory. 0.2mm Molybdenum was chosen for the sample holder as it has a high melting temperature, and upon high temperature annealing forms a Mo-carbide on the rear of the diamond sample aiding in grounding the sample/ taking reliable drain current measurements (4.9a). A 0.125mm thick molybdenum (Mo) face plate was manufactured for each sample, for which the surface area of the sample was maximized by use of a circular aperture holding the sample only in the four corners (4.9b). Sliding the faceplate under the folded 'wings' of the sample holder creates a very secure mount for the sample.

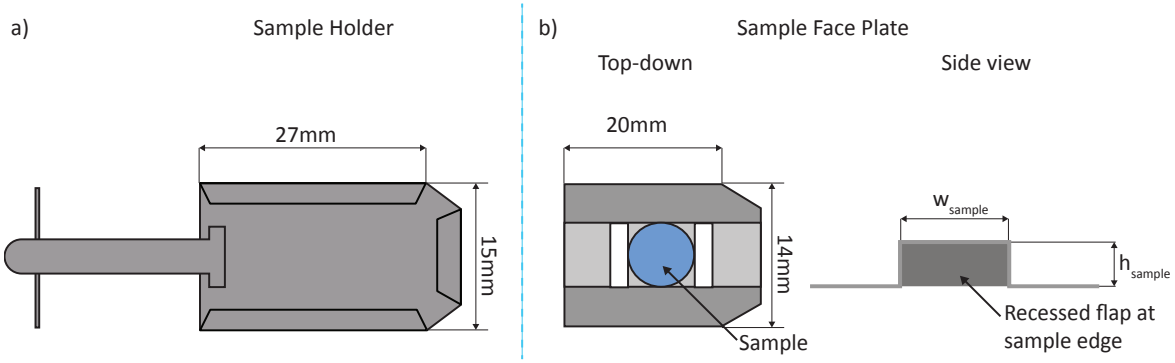

Figure 4.9 Schematic illustrations of the sample holder and faceplate used in the REES system at Aberystwyth.

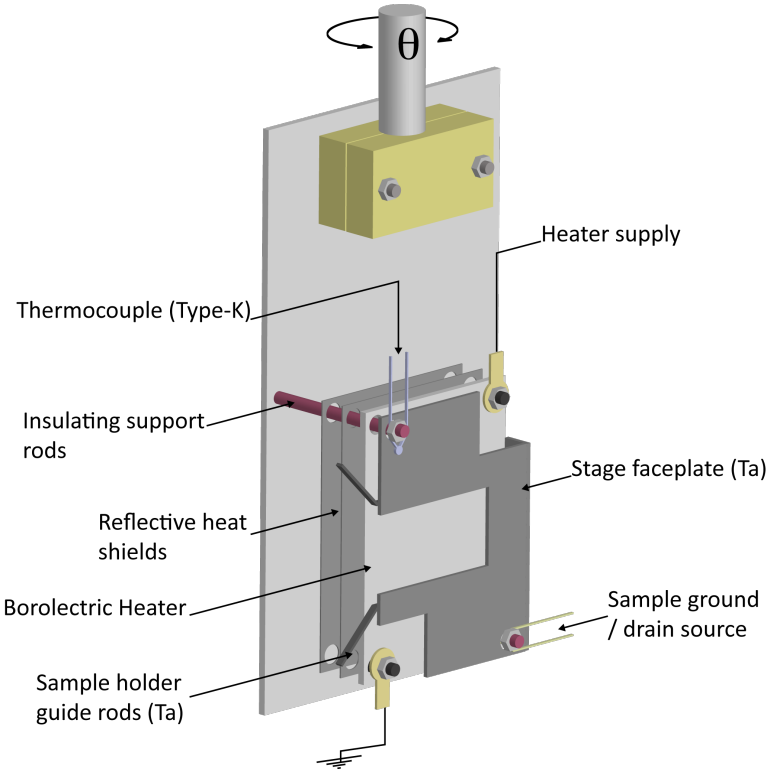

Figure 4.10 Schematic diagram of the heating stage found in the REES system at Aberystwyth materials laboratory.

The heater stage itself (Figure 4.10) is made of a UHV compatible Boralectric® heater, which comprises of encapsulated graphite tracks within boron-nitrate (BN), which is capable of reaching ~1200°C. Connection to the heater is made via Ta rods and Mo washers, whilst the entire unit is supported on insulating ceramic threaded rods. Two stages of reflective heat shields are used to ensure that heating of the connection cables (not shown) that traverse up the rear of the manipulator plate is kept to a minimum. A type-K thermocouple mounted on one of the ceramic support rods and in good mechanical contact with the 0.3mm thick Ta faceplate is used to read the sample temperature, whilst sample ground/ drain source is connected to the other bolt. 1mm diameter Ta wire was spot-welded to the rear of the faceplate to aid in guiding in the sample holder. Constant-current vs time profiles controlled from LabVIEW software via a

programmable Kenwood PDS60-12 regulated DC power supply allowed for repeatable heat-cycles to be performed.

4.6 The REES system

The Real-time Electron Spectroscopy system (technique discussed in 2.1.8) is the main spectroscopy kit at Aberystwyth. The UHV system is composed of three stainless steel chambers and a fast load lock separated by UHV gate valves. A schematic representation is shown in figure 4.11. The analysis chamber (REES chamber) is pumped by an ion pump and TSP combination and achieved a bass pressure of $\sim 5\times10^{-11}$mbar. K-cells containing Fe and C_{60} are located in this chamber and capable of depositing material in the PES analysis position. The cells are equipped with a shutter and are collimated as to avoid contamination of the analyser entrance plane and X-ray head. Also attached are the twin anode X-ray source (4.2.1), the specs UVS-300 UV source (4.2.2), a rear view LEED unit 180° and in line with the electron analyser and Dycor quadrupole mass spectrometer (used only in this work to check vacuum quality and He leak-test). A VG OMNIAX manipulator allows for precise control over sample position and is fitted with the heater shown in figure 4.10.

The transfer (or preparation) chamber provides the main turbo pump for the system through which the entire system is pumped during bake-out. This can be gated off to allow the ion-pump / TSP to bring the chamber down to around the same pressure as the REES system. Knudsen cells containing Au, Ag, and Fe are opposite quartz-crystal thickness monitors at the deposition position, whilst higher up the chamber a linear four point probe is present (currently being commissioned).

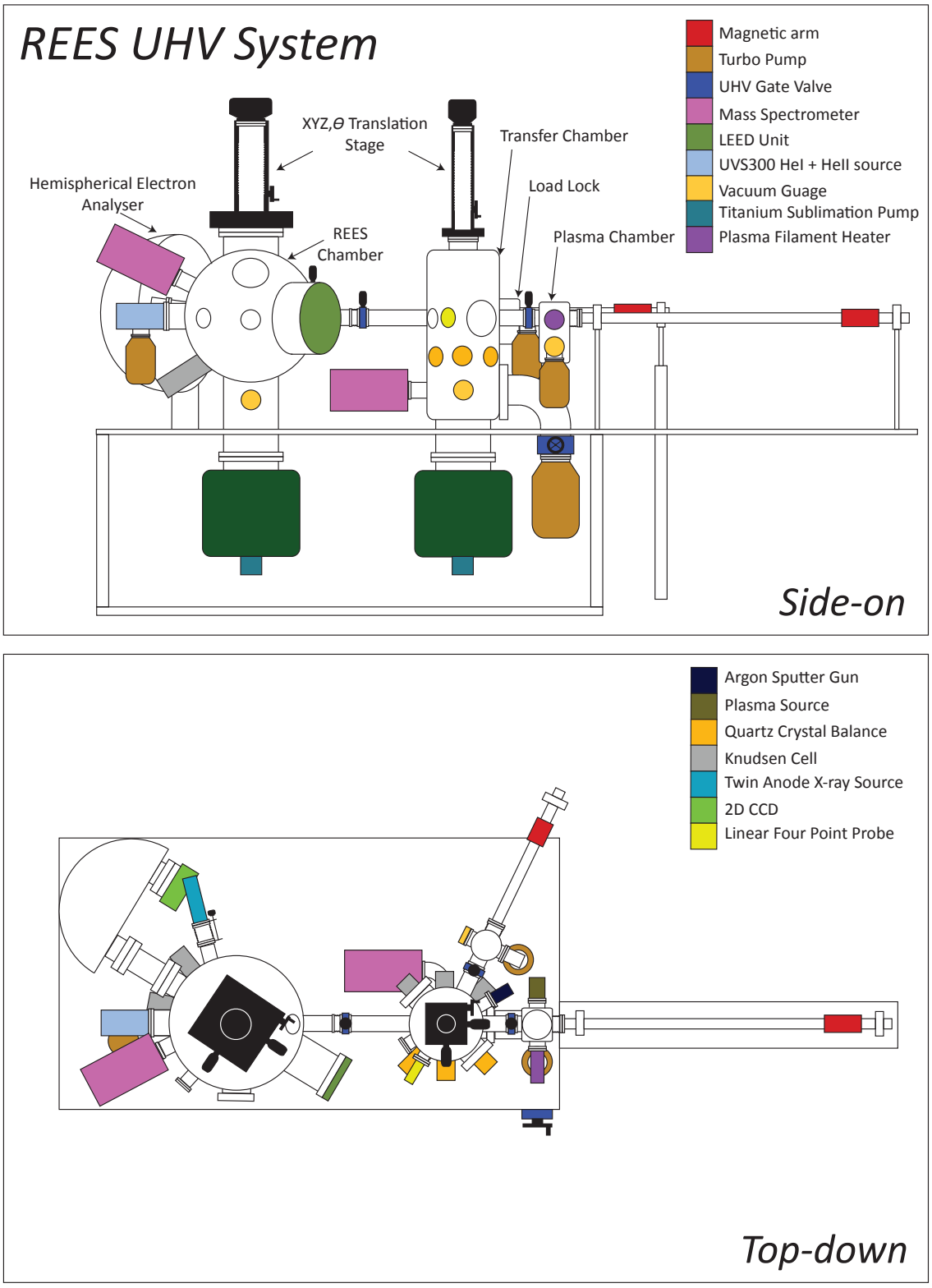

Figure 4.11 A schematic of the REES system at Aberystwyth University. Colour code is used for both top-down and side-on views.

A mass spectrometer and argon ion sputter gun make up the rest of the instruments present. The manipulator is also fitted with the heater shown in 4.10, with the adaption of a second stage below that contains a hole-matrix mask for patterned deposition of the substrate. This chamber also acts as the transfer stage for when a sample is passed from the fast load lock and picked up on the long magnetic arm (accessed from the plasma chamber described in 4.4.1) for insertion into the REES chamber.

¼ inch stainless steel pipe, ferrules and hoke fittings were used to make connections to the various gas bottles, which with the exception of Ar-H mix (12L disposable lab bottle) were fitted with two stage pressure gas regulators, in line with all metal precision leak valves.

The REES systems instrumentation such as ion pressure gauge controllers, heater/ evaporator power supplies and TC-08 thermocouple reader (for heater and K-cell temperatures) are all connected to the REES software interface, either directly via USB or via an analogue to digital interface such as GPIB. This allows the system to log all experimental variable parameters to its corresponding core-level snapshot. The software also allows access to the spectrometer functions such as lens mode, acquisition energy, dwell time etc., which allows for a large versatility to the experiments that can be conducted in this custom system.

4.7 Chapter summary

This chapter has detailed the instrumentation used throughout the following investigations. UHV and its importance for preserving surfaces during measurement, as well as increasing the electron mean free path have been discussed. The three photon sources X-ray lamp, UV-source and synchrotron radiation were presented as well as the different insertion devices and beam-lines used. Thin-film growth was introduced and the evaporation sources used to achieve this. Finally details of the home-laboratory were discussed with attention being paid to the non-thermal plasma source, sample mounting, heating and the overall composition of the system.

Chapter 5 – The clean diamond surface

The review given in chapter 3 made it evident that the growth of graphene is strongly influenced by the underlying substrates electronic and physical structure. For this reason thorough investigations of the bare diamond surfaces were conducted. In order to provide the best possible template for Fe and Graphene growth a clean (1×1) structure of the (111):H diamond surface is required (Figure 5.1). This can be achieved via annealing of the 111 surface in vacuum to temperatures of ~1200 K in order to reconstruct the surface, upon which the surface will be classified as clean. Subsequent re-opening of the closed surface reconstruction via hydrogen termination will then provide the ideal (111)-1×1:H surface[87, 94].

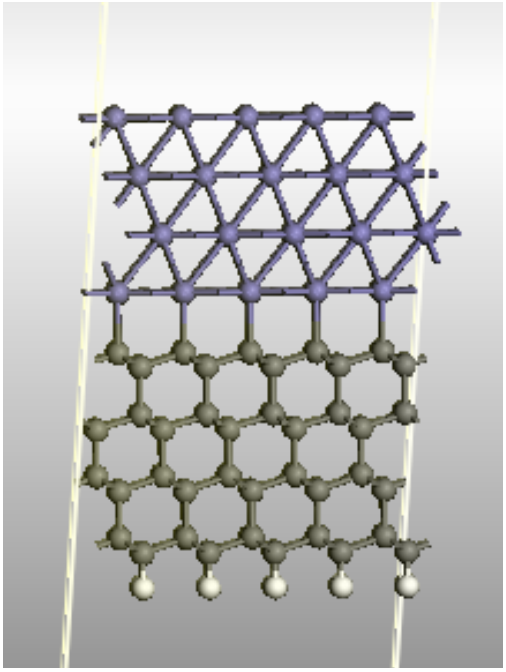

Figure 5.1 Image of the lattice match of diamond and iron, generated from DFT results showing the geometry following optimization of four monolayers ccp-Fe(111) (in purple) on top four monolayers fcc-$C_{(diamond)}$(111)(in green) of which the last layer is terminated by hydrogen (in white). DFT calculated by Dr Karin Larsson of Uppsala University.

5.1 The initial diamond surface

The (111) diamond sample used throughout the following investigations is a type IIb natural single crystal measuring 7 x 4 x 1.5mm. It was polished to within 1° of the (111) plane by Element six (e_6) and showed a surface roughness of <1 nm R_{rms} when measured by contact atomic force microscopy (AFM). The diamond being naturally semiconducting in nature (p-type due to boron dopants at 10^{15} atoms cm^{-3}) provides a sample well suited for both XPS/ARPES and SPELEEM measurements. The latter technique requires conductive samples, as a large potential is applied between the sample and objective lens making insulating diamonds difficult to image.

In all experimental cases the diamond surface was pre-treated with an oxidising reaction involving 10ml (0.18 Mol) sulphuric acid and 0.5g potassium nitrate (KnO_3) held at boiling

point for 10 minutes in order to prepare the O-terminated surface. The sample was then subjected to 10 minute ultrasonic wash in DI water followed by 5min ultrasonic wash in acetone, flushed with methanol then isopropanol quickly followed by blow drying the sample in dry nitrogen gas. The sample was then degassed in the preparation chamber to a temperature of ~500 °C and held their until the pressure in the chamber recovered to ~1×10^{-9} mbar before performing any analysis. Sample temperature in all cases was measured by a type-K thermocouple mounted close to the sample position.

5.1.1 Results

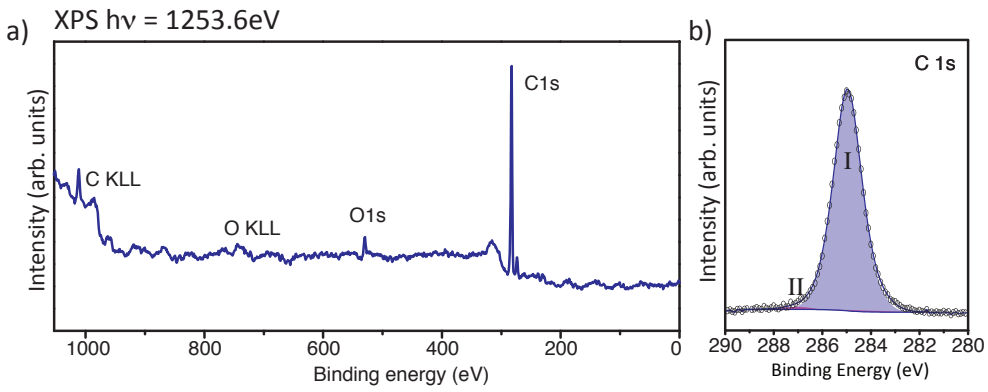

Figure 5.2 a) a survey scan for the diamond (111) surface following a 500 °C anneal and a b) high resolution C1s taken at 20eV pass energy.

Component	Line shape	Position (eV)	FWHM (eV)	At %
(I) sp^3 Carbon	Sum Gaussian-Lorentzian	284.8	1.38	99
(II) C-O/C=O	Sum Gaussian-Lorentzian	286.9	1.44	1

Table 5.1 details the components and parameters used to fit the C 1s photoelectron peak shown in figure 5.2b

The sample following an anneal at 500 °C in the preparation chamber still shows some evidence of oxygen on the surface as seen in the survey scan 5.2a however the dominant feature is the C1s. Quantification reveals a chemical composition of 5% oxygen

corresponding to around 1ML oxygen on the diamond surface. High resolution C1s (5.2b) taken at $E_{pass=}$ 20 eV shows the C1s located at 284.8 eV (see parameters in table 5.1) with a component towards the higher binding energy side that, whilst improving the fit did not have sufficient area to be included in the quantification, however C-O and C=O bonding would be located on the higher binding energy side of the peak.

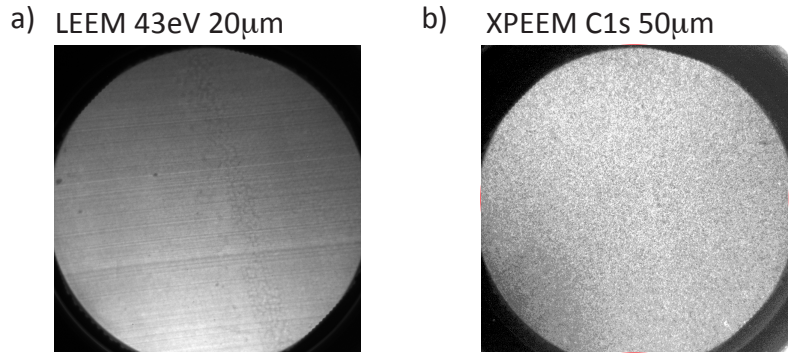

Figure 5.3 a) LEEM and b) XPEEM image of the C1s photoelectron following in vacuum annealing to 500 °C in SPELEEM prep chamber

Figure 5.3 shows LEEM and XPEEM images taken using the Elmitech SPELEEM available at i311 MAXlab. Bright field LEEM image taken at 43 eV (5.3a) shows a very flat surface in which contrast is generated by changes in the physical structure of the surface. The primary features are the lateral lines running along the diamonds length, most likely resulting from the polishing procedure used by e_6. Surface sensitive XPEEM hv=330 eV was used to image the C1s core level (E_{kin}=40 eV) showing the surface comprises of a single form of carbon and free from sp^2-like regions.

The sharp and bright spots of the (1x1) LEED pattern (figure 5.4a) indicate the surface is of superb crystallinity and as expected from the corrugated (111) surface the (10) and the (01) diffraction spots have different LEED-IV profiles corresponding to different Bragg conditions for the surface and 2^{nd} layer atoms.

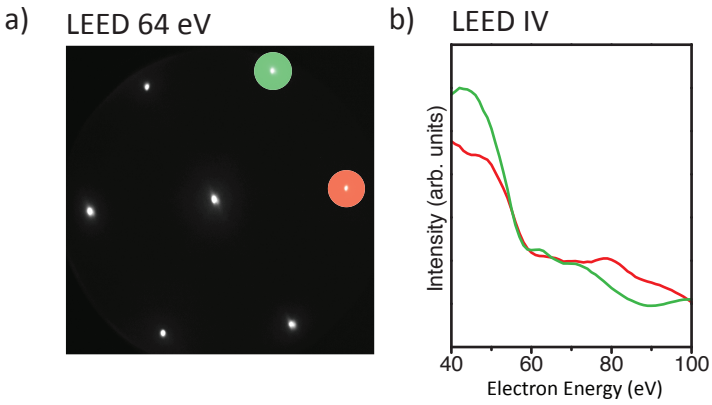

Figure 5.4 Shows a) LEED image at 64eV taken from LEED IV image series, and b) LEED IV profiles of the (10) in green and (01) in red LEED spots. The IV profiles are colour coded with the circles in a)

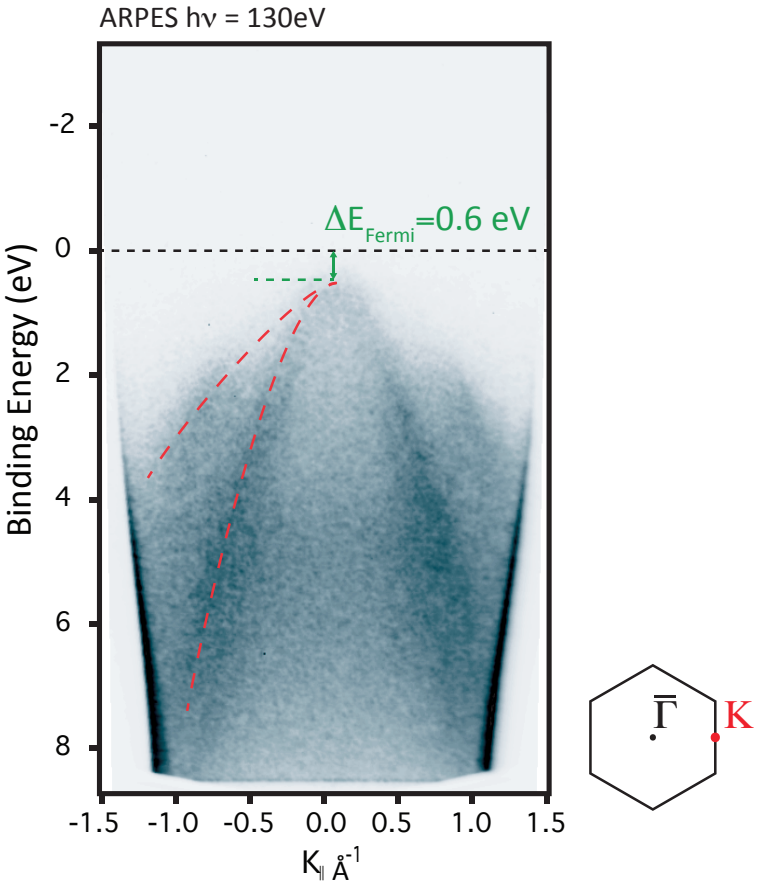

Figure 5.5 Angle resolved photoemission image taken along $\boldsymbol{K} - \bar{\Gamma} - \boldsymbol{K}$ for $C_{diamond}$(111) hv=130eV. The top of the valence band maximum is observed 0.6eV below the Fermi-level. Two dashed red curves have been added to indicate the two bands of the diamond σ-states.

Angle resolved photoemission data taken around normal emission for the as prepared surface is shown in figure 5.5. The top of the σ-band for diamond (111) at $\bar{\Gamma}$ is shown lying

0.6 eV away from the Fermi level (as measured on Ta foil within the system). The outer σ-band (heavy hole band) appears brighter than the outer band due to differences in their photoemission cross section at this energy [93, 258].

5.1.2 Discussion of the clean surface results

The data presented in figures 5.1 – 5.5 give a clear indication of the quality of the substrate used. Following only a 500 °C anneal the diamond appears be clean from atmospheric contamination and terminated by an oxygen monolayer. The C1s shows only a small component at higher binding energy of the main sp^3-carbon component when fitted with a voigt-function. The smaller component is attributed to oxygen bonding to the diamond surface [255], however the type of bonding was indistinguishable as the component falls to within sensitivity limit of the measurement technique. A FWHM of 1.38 eV is broad for the diamond however is typical for diamond surfaces measured in this system after similar procedures [259].

The topography and chemical composition of the surface were imaged in LEEM and XPEEM. With the pass energy of the system set to 0.5 eV, a shift of only a few tens of an electron volt in the imaged peak's kinetic energy would result in a significant contrast change in the image formed, figure 5.3b thus shows that the surface is comprised of a singular C1s component. Some shading is visible towards the edges of the image and is due to the imaging analyser dispersing energy across the image. The only features visible in the LEEM image are the polishing lines running along the length of the crystal, they are ~0.5µm in width most likely the size of diamond polishing grit used during the polishing procedure.

The reciprocal structure of the surface was probed with both LEED and ARPES. Electron diffraction measurements suggest that the diamond surface is of high crystal quality indicated by the small and bright spots in figure 5.4a. As described in 3.1.2 the (111) surface is comprised of a buckled hexagon at the surface, this corrugation in the surface leads to characteristically different Bragg conditions resulting in differing intensity profiles for three spots (separated by 120°) of the observed diffraction pattern 5.4b. The energy of 64 eV was therefore chosen to show the reciprocal structure with all spots at comparable intensities. ARPES data taken around $\bar{\Gamma}$ shows the valence band maximum at ~0.6 eV below the Fermi-level, this is in good agreement with the experimental data detailed by Pate (See Ref [93]) at around 0.8 eV below E_f. The difference is most likely due to different dopant or impurity density within the crystals used in this early work.

No evidence of surface reconstruction is seen following this preparation step, the surface determined by LEED, ARPES and XPS is therefore the (111)-1×1:O surface however the configuration of the oxygen bonds (single or double bond) is unknown, although most likely to be C=O as suggested in the literature [260].

5.2 The (111) Surface reconstruction

In order to reconstruct the surface high temperature annealing at good vacuum pressures are a prerequisite. In the case for the (111) diamond surface, reconstruction requires temperatures in excess of 1200°K for which the partial pressure of hydrogen in the system must be low. Results following such an annealing cycle are presented below.

5.2.1 Results

The sample was subjected to three heat cycles of ~800°C for 30min in order to improve the vacuum pressure at high temperature (P(T=800°C) = 5×10^{-9} mbar), the sample was then heated to ~930°C for 5min during which time the pressure increased to 5×10^{-8} mbar. Cooling the sample to ~800°C and holding it at this temperature ensured that few contaminants could re-adsorb on to the surface. This temperature was maintained until the pressure recovered to at least 5×10^{-9} mbar. The sample was then cooled to room temperature to perform XPS measurements.

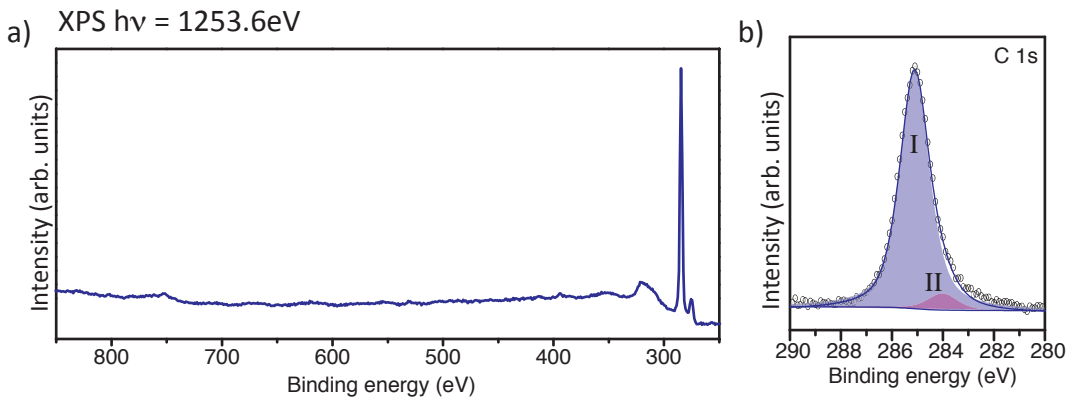

Figure 5.6 shows a) survey scan and b) high resolution C 1s core level, following reconstruction of the surface by annealing the substrate to ~920°C

Component	Line shape	Position (eV)	FWHM (eV)	At %
(I) sp^3 Carbon	Sum Gaussian-Lorentzian	285.1	1.3	92.7
(II) sp^2 surface component	Sum Gaussian-Lorentzian	284.0	1.4	7.3

Table 5.2 details the components and parameters used to fit the high resolution C1s photoelectron peak in figure 5.6b

The XPS survey scan presented in Figure 5.6 shows only the C1s component and its related spectral features (plasmons etc.)

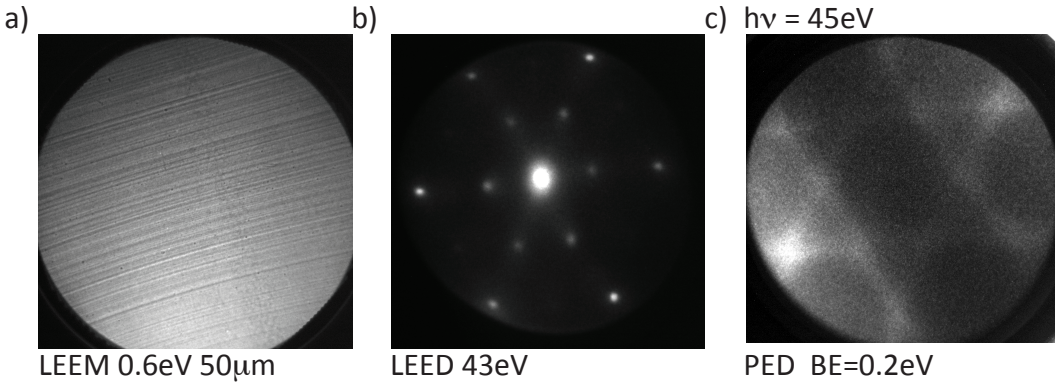

Figure 5.7 images taken for the diamond surface following a 1.5 hour anneal at 800°C and flash to 970°C. a) LEEM showing polishing lines b) LEED showing threefold rotations of the 2x1 surface reconstruction, and c) PED constant energy slice taken 0.2 eV below the Fermi

Figure 5.7 details some of the experimental data taken following; a 1.5hour 800 °C degas cycle followed by a quick ramp (10 °C/s) in temperature until reaching 970 °C. During the whole procedure the pressure in the preparation chamber did not increase above 5×10^{-9} mbar. Cooling of the sample was performed in a similar way to that described for the XPS measurements of figure 5.6.

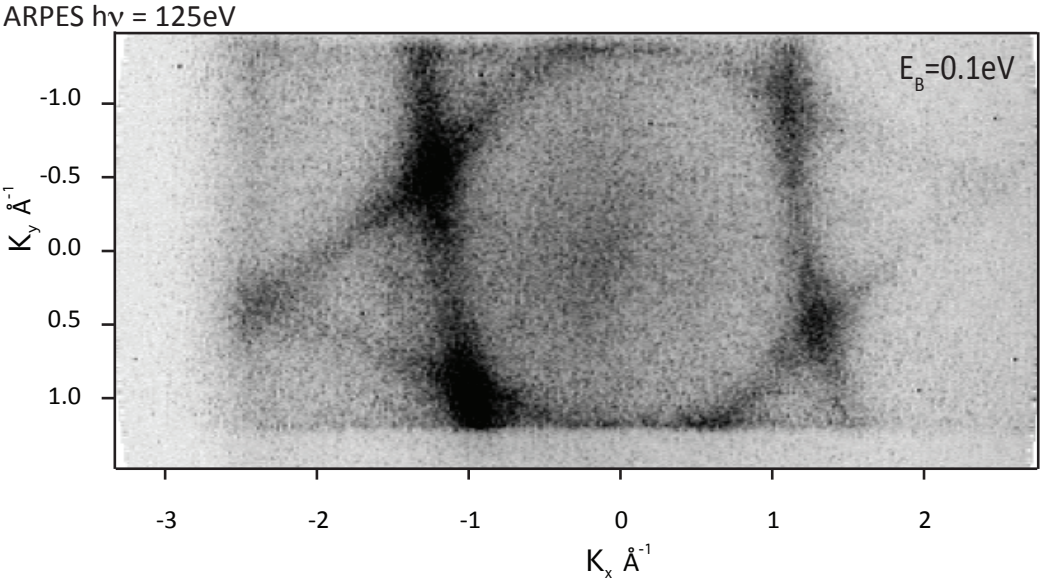

Figure 5.8 constant energy slice of K_{II} 0.1 eV below E_{Fermi}. The electronic structure observed shows categorically that the surface is composed of three rotational domains of the Pandey (2×1) reconstructed (111) surface.

The ARPES data presented in figures 5.8 – 5.12 follows from reconstructing the surface in the preparation chamber of the SGM3 beamline of ASTRID, ISA. The sample was heated

to 800 °C until the pressure recovered to ~2×10^{-9} mbar and then flashed to 1000 °C using E-beam heating. The maximum pressure in the preparation chamber at this temperature was ~1×10^{-7} mbar and is most likely a result of the manipulator out-gassing. The sample was therefore cooled slowly as to avoid re-adsorption of contaminants on to the surface during pressure recovery.

Figure 5.8 shows a constant energy slice i(K_x, K_y) taken 0.1 eV below the Fermi level. The hexagram shape observed (shown schematically in figure 5.9) does indeed cut the Fermi-level, (see Figure 5.10) however the contrast for all surface states is much better slightly below E_{Fermi}.

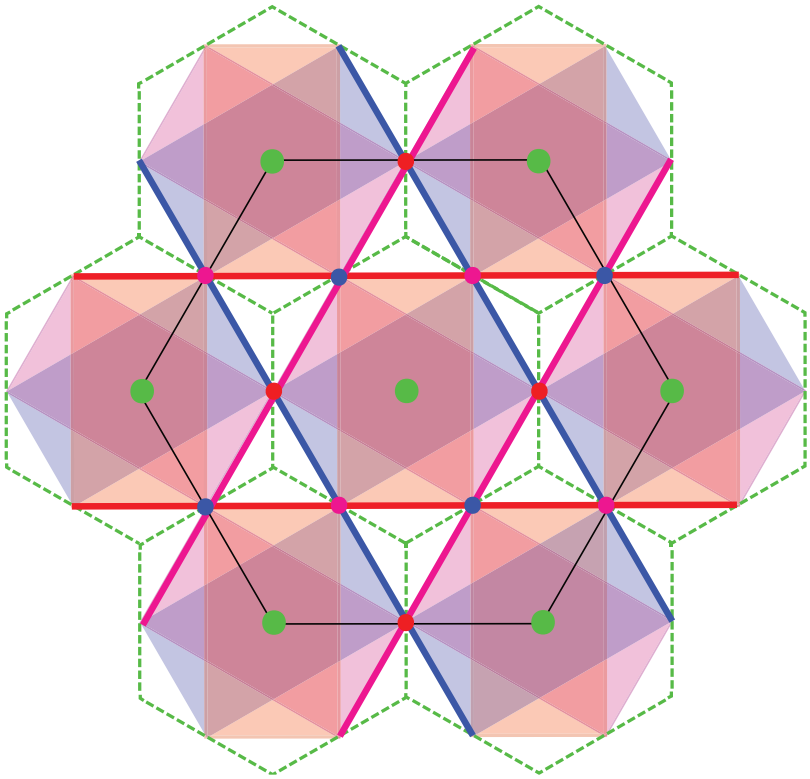

Figure 5.9 Schematic showing the accumulation of the electronic surface states at the Fermi level for three rotational domains of the Pandey (2×1) surface reconstruction across seven 1x1 Brillouin zones.

The slice indicated by the thick black line in the surface Brillouin zone schematic of Figure 5.10, allows for a i(E,K) cut to be taken through the data set which includes two K-points

of the surface reconstruction π-states at K_{II}=1.44 $Å^{-1}$ whilst crossing $\bar{\Gamma}$ showing any influence of the reconstruction on the diamond bulk σ-bands.

The slice taken in figure 5.11 was chosen as an equivalent slice to the data set shown in Graupner's review (See ref[88]). Laid over the figure is the theory and experimental data from the report, which was added by scaling the axis of the data presented in their work until they matched in energy and momentum to the ARPES slice presented in this work and overlaying new symbols which matched the original experimental and theoretical data points.

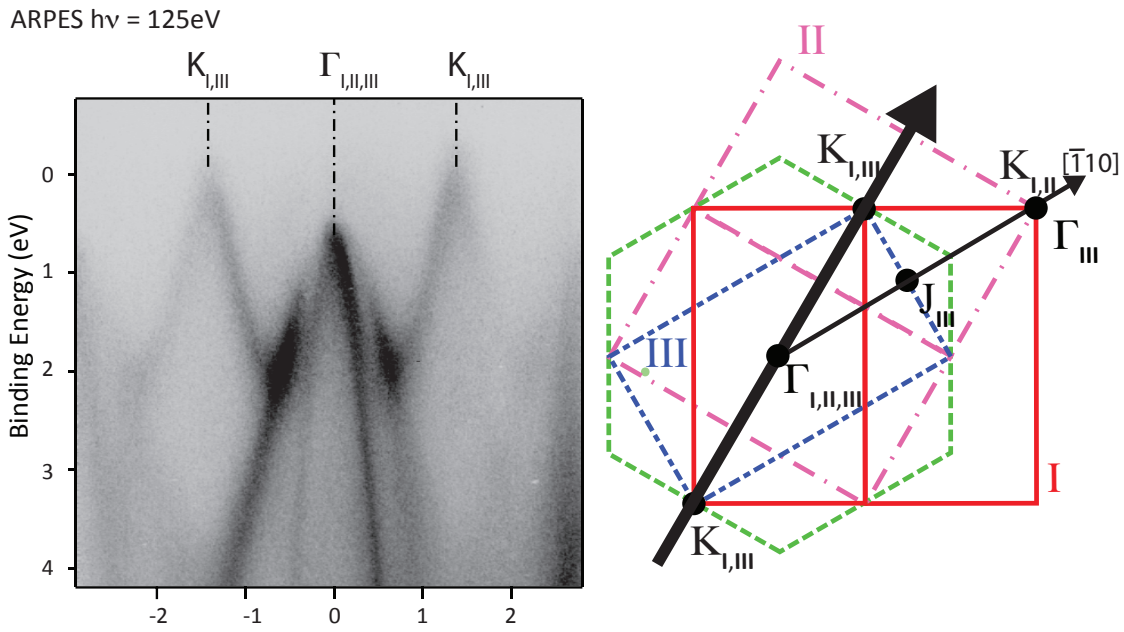

Figure 5.10 The I(E,K_{II}) dispersion for the reconstructed diamond surface. The direction of K_{II} through the surface Brillouin zone is shown as the thick arrow in the accompanying schematic.

Figure 5.12a shows a particular slice along an equivalent $[\bar{1}10]$ direction, in this case labelled $[10\bar{1}]$. The cut indicates second state approaching the Fermi level in between the surface reconstruction high symmetry points J_I and $K_{II,III}$ taken from the common Brillouin zone centre $\Gamma_{I,II,III}$. 5.12b was taken from a second ARPES data set in which the

diamond was tilted 29° forwards with respect to the dispersive plane of the analyser. This was done in order to capture K-M-K for graphene whilst maintaining light intensity by decreasing the necessity to perform large polar scans.

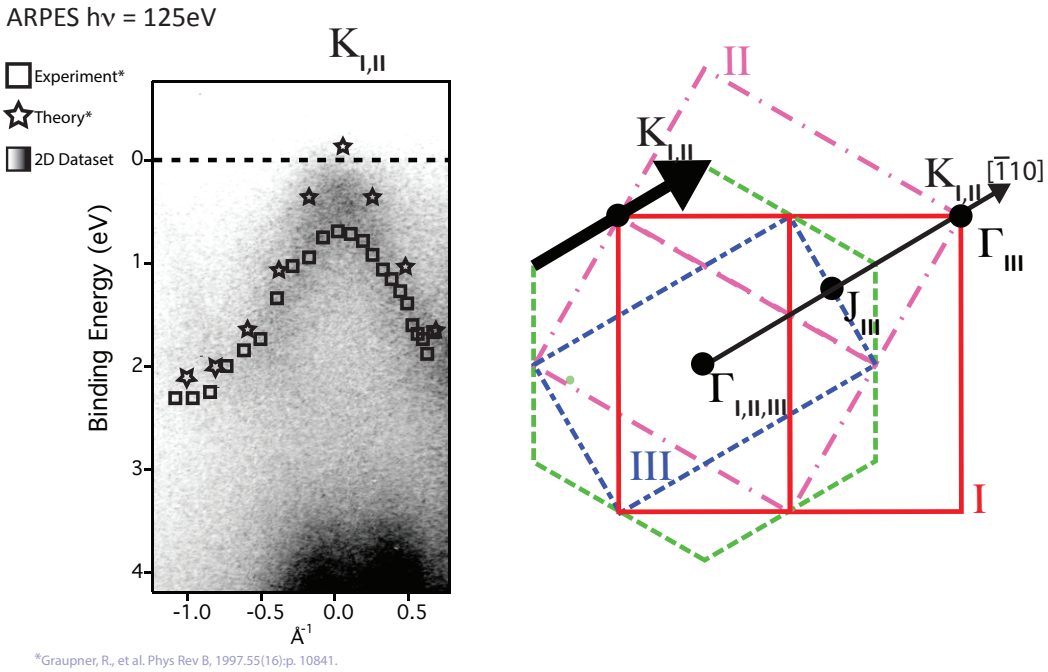

Figure 5.11 The I(E,K_{II}) dispersion for an equivalent cut as the theory and experimental data presented in Graupner's article see *Ref.* [5]. The bold arrow in the accompanying Brillouin zone schematic depicts the equivalent cut taken through the surface, along $[\bar{1}10]$.

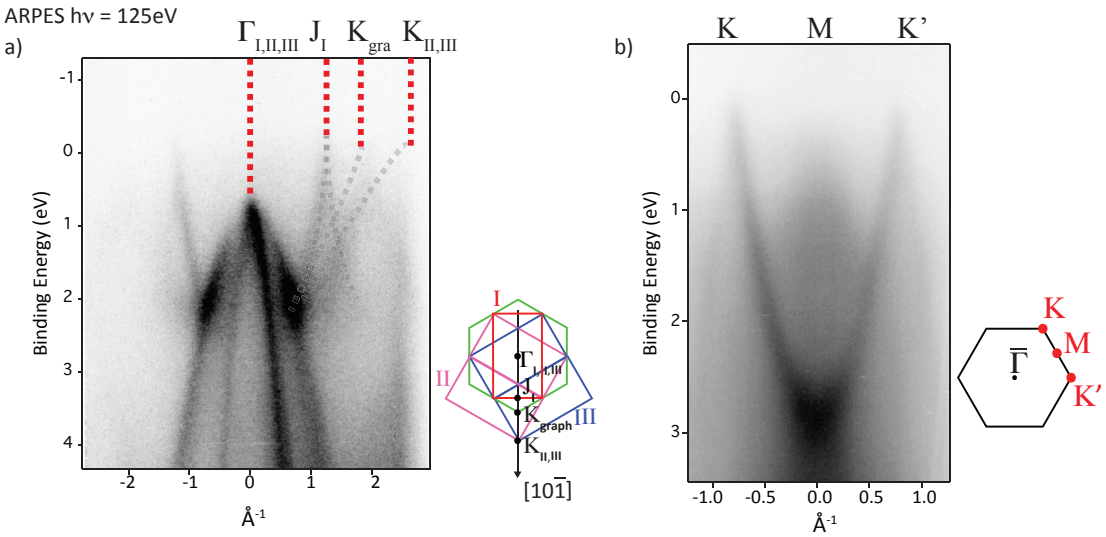

Figure 5.12 a) A cut through the data set along $[10\bar{1}]$ shows a faint feature approaching the Fermi level around the K-point of the unreconstructed (1×1) surface Brillouin zone. b) Second ARPES series of the reconstructed surface in which the sample was tilted 29° (in order to maintain light intensity over small angle series) from normal incidence in order to scan K-M-K direction of graphene Brillouin zone (see figure 3.7)

5.2.2 Discussion of the reconstructed surface results

The XPS data presented in figure 5.6 shows the surface is free from any contaminants, whilst the second component of the C1s at ~284 eV is indicative of sp^2-bonded carbon and in close agreement (±0.2 eV) with the other sp^2 bonded carbon materials[261] The LEED pattern shown in figure 5.7b shows second order spots as a result of the surface reconstruction. This LEED pattern is now categorically formed as a result of three rotational domains of the 2×1 Pandey-chain and not the buckling model [92] or 2×2 reconstruction [93], due to evaluation of the photoelectron diffraction (VPED) image shown in figure 5.7c and the ARPES data presented in this section.

The hexagram observed in 5.7c and 5.8 both result from constant energy slices $I(K_x,K_y)$ taken close to the Fermi level (as referenced to the Fermi-edge on freshly deposited Fe and Mo respectively). The effect of accelerating the emitted photoelectrons to 1800 eV in the imaging column of the SPELEEM allows for the band structure to be imaged at a constant kinetic energy for the same reciprocal distance shown for the LEED patterns ~5×5 $Å^{-1}$. The ARPES performed at the ISA facility only captured one of the longest K-J-Γ-J-K directions however due to symmetry, equivalent K-points to those presented in Graupner[88] and Pate's [93] related work can be analysed. The extended band structure is not captured due to the large polar angles necessary, even at comparably high incident energy (hv=125 eV) and consequent intensity decreases as a result of the low collection angles.

Figure 5.9 is a schematic used to demonstrate how the accumulation of all the strongly dispersing surface states (those along Γ – J the short edge of the rectangular

reconstruction *see 3.1.2*) accompanied with three equivalent 60° rotated domains is capable of producing the pattern observed close to E_f. The diffraction spots for each rotation of the 2x1 surface, as would be observed in LEED (figure 5.7b) are also shown in matching colours to their respective Brillouin zones. All of the diffraction spots were visible in the LEED pattern, however it was necessary to set a very high contrast level to the image in order to see those located between the original 1×1 reciprocal lattice sites.

Contrary to the work of Graupner the π-states presented here cut the Fermi-level at K_{II} =±1.44 $Å^{-1}$ clearly showing that they are in fact metallic. This challenges his prediction of an energy gap of at least 0.5 eV for this reconstructed surface[88]. This result indicates that no dimerization between the surface atoms within the π-bonded chains has occurred as dimerization causes a shift of the state to higher binding energies. The metallic nature of the states indicates that the chains also flat, as tilted chains such as those seen for the 2×1(111) silicon surface also induces a gap in the surface state bands[89]. The experimental results presented here agree well with the theoretical calculations presented by Kern (see *Ref.*[87]), however there is an apparent gap between E_f and the top of the π-states around Γ of 0.7 eV (see figure 5.10). A possible explanation of this shift to higher binding energy is touched on in Pandey's original review, and is related to the bond length along the reconstructed chains. He states, "*A variation of the bond length along the chains has very little effect on the bands near* $\bar{J} - \overline{K}$*. It affects, mainly, the splitting of the bands near* $\bar{\Gamma}$ *which decreases (increases) with in-creasing (decreasing) bond length[92]."* Suggesting that the dimer length along the chain is short on this particular sample. It is thought that this result is likely linked to the proximity at which the diamond surface is polished to within the true (111) plane. If this angle is large, step

edges along the surface would cause a variation of bond lengths along the reconstruction. In the case of this diamond, the surface was polished to within 1° of the (111) plane, as a result the 2×1 reconstruction can accommodate a short dimer length inducing this downward shift.

An unexpected result from this reconstructed surface came in the form of evidence of surface graphitisation, or more correctly the detachment of graphene regions from the reconstructed surface. This was made evident by taking a slice along $[10\bar{1}]$ where a second feature approaches the Fermi-level $\sim K_{II}$= 1.71Å^{-1} (see figure 5.12a), The location of this second feature at E_f agrees well with the distance between the Brillouin zone centre and the W-point of diamond (see figure 3.2) or K-point of graphene at $\sim K_{II}$= 1.77 Å^{-1} [176] Indicating the graphene is in good registry with the substrate. A second ARPES series was then conducted in order to collect data around two of graphene's Dirac points. Due to the cross section of diamond's electronic states changing rapidly below hν = 50 eV [91] a photon energy of 45eV was chosen to achieve good contrast between the graphene π-band and the diamond's spectral features. Figure 5.12b shows the results of the series. A cut was taken along the K-M-K direction of graphene's Brillouin zone (see figure 3.7b), the image clearly shows the un-doped π-band of graphene intersecting the Fermi level, whilst the large intensity increase at the M-point ~3 eV is most likely due to interband transitions between the diamond's electronic states (shadowed grey area) at this photon energy [91]. The distance between the K-points centred on M is $\sim K_{II}$=1.61 Å^{-1} as expected for graphene, however this value does not exactly match with that of the W-W direction of the 1×1 Brillouin zone of (111) diamond (~1.77 Å^{-1}). One possible reason for the discrepancy in the values seen for the K-K distance in graphene and the Γ-W distance in

diamond is due to errors induced by k-warping the larger collection angles of the spectra, however other possibilities exist. One such possibility is the expansion of the real-space graphene hexagonal lattice as it relaxes into its 2D form, from that of the buckled 1×1 diamond hexagon, inducing a small shrinking of the graphene reciprocal lattice.

The question of whether the carbon was detached from the surface or formed by some other mechanism is an important one. Details have already been discussed in chapter three in regards to graphitising the surface, where it was suggested that temperatures in excess of 1500 °C are required for this [96]. The graphene could therefore form as a result cracking some gas phase carbon such as CO onto the diamond surface at high temperature in vacuum pressures of 1×10^{-7} mbar (where CO is likely to be a large contributor to the overall vacuum pressure).

5.3 Hydrogen termination and generation of the 1×1:H surface

As mentioned earlier the desired surface for deposition of Fe as calculated via DFT* is the 1×1 structure of the (111) diamond surface. It is already well discussed in section 3.1.3 that atomic hydrogen provides a mechanism of recovering the 1×1 surface following reconstruction to the 2×1 at high temperature; the results of such experiments will be presented here. The results allow for investigation of another phenomenon associated with hydrogen-terminated diamond, the induced negative electron affinity NEA.

5.3.1 Results

Following from analysing the reconstructed surface the sample was transferred back to the preparation chamber of the SPELEEM for hydrogen dosing. A Tectra H-flux® was used as a source of atomic hydrogen. A flux of 15nA was maintained for 30 minutes with the sample held at 300°C. The sample was cooled over the final ten minutes whilst still within the atomic hydrogen flux. The pressure in the chamber was held constant at 1×10^{-6}mbar and allowed to recover well into mid $\times10^{-10}$ mbar scale before transferring into the analysis chamber.

Figure 5.13 The surface following atomic hydrogen adsorption a) LEEM image of the surface shows no structural degradation of the surface following the procedure. b) LEED image shows the re-emerging (1×1) surface configuration. c) XPEEM image of secondary electrons at E_{kin}=0.5 eV image is a factor of 10 more bright than comparison to secondary images taken for previous steps.

It can be seen that following hydrogen treatment the surface remains topographically unaltered as shown in the LEEM image (figure 5.13a). The 1×1 electron diffraction pattern observed in figure 5.13b indicates that hydrogen termination has removed the reconstruction whilst an image of the secondary electrons at E_{Kin}=0.5 eV confirms that there is a large increase in the number of secondary electrons as the image was taken at a significantly reduced integration time than that required to achieve an image of this intensity for previous steps. A large increase of the secondary electrons emitted from the diamond surface, being a key indicator of a hydrogen terminated surface [105].

In the home laboratory the sample was subjected to hydrogen plasma (as detailed in section 4.4.1). The sample was heated to ~450 °C subjected to the H/Ar plasma for 20 minutes then cooled in the hydrogen flux to around 200 °C over 20 minutes. The pressure in the plasma chamber was maintained at 1×10^{-4} mbar and allowed to recover until the chamber reached mid $\times10^{-7}$ mbar scale.

Figure 5.14 details the results following this procedure. High resolution C1s (5.14a) taken at E_{Pass}=20 eV shows a single component of the C1s located at 283.9 eV resulting from the removal of the second component shown in 5.6b attributed to the surface sp^2-carbon.

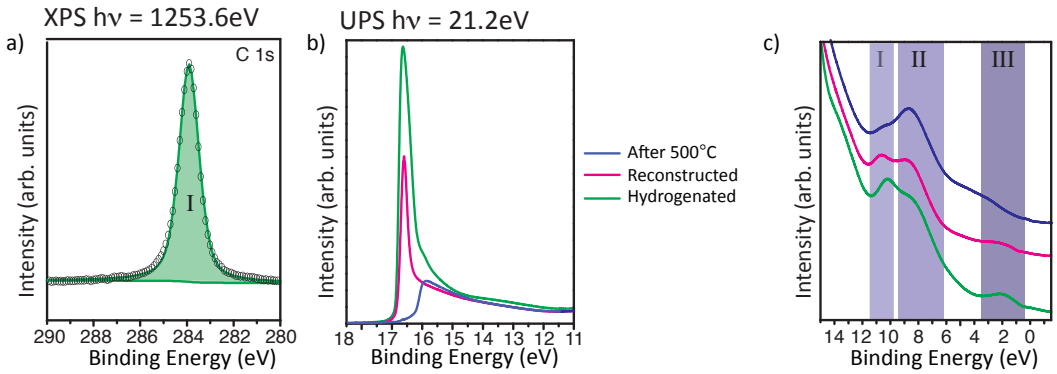

Figure 5.14 XPS and UPS spectra of the surface following the reconstruction and. a) shows high resolution E_{pass}=20eV C1s spectra comprising of a single component b) Shows the increase in secondary electron emission between the surfaces. c) Density of states for both surfaces, see text for details.

Component	Line shape	Position (eV)	FWHM (eV)	At %
(I) sp^3 Carbon	Sum Gaussian-Lorentzian	283.9	1.0	100

Table 5.3 details the components used to fit the high resolution C1s photoelectron peak in figure 5.14a

Figure 5.14b and 5.144c are taken from UPS measurements using the He-I emission line hν=21.2eV. 5.14b shows the relative increase in intensity of the secondary electron tail, whilst 5.14c shows the density of states around the valence band. A bias of -2 V was applied to the sample holder in order to push the electron cut-off towards a higher kinetic

energy range for analysis, and included in the calculation for binding energy that was referenced to the Fermi-edge of the Mo faceplate before H-termination (after 980°C).

5.3.2 Discussion of the hydrogenation results

Removal of the 2×1 surface reconstruction via termination of the surface dangling bonds with atomic hydrogen has resulted in returning the (111) diamond's surface to the desired 1×1 structure. This was made evident by the lack of second order spots in the electron diffraction image (see figure 5.13b). The diffraction pattern shows very small and bright spots relative to the background intensity also indicating the surfaces cleanliness, as surface adatoms generally cause an increase in the background intensity due to scattering processes. The energy of 64 eV was again chosen to show all diffraction spots at a comparable intensity.

The C1s shown in figure 5.14a further indicates that hydrogen adsorption has succeeded in removing the sp^2 surface termination, as it is now comprised of a singular component. The decrease in its FWHM from 1.3 eV to 1.0 eV has not emerged as a result of the hydrogenation process, rather that the diamond was polished in-between the initial laboratory work and the measurements taken for this section. The narrow line width is another key indicator of the pristine surface quality. UPS measurements detailing the evolution of secondary electron tail during these surface-processing steps can be seen in figure 5.14b, and for the valence band at low angular dispersion around normal emission 5.14c. Features located within bands I and II are related to diamond bulk σ-states [93], with the intensity variation of the second component related to removal of oxygen 2s

state ~6 eV. The shape and size of the secondary electron tail changes dramatically between the 500 °C prepared surface and that following reconstruction, this change in shape is related to surface charging which is eliminated as the oxide layer is removed. An increase in the size of the secondary tail between the two states is also seen. This is most likely caused by the new metallic states from the reconstructed surface, which allow additional loss processes. Evidence of the surface states is visible here as the emergent peak around 2 eV which extends to $E_{F.}$ Its persistence following hydrogen termination indicates that graphene regions are still present, as the formation of the 1×1:H surface should of removed all surface states [103]. Electron diffraction shows no change with respect to the graphene residing on the surface, and is not surprising as the lattice match to the diamond is excellent, a variation of the IV from that of the surface after 500 °C would give more indication, as the graphene has fundamentally different characteristics as a result of the lack of a buckled hexagon structure. The increase in the secondary electron tail results from the increase of low kinetic energy electrons allowed to leave the surface. These electrons would otherwise populate energy levels below the conduction band minimum, however they can now escape the vacuum level as a result of the induced negative electron affinity [106]

5.4 Chapter conclusion

Details of the surface preparation steps used before continuing with iron deposition have been discussed in this chapter. The diamond surface is found to be terminated by a monolayer of oxygen following a routine 500 °C heat cycle which following removal at high temperature allows the surface to re-construct into a 2×1 structure. As the 1×1

surface posses three fold symmetry, the 2×1 reconstruction obtain three rotational domains rotated in plane by 60°. Unlike the experimental results that appear in the literature, this particular diamond displays metallic surface state that intersect the Fermi-level when reconstructed, indicating no dimerization between the reconstructed chains occurred. The splitting of the bands near $\bar{\Gamma}$ indicates that the chains formed on this diamond shorter (in the direction of the chain) than those presented in literature, the proximity of the polished surface to the real (111) plane was given as one possible explanation.

Evidence of graphene detaching from the reconstructed surface at elevated temperatures was found via high resolution ARPES and came in the form of a second surface state approaching the Fermi-level between the J and K-point of the reconstructed surface along $[10\bar{1}]$. A second ARPES series confirming this via analyses of a K-M-K slice taken through graphene's Brillouin zone. The graphene's electronic structure appears to be un-affected by the underlying diamond substrate. This evidence points toward the possible production of graphene directly on top of an epitaxially ideal and insulating substrate, an avenue that requires further investigation.

De-reconstruction of the surface from the 2×1 to the 1×1 structure via termination with atomic hydrogen was investigated. Whilst providing an overall removal of surface sp^2 carbon was observed (undetectable within the C1s when measured with lab based XPS), UPS measurements show that graphene produced in this manner appears to be stable during the hydrogen termination procedure as evidence of its surface states are still visible in the valence band following hydrogen plasma treatment.

Chapter 6 – Thin film Iron on Diamond

The role of iron in the following experiments is to provide the catalytic conversion of sp^3-carbon of the diamond surface to sp^2-carbon on the metal surface. It is therefore important to perform a thorough investigation of the growth of Fe on $C_{(111)\ diamond}$ as the growth parameters of this interface can have a large effect on how the graphene will grow. Here studies of the epitaxial growth and phase transition of Fe from fcc (111) to bcc (110) have been investigated with real-time photoelectron spectroscopy and the many operation modes of the SPELEEM.

6.1 Deposition

The deposition of Fe on the (111) surface was followed using real-time photoelectron spectroscopy in order to ascertain how such a metal grows on the substrate. The importance of film uniformity is assumed vital (given the body of evidence for other systems see chapter 3.2.2.2), as clustering of the Fe-film on the diamond surface would provide non-uniform graphene growth. Here results are presented for the real-time deposition of Fe on (111) diamond, and subsequent studies of the how temperature affects the structure investigated with LEED, XPS and LEEM/XPEEM at the SPELEEM of i311 MAXlab.

6.1.1 Results

Figure 6.1a shows a plot of the natural logarithm of the fractional attenuation of the C 1s of diamond during growth of a thick Fe overlayer, and figure 6.1b snapshots (1s integration time) of the C1s for t=0s and t=4000s. Due to similar position of the C1s peak for graphene and diamond, analysis of this system would be difficult when using MgKα X-rays, for the purposes of the REES graphitisation (which will follow in chapter 7). For this reason a thick film of Fe (large compared to the mean-free path of the C1s core level) was required in order to supress emission originating from diamond C1s core level. Table 6.1 details the components used to fit the first C1s photoelectron peak spectrum, which was then propagated through the real-time data series. A linear fit of the dataset reveals a Fe film growth rate of ~0.1 nm min^{-1} when calculated with equation 6.1.1.

$$\text{Rate} = \text{slope of attenuation} \times \lambda \qquad \textit{(Eqn – 6.1.1)}$$

Where λ is the electron attenuation length of the kinetic energy of the substrate core level through an overlayer of known material (here calculated by the NIST EAL database[31]. In this case λ=1.22 nm and the attenuation was 0.0015 s^{-1}.

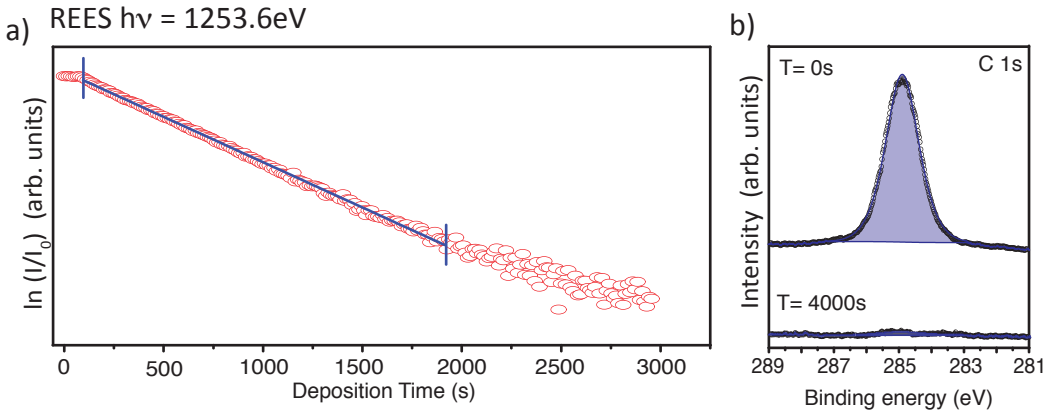

Figure 6.1 Real-time monitoring of C1s attenuation during Fe growth a) exponential attenuation (linear due to the semilogarithmic plot) of the C1s core level indicates a layer-by-layer growth of the overlayer. b) C1s at beginning and end of deposition run

Component	Line shape	E_{Pass} (eV)	FWHM (eV)	At %
C1s	Sum Gaussian-Lorentzian	100	1.76	100

Table 6.1 details the component and parameters used to fit the real-time attenuation of the C1s photoelectron peak in figure 6.1

Figure 6.2 shows the resulting XPS survey scan (6.2a) and high-resolution XPS measurement of the Fe2p core level (6.2b) following a 2 hour deposition of Fe (the first 50min of deposition presented as the REES series of 6.1a) giving a total film thickness of ~12 nm. Table 6.2 details the line profile used to fit the Fe2p core level and the fit parameters.

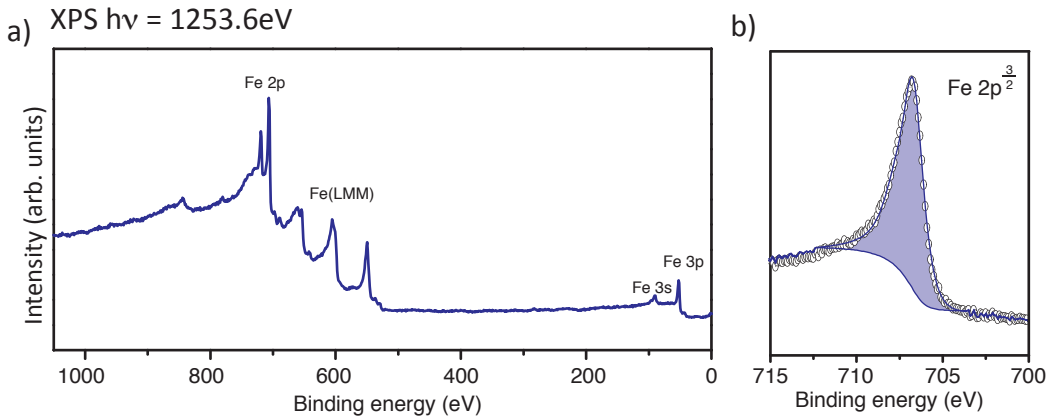

Figure 6.2 a) Survey scan of bulk Fe >10 nm on $C_{diamond}$ (111) indicating the purity of the deposition method as no evidence of oxygen or other foreign species is seen. b) $Fe2p_{3/2}$ component fitted with a single asymmetric Doniach-Sunjic line-shape

Component	Line shape	E_{Pass} ( )	FWHM (eV)	At %
$Fe2p_{3/2}$	Doniach-Sunjic	100	1.41	100

Table 6.2 details the component and parameters used to fit the High resolution Fe2p photoelectron peak in figure 6.2

A thin film of Fe was deposited in order to investigate the interface between Fe and Diamond. Quantification of the spectra presented in figure 6.3a reveals a Fe overlayer thickness of ~1.6 nm. Figure 6.3b shows a high resolution C1s core level, E_{pass}=20 eV, taken 30° from normal emission in order to improve the surface sensitivity of the technique (XPS surface sensitivity ~$3\lambda\cos\theta$ [34]). The peak shows a second component located ~1.6 eV lower in binding energy than the main sp^3 component. Details of the fit are shown in table 6.3

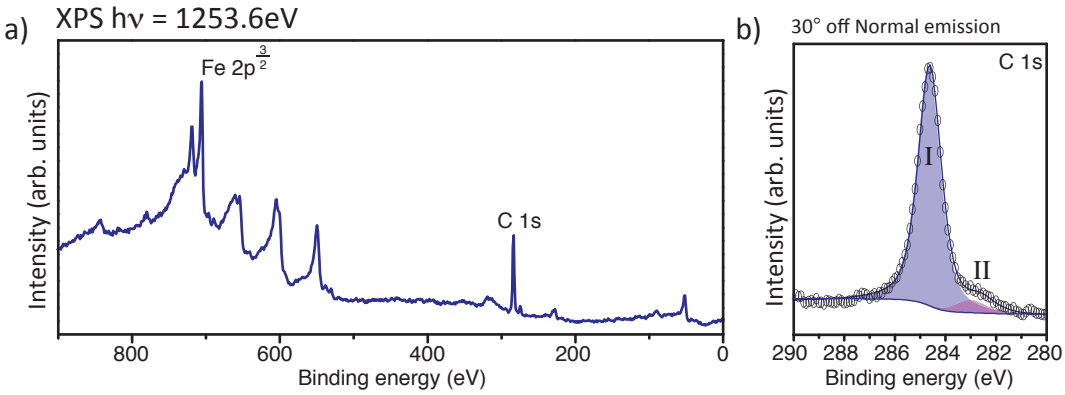

Figure 6.3 a) survey scan following thin film growth of Fe on $C_{diamond}$ (111) . Quantification of the components reveals a 1.6 nm thick film. b) C1s taken 30° off normal (towards illumination source) in order to achieve a more surface sensitive measurement. The peak contains a second component located 1.6eV to lower binding energy

Component	Line shape	Position (eV)	FWHM (eV)	At %
(I) sp^3 Carbon	Sum Gaussian-Lorentzian	284.6	1.10	94
(II) Carbide	Sum Gaussian-Lorentzian	283.0	1.40	6

Table 6.3 details the components and parameters used to fit and the C 1s photoelectron peak shown in 6.3b

The images shown in figure 6.4 show the as deposited results for a 2 nm Fe film on diamond (111). As quantification of XPS spectra in the SPELEEM is unreliable following transfer to and from the preparation chamber another approach to estimate film thickness was sought. Here the E-beam evaporator was inserted into the microscope chamber and reflectivity oscillations counted during deposition to determine the number of layers formed. As the doser is equipped with its own flux monitor (in arbitrary units of nA) the growth rate can be calibrated to a constant deposition flux, for which 10 nA for 2 hours is estimated at 6 monolayers ≈2 nm.

Mirror electron microscopy and XPEEM images of the surface show that the deposited thin film is homogeneous across the surface. A diffuse 1x1 LEED pattern is shown in 6.4b,

this indicates that the Fe overlayer grows commensurate to the fcc(111) diamond substrate.

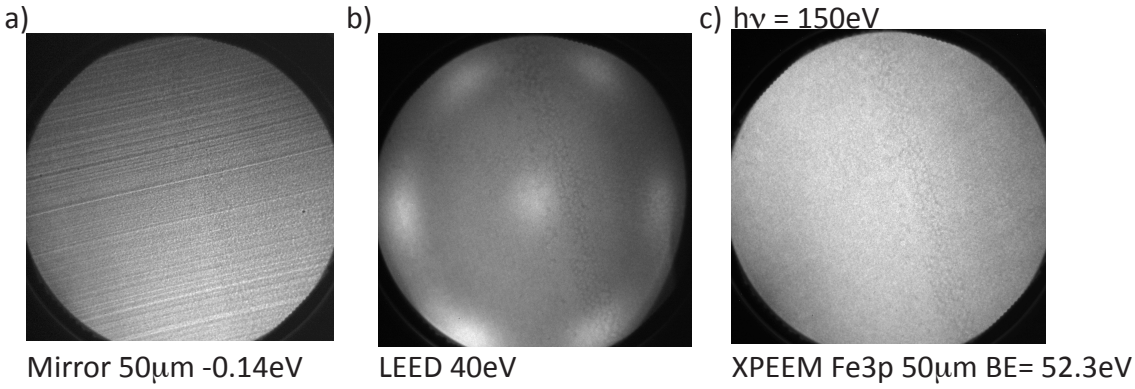

Figure 6.4 Images of the surface following 2 nm Fe film deposition from an e-beam evaporator at a sample temperature of 40°C. a) Mirror mode microscopy indicating no large change in topography following deposition. b) LEED image shows fcc (111) Fe lattice as deposited. c) XPEEM image of Fe3p core level ($E_{binding}$=52 eV) indicates homogeneous coverage across the surface

6.1.2 Discussion

The growth of Iron on (111) diamond has been investigated; the results show that the growth mode follows a Frank-van der Merwe (layer-by layer) relationship as indicated by the linear attenuation of the C1s core level during REES measurements. A carbide component that forms at the diamond/Fe interface is apparent within the C1s when the surface sensitivity of the measurement technique is improved by collecting the core level at low collection angles. The component lying ~1.6 eV to lower binding energy is also in good agreement (±0.2 eV) carbide component formed by graphene on Fe(110)[217]. This carbide formation is expected to restrict clustering during the annealing process allowing the possibility of patterning the catalyst on the surface for subsequent graphene growth. Evidence of a pseudomorphic growth of fcc-Fe up to at least 2 nm (~6 ML) when deposited at room temperature is seen in the LEED pattern of figure 6.4b. The lattice

match of fcc-Fe (3.59 Å) and fcc Diamond (3.57 Å) is extremely close however the broad spots indicate that some disorder, or bcc regions exist.

6.2 Iron structural transition

During the initial stages of annealing, evidence of the Fe-layer undergoing a phase transition is apparent, the results are presented here.

6.2.1 Results

Figure 5.6 and 5.7 shows the sample surface following annealing to 320 °C and 440 °C respectively. The mirror electron images indicates that no clustering of the Fe film occurs following to 440 °C, however an obvious restructuring of the film is apparent in the LEED images. Dispersive plane imaging indicates that no carbon is present at the surface as evident by the photoelectron peaks shown in figure C of both figures.

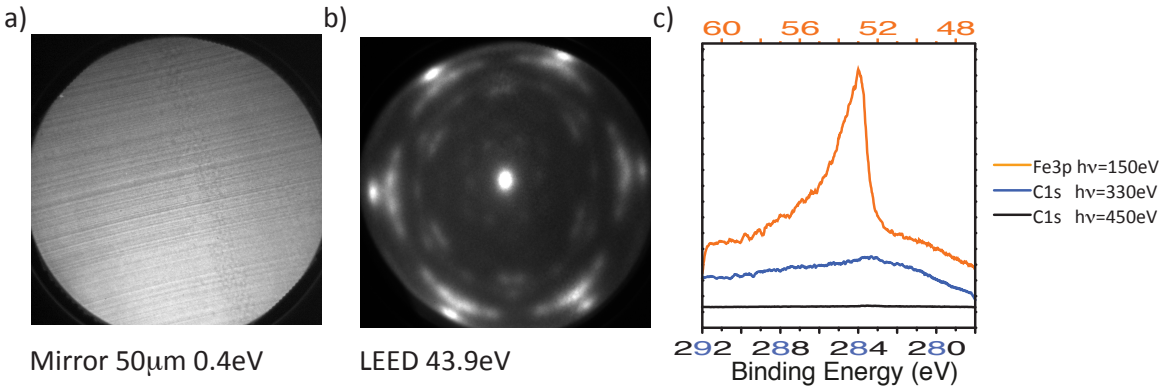

Figure 6.5 Shows the surface after annealing to 320°C a) Mirror mode microscopy still indicates uniform surface coverage during the annealing stage. b) Electron diffraction pattern shows evidence of fcc-bcc reconstruction of the Iron layer. c) Dispersion plane spectra indicating the film is still comprised primarily of Fe

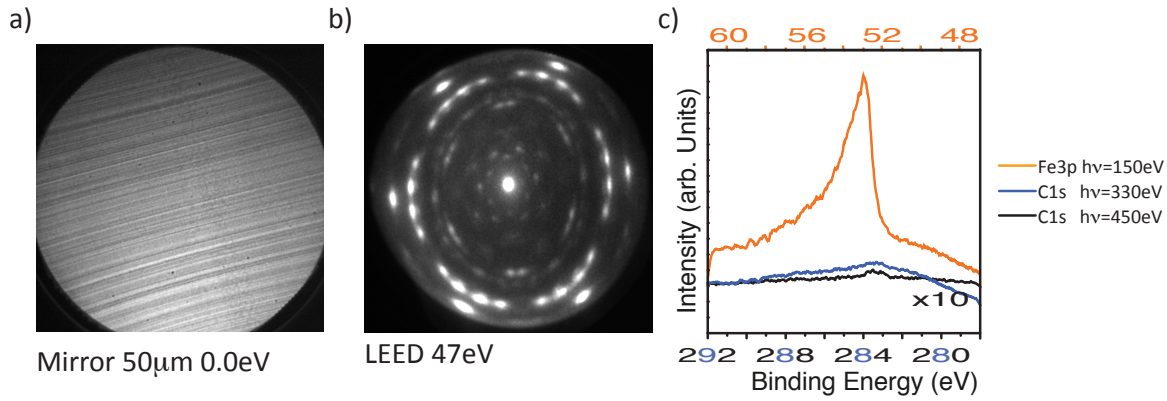

Figure 6.6 shows the metal film following anneal to 440°C a) Mirror microscopy indicates some roughening of the film, along the polishing directions of the underlying diamond. b) Electron diffraction shows the Fe overlayer is becoming more crystalline due to more resolved diffraction beams. c) Dispersive plane spectra show that the film Is still primarily composed of Fe, however a small feature of the C1s at hν=450 eV for this film reveals that there may well be some dilute carbon within the metal film

6.2.2 Discussion

The LEED patterns presented above are a representative selection (as many LEED patterns were taken from different regions) of the data, recorded at room temperature following annealing cycles of the sample in steps of 20 °C from 340 °C to 500 °C. The two images were chosen as they represent the initial and final stages of the structural transformation, where only the intensity and size (spots become more defined) of the diffraction spots improved for every increase in temperature up to 440 °C. Although the diffraction pattern is complex, some similarities and conclusions can be drawn from similar studies of iron grown on hexagonal substrates. For instance thin Fe films grown on Au(111) show a phase transition from fcc(111) for the first monolayer to bcc(110) at around 2.5 monolayers when studied with STM [262]. Similar results for the growth of Fe on Cu(111) have been observed, where Fe films deposited at 300K show fcc(111) dominating the growth mode, however the overlayer does not grow in a layer by layer fashion on this substrate[114]. Deposition of Fe on Ni(111) substrates has also been

studied[263], this represents another system in which there is an excellent lattice match to the substrate for fcc-Fe (Ni a_0=3.61 Å)

The effect of constraining rectangular bcc(110) lattices to hexagonal fcc(111) substrates will inevitably result in rotational domains due to equivalent lattice sites around the hexagonal lattice where all are expected to be observed. Two models of the resulting structures are the Kurdjumov-Sachs (KS) in which six rotational domains are found, and Nishiyama-Wasserman (NW) where three rotational domains are found. The number of rotational domains observed is related to the dimensional matching of the overlayer to the substrate, where a match in a single dimension results in six possible rotational domains, and a match in two-dimensions yields only three. The real space lattice match of bcc-Fe(110) and fcc-$C_{diamond}$(111) is shown in figure 6.7 using the lattice parameters of a_0=2.861 Å for bcc-Fe [264] and a_0=3.567 Å [89]. For the purposes of differentiation between the substrate direction and the overlayer direction triangular and square brackets are used respectively.

The 1D matching is shown in figure 6.7a, the lattice match lies along the diagonal of the rectangular bcc lattice along $[\bar{1}1\bar{1}]_{bcc}$ which lies parallel to the $\langle 011\rangle_{fcc}$ direction. The angle between $[\bar{1}10]_{bcc}$ and $\langle\bar{2}11\rangle_{fcc}$ is 5.25°. The case of 2D matching is shown in figure 6.7b the $[\bar{1}10]_{bcc}$ lies parallel to the $\langle\bar{2}11\rangle_{fcc}$, and the $[01\bar{1}]_{bcc}$ lies parallel to the $\langle 011\rangle_{fcc}$ direction.

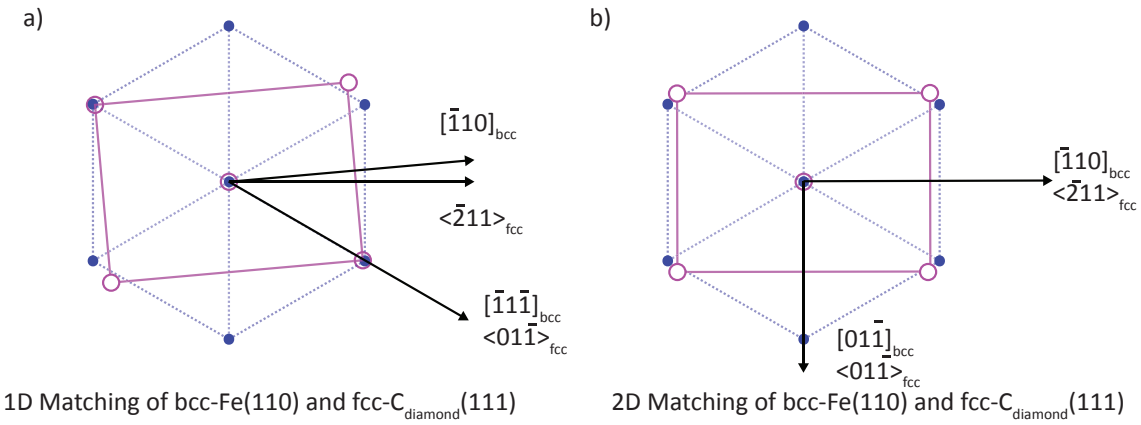

Figure 6.7 Shows illustrations of the possible matching between bcc Fe on fcc diamond lattices. a) shows one of the possible six matching directions of the Kurdjumov-Sachs orientation, whilst b) shows one of the possible matching directions of the Nishiyama-Wassermann orientation.

Models of the reciprocal space patterns for all of the rotational domains of KS and NW and are shown in Figure 6.9 a and b respectively. The zero order (0,0) diffraction spot is observed for all lattice rotations and in the case of the illustrations presented here the (0,0) is larger to represent an accumulation of all rotations. However first it is important to understand the reciprocal space pattern of a single bcc lattice and how it compares to that of fcc lattices, figure 6.8 shows the two side by side

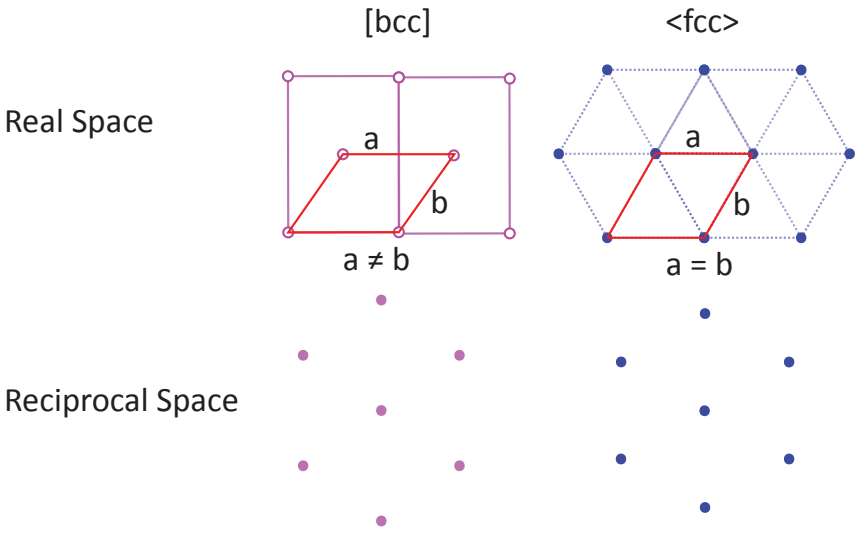

Figure 6.8 Shows a schematic representation of the real space unit cells of bcc and fcc lattices and the resulting reciprocal space patterns.

The surface unit cell for fcc lattices on the (110) plane is a rhombus in which a is equal to b which generates a perfect hexagon in reciprocal space rotated by 90°, however for the bcc lattice the unit cell is a rhomboid with sides of unequal length where $b = \frac{a\sqrt{3}}{2}$. The resulting reciprocal space pattern although still rectangular is seen to be a hexagon stretched in one dimension, which when rotated yields the patterns shown in Figure 6.9.

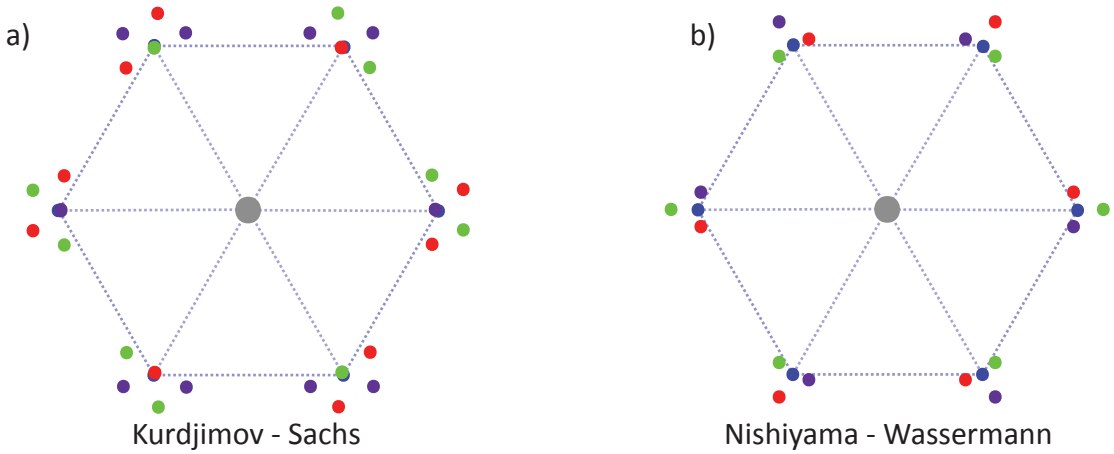

Figure 6.9 Shows the resulting reciprocal space patterns for a) KS and b) NW when all rotational domains are considered. The substrate lattice is shown in blue whilst the rotational domains are represented by green, purple and red spots.

Clearly the resulting reciprocal space pattern are not sufficient in describing the diffraction patterns observed in Figures 6.5b and 6.6b although similarities between the triangular formations around the $1\times1_{fcc}$ lattice of the NW reconstruction can be seen, indicating that there are most likely only three rotational domains. The XPS spectra presented in the corresponding figures suggest that the possibility of a carbon-stabilised reconstruction of the surface is unlikely as no carbon signal was observed even when the surface sensitivity was decreased by going to higher photon energies. However this is not ruled out as only few percent of carbon (below the detection limit of the instrument) is required to cause stable reconstructions on Mo[265]. The possibility of the diffraction

pattern resulting from Fe_3C (cementite) formation can be dismissed as the structure presented here does not correspond to the observed diffraction patterns in literature for such a material (see figure 1 c) and d) in *Ref.*[217]).

The remaining explanations of the diffraction patterns observed here is that they result from a clean-surface reconstruction, or result from a superstructure of rectangular bcc-Fe on the fcc-diamond surface, which results from long-range lattice matching of the two lattices.

6.3 Chapter conclusion

This chapter has presented details on the growth and re-structuring of ultra-thin iron films on (111) diamond single crystals. The growth mode follows a Frank-van der Merwe (layer-by-layer) mode that appears pseudomorphic at thickness well above that observed for iron deposition on other substrates. At temperatures above 300°C a phase transition (no longer pseudomorphic from hexagonal fcc to a rectangular bcc lattice is apparent for the film. It has been shown that models of the reciprocal space patterns for 1×1 rectangular lattices on top of 1×1 hexagonal ones do not adequately describe the observed structures here. Instead the complex LEED pattern is thought to be due to a long range lattice match between the overlayer and substrate however further investigation is necessary to completely understand such structures.

Chapter 7 – Catalytic graphitisation

Presented in this chapter are the results of three experiments that follow the catalytic graphitisation of the diamond substrate in the presence of thin Fe films. Here the presence of the hot transition metal catalytically breaks the sp^3-bonds of the substrate, and subsequently transports the now free carbon atoms to the surface where they can recrystallise to form sp^2-bonded graphene. The real-time spectroscopy work has been published in a recent article (see *Ref.*[14]) which includes a similar method of production on 6H-SiC (0001) surfaces. The details from this substrate have been omitted from this section however as the previous two chapters have only dealt with the (111) diamond substrate.

7.1 The initial stages of graphene growth

7.1.1 Results

Figure 7.1a shows the real-time electron spectroscopy (REES) measurements performed during a linear annealing cycle up to ~785°C at a rate of 0.45 °C/s and during cooling for a ~12 nm thick Fe film deposited on the diamond(111) surface. The experiment was performed directly after the deposition presented in chapter six figures 6.1 – 6.2. Snapshots of both C1s and Fe2$p_{3/2}$ photoelectron peaks were captured sequentially every two seconds at E_{pass}=100 eV and fitted with the parameters shown in table 6.1 and 6.2 respectively. Figure 7.1b shows the C1s photoelectron peak taken at room temperature following the heat-cycle shown in figure 7.1a. Details of the components used to fit the C1s peak are presented in table 7.1.

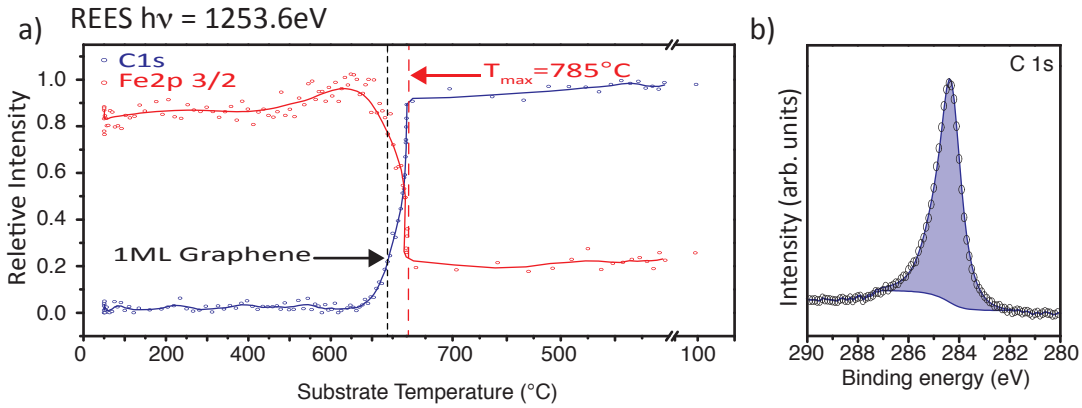

Figure 7.1 shows a) REES data taken during annealing and cooling of a thick ~12 nm Fe film on Diamond (111). One monolayer graphene is indicated on the graph and calculated from intensity ratio of Fe2p and C1s photoelectron peaks. b) High resolution C1s Epass=20 eV following cooling shows asymmetric line profile expected from metallic materials.

Component	Line shape	E_{Pass} (eV)	FWHM (eV)	At %
C1s	Sunjic-Doniach	100	1.0	100

Table 7.1 Details the line-shape and parameters used to fir the C1s peak shown in figure 7.1b

Figure 7.2 shows the initial stages of growth as made evident by the emergence of a C1s component on the surface (7.2c) and reduction of the Fe3p photoelectron peak at T= 495 °C. The surface appears to roughen during the initial stages as carbon emerges to the surface. The intensity of the LEED spots towards the centre of the pattern has changed dramatically from that presented in 6.6b where the brightest features now correspond to the 1×1 pattern of hexagonal graphene.

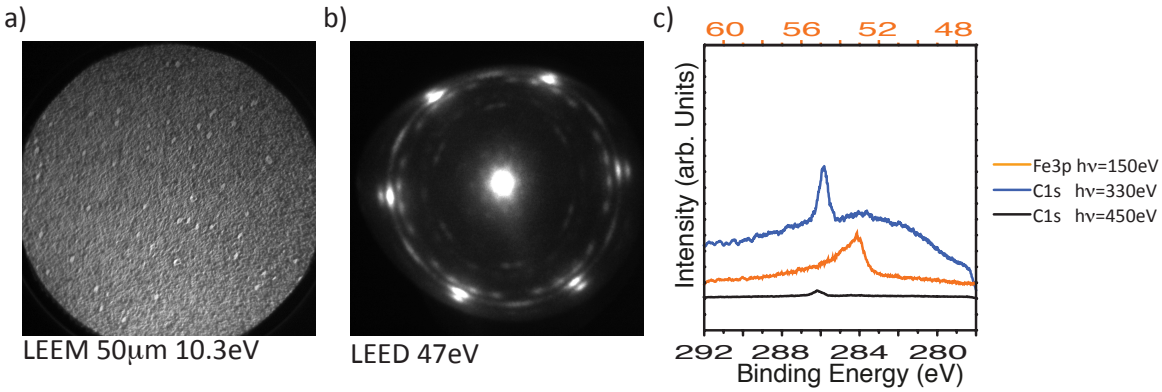

Figure 7.2 The surface following an anneal of the sample to 495 °C a) Mirror microscopy indicates some roughening of the surface following heat treatment .b) μLEED pattern from the surface at 47 eV c) Dispersive plane spectra indicating Carbon at the surface due to Fe3p and C1s ratio

Following observation of this 'rough' surface an investigation of whether this surface could be smoothed by annealing the sample at ~500 °C was undertaken, in order to improve the quality of the formed graphene layer. Figure 7.3 shows three images of the surface during annealing at constant temperature for a) 0 minutes, b) 15 minutes and c) 1.5 hours.

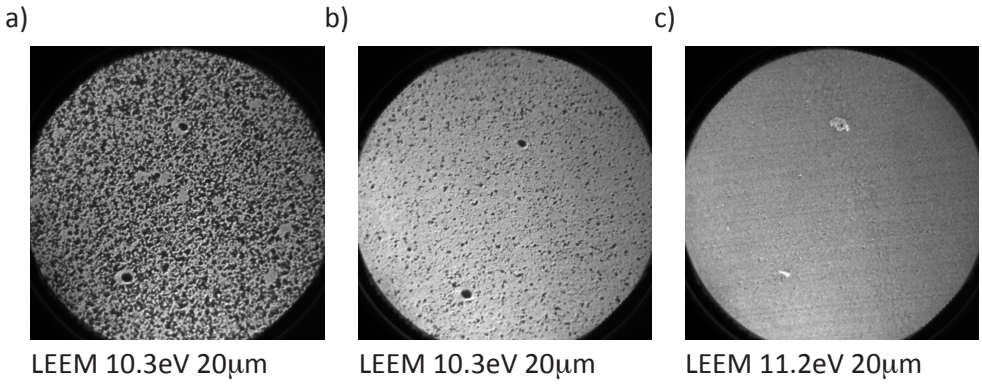

Figure 7.3 Time series of the surface smoothing when held at a constant temperature of 500 °C for a) 0 min b) 15min and c) 1.5hours

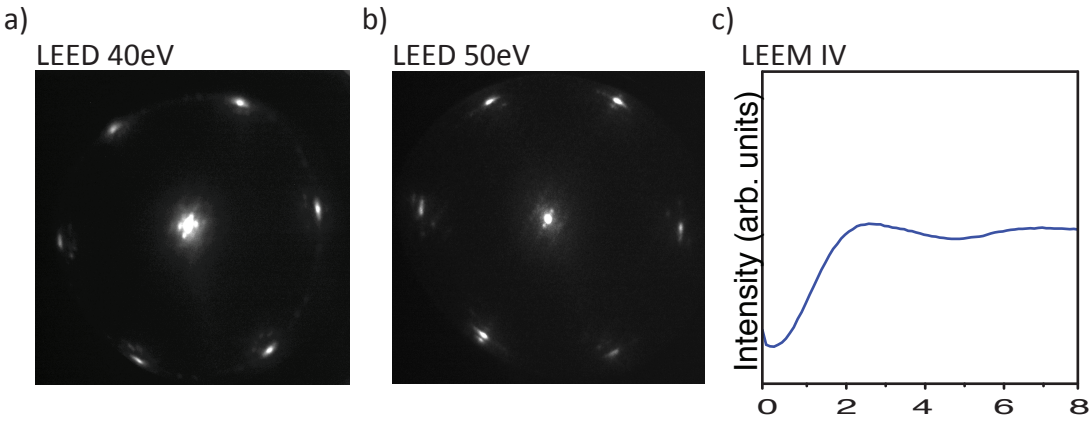

Figure 7.4 Electron Diffraction patterns and LEEM IV oscillation of the surface seen in Figure 7.3c. a) The dominant pattern observed across the surface at 40 eV. b) A single rotational domain of bcc-Fe under graphene taken at 50 eV shows a Morié pattern in one direction. c) LEEM IV measurement reveals characteristic oscillation of closely bound graphene buffer-layer

The resulting electron diffraction patterns from this smooth surface shown in figure 7.3c are shown in figure 7.4. The 1×1 pattern of graphene is now obvious however other hexagonal features are evident around the 1×1 and zero-order spots and are likely due to the superstructure of graphene on bcc-Fe. The rotation observed between the 1×1 diffraction spots results from mounting the sample in a slightly different orientation from that in a) and has been selected as it shows predominantly a single direction of the underlying bcc-Fe lattice as visible by the Moiré pattern in a single direction. Figure 7.4c shows the LEEM IV oscillation, in which the attenuation of the electrons occurs for

energies less that 2 eV, and is characteristic of a buffer-layer similar to that seen for the $6\sqrt{3}\times6\sqrt{3}$ reconstruction of SiC surfaces[69].

A similar experiment was performed at the SGM3 beamline of ASTRID, here 2 nm of Fe was deposited and the sample annealed for 40 minutes at ~500 °C. The film thickness was estimated by previous calibration of the evaporation source involving quantification of the attenuation of Cu3p core level following a thin Fe overlayer (~1.2ML). A comparative study on the diamond could not be performed, as the photon energy required to excite the C1s peak could not be reached on this beamline.

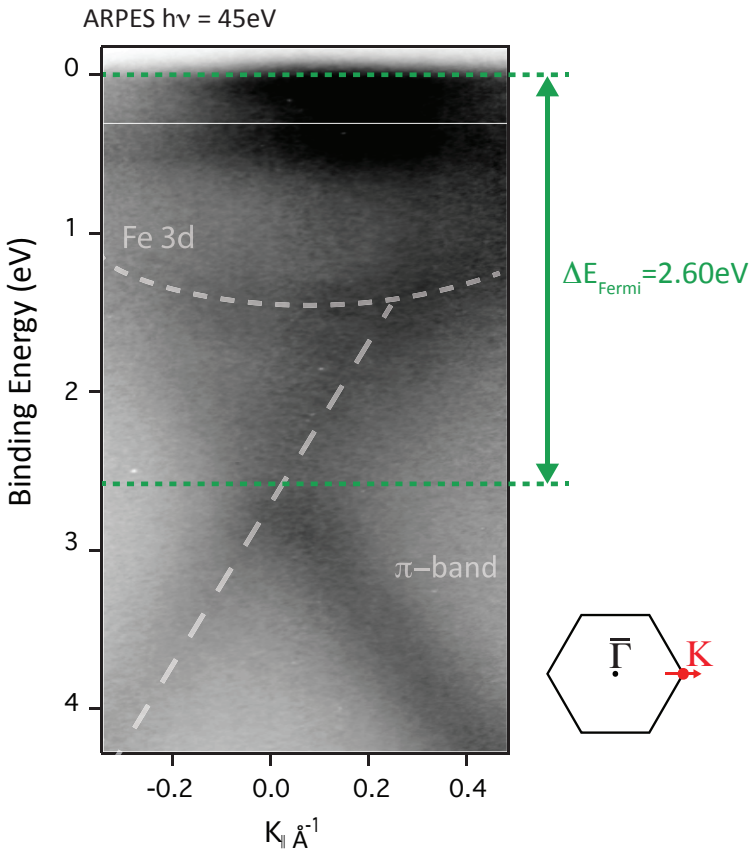

Figure 7.5 ARPES data taken following 4min anneal of 2 nm Fe-$C_{diamond(111)}$ interface at 625 °C. The data is believed to represent the current state of the surface (LEEM image 7.3c). The K-point is observed to be n-doped by ~2.6 eV indicating a strong interaction of the graphene with the underlying substrate. The intense features at the Fermi-level are due to the Fe d-states.

Figure 7.5 show an ARPES cut taken through one of the K-points of graphene towards the next Brillouin zone centre. The K-point appears to be shifted in energy towards higher binding energy ~2.6 eV indicating a strong interaction between this layer and the underlying Fe. The location and energy of the K-point and Fe3d band observed matches well with the ARPES data shown in the work of Varykhalov [266], in which the recipe for graphene production on Fe(110) of Vinogradov and Preobrajenski [217] was used.

7.2 The growth of quasi-free-standing graphene

7.2.1 Results

Following the growth of the buffer layer a small increase in temperature of ~30°C is all that's necessary to enabled carbon to be emitted from the buffer layer and grow across its surface. Figure 7.6 details the results following 1 hour at 530°C. The colour circles shown in figure 7.7a correspond to the LEEM IV curves and diffraction patterns seen in b) to d). Figure 7.6f shows a 20µm XPEEM image of the Fe3p photoelectrons from another region on the sample. No evidence of Fe residing in the formed graphene layers is seen.

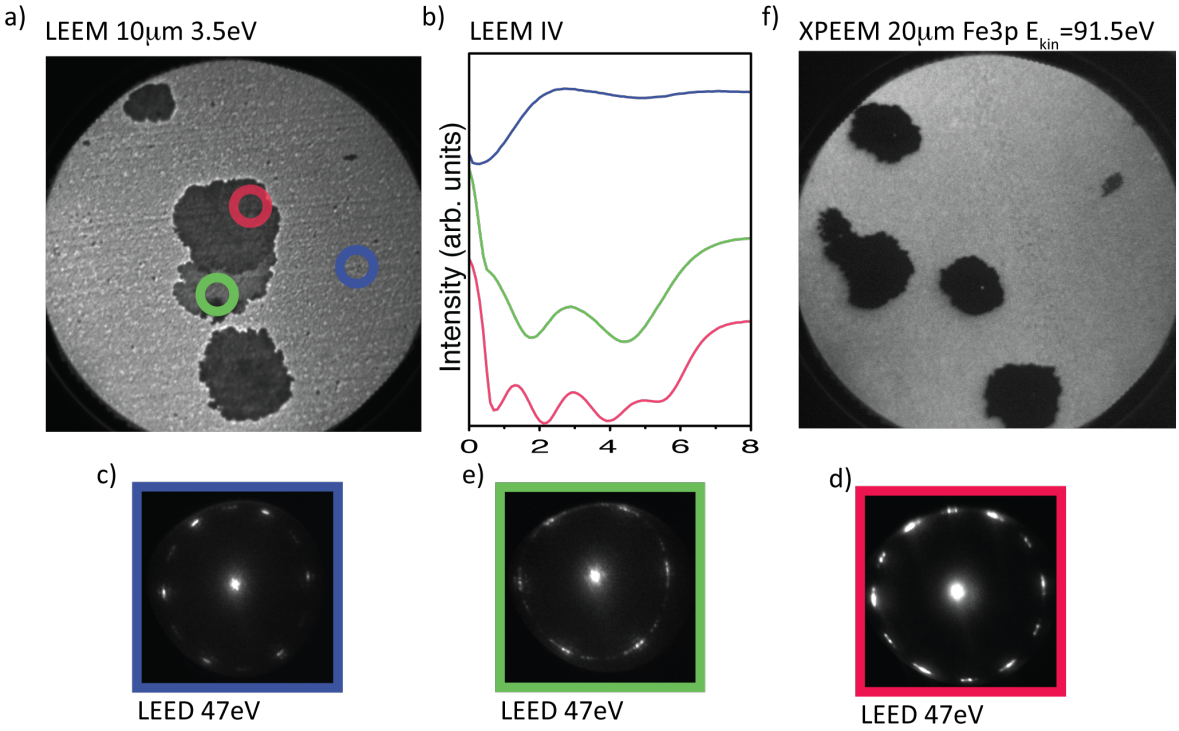

Figure 7.6 Surface annealed to 530°C for 1 hour. a) LEEM image chosen for graphene contrast, colour circles used to represent data in the following images. b) LEEM IV oscillations for buffer layer (blue), bilayer- (green) and 4-layer graphene islands. c) Electron diffraction shows that no change in structure has occurred for the buffer layer. d) and e) show how graphene grown slowly like this is prone to lattice rotations.

A further increase in temperature of 30°C allows larger areas of the buffer layer to be promoted to quasi-free-standing graphene layers. Figure 7.7 shows the various experimental results collected after cooling the sample to room temperature following a 1 hour anneal at ~560°C. As with the previous figure, the colour circles of figure 7.7a correspond to the colour of the data presented in b) to e).

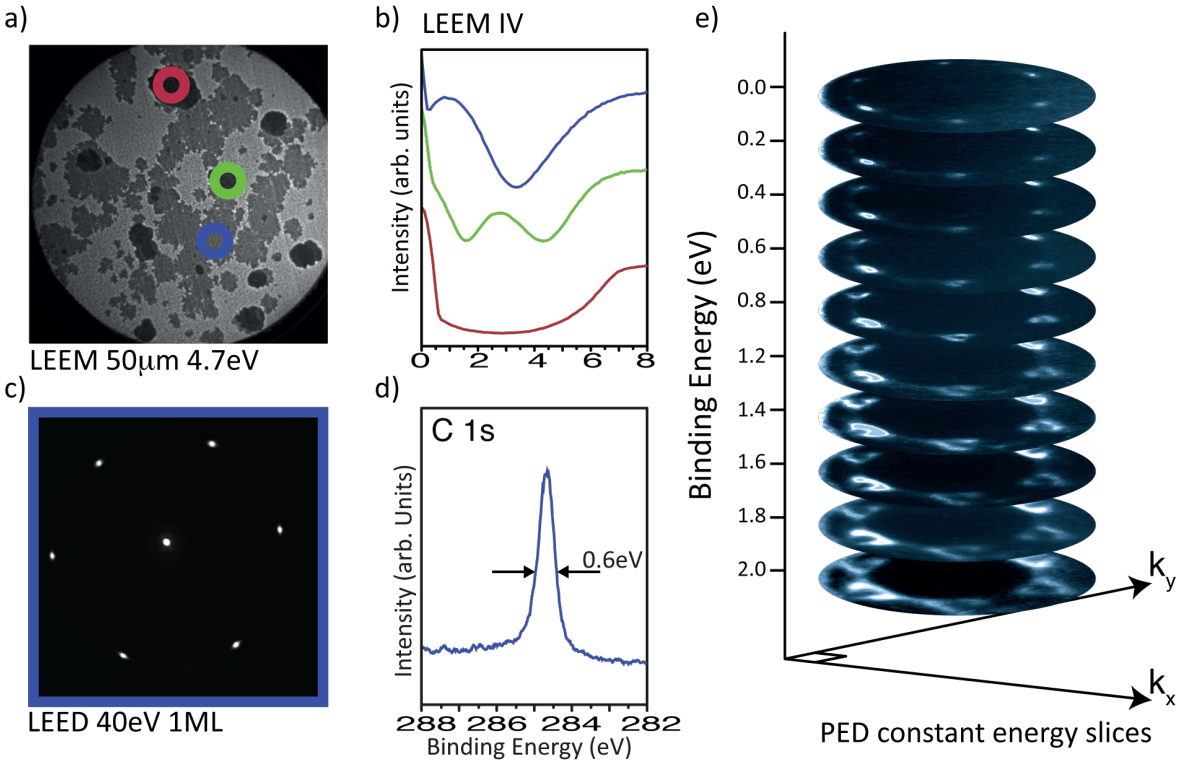

Figure 7.7 The surface following 1hour anneal at 560°C. a) LEEM image chosen for graphene contrast, colour circles used to represent data in the following images. b) LEEM-IV oscillations for the regions illustrated in 'a' showing mono-(blue), bi-(green) and many- (red) layer graphene islands. c) Electron diffraction pattern from monolayer area, the intensity of the outer six spots of the hexagon have all been increased equally in contrast, as they were observed to be weak in intensity due to the high brilliance of the zero order diffraction spot. D) Dispersive plane spectra of the 1ML area. f) Stacked constant energy slices showing the six conical bands of graphene's π-states.

With respect to the LEED pattern presented for the 1ML area (figure 7.7c) the contrast of an area surrounding each of the six outermost spots (area was at least 10 times that of the diffraction spot) has been linearly increased irrespective of the zero order spot, this has been done for two purposes. Firstly the zero order spot was so sharp and bright that the outer spots appeared very dim in comparison (a problem that would not occur in conventional rear-view LEED as the zero, order spot would be hidden by the electron gun and integration of the outer spots could be performed without the danger of saturating the CCD of the acquisition camera). Secondly, it was necessary to investigate whether the outer spots had any evidence of the Moiré pattern seen for the buffer layer (figure 7.6a-b)

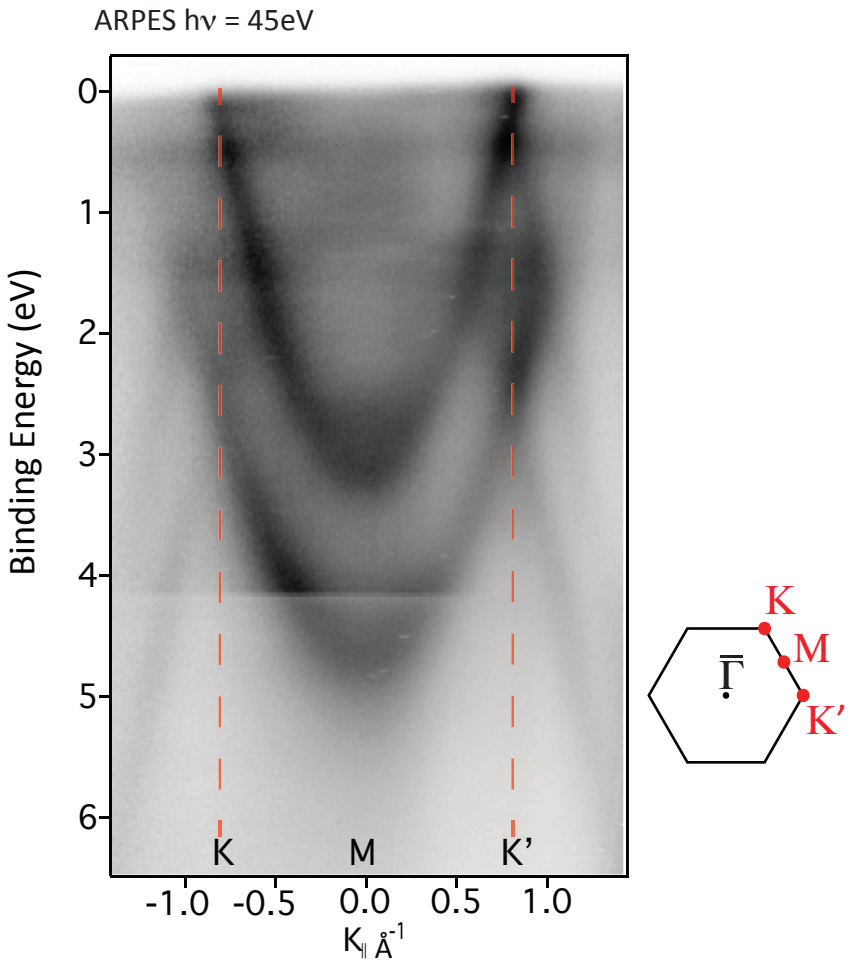

Figure 7.8 ARPES series taken following a total anneal time of 20 minutes at 625 °C. Slice taken along K-M-K' direction showing two Dirac points and the saddle of both the buffer layer and 1st layer graphene. 1st layer graphene is observed to cross the Fermi-level at the K-points.

Figure 7.8 represents the data that follows on from the experiment detailed for figure 7.5 after annealing the sample for 20 minutes at ~560 °C. The sample was tilted (as described for the data collection of figure 5.12b) in order to collect a slice that included two K-points (K and K') and the saddle of the π-band at M (See schematic to the right of the dataset).

7.3 Discussion

The growth of graphene has been monitored of for the Fe on $C_{diamond}$ system using real-time photoelectron spectroscopy. This allows the C1s and Fe2p core levels to be monitored continuously during a programmed temperature ramp to ~800 °C and during cooling. The results are shown in the peak intensity plot of figure 7.1a. During the initial stages of annealing a change in the Fe2p core level intensity is apparent. This is most likely due to re-ordering of the Fe film, which is known to undergo a phase transition from a (111) fcc-lattice to a (110) bcc-lattice as described in chapter six. The temperature at which this phase transition occurs i.e. the temperature at which the intensity of the $Fe2p_{3/2}$ core level increases, seen in the REES measurement is above 500 °C whilst for thinner films the phase transition is seen to occur at ~320°C (see figure 6.5b). The difference in temperature is most likely related to the time and temperature required for thicker films to undergo such a transition.

The initial activation temperature, i.e. the temperature at which carbon begins to detach from the diamond surface in the presence of the Fe catalyst, is related here to the onset temperature at which the C1s peak begins to increase in intensity. Here the increase of the C1s is seen to occur at ~620 °C. Other studies of the system in the SPELEEM indicate that for thinner Fe films ~2 nm, carbon begins to form on the surface at ~495 °C as indicated by XPS in panel c) of figure 7.2. The thickness of the Fe film therefore plays a role in determining how long and at what temperature the graphene will emerge on the surface. It is therefore assumed that the transport of carbon atoms to the surface is not a fast process, rather that the hot Fe layer is capable of accepting interstitial carbon atoms

into its lattice, where only the continuation of carbon being accepted from the bottom-up forces carbon to the surface. If this is the case the temperature at which the C1s peak begins to emerge during the REES measurement, is related to the moment at which carbon is visible at the deepest analysis depth (∼3λ) and not the surface. Monitoring the process in real-time does however enable a method for the precise control of the overlayer thickness as continuous evaluation of the core level intensities is possible[14].

Moving away from averaging techniques such as XPS into a real-space regime provided by the many operation modes of the SPELEEM enable investigations of the true growth mode of graphene on the Fe-$C_{diamond}$(111) system. It was found that annealing the Fe-Diamond interface at 500 °C for 1.5 hours is sufficient to create a layer of graphene across the entire surface (see figure 7.3). At this temperature, the growth of graphene appears to be self-terminating at the 1^{st} layer, where only defects in the lattice show a vertical growth of small graphene islands. This self-limiting is possibly related to a thermodynamic equilibrium phase, where lowering of the surface free energy of the metal by formation of the complete first layer, hinders subsequent graphene formation as described for some CVD processes [198, 199].

The diffraction patterns from this surface appear to be in excellent registry to the substrate, with no rotational domains of the 1×1 spots observed. A Moiré pattern due to the underlying bcc-Fe mismatch shown along a single direction in panel b) of figure 7.4 also implies that larger domains of the underlying Fe lattice also form at this higher temperature (for lower temperatures no single domain could be seen in LEED measurements for the bcc-Fe(110) lattice as detailed in chapter 6). The LEEM IV

oscillations taken from this graphene layer in panel c) of figure 7.4, displays a pronounced single dip below 2 eV, characteristic of a buffer layer. This oscillation is however much stronger than that observed for the $6\sqrt{3}\times6\sqrt{3}$ reconstruction of the SiC surface[69] indicating that the buffer layer on the $C_{graphene}$-Fe-$C_{diamond}$ system is more weakly interacting than its counterpart on SiC, and most likely only bound by strong electrostatic forces.

Angle resolved photoemission data taken at around the same stage of buffer-layer growth is presented in figure 7.5. Here the K-point is heavily n-type doped by ~2.6 eV, indicating a strong interaction between the graphene and Fe film. The closest matching material that provides doping of this magnitude is Ruthenium, which also shows an n-type doping of 2.6 eV [198]. As Fe is a much cheaper material in comparison to Ru (which belongs to the Platinum group of elements) it offers a reduction in cost in the manufacture of devices that may require such large n-type doping of the graphene.

The characteristic linear relationship of the π-bands is not altered around the K-point which is unusual given the Moiré pattern observed for the underlying Fe(110) layers, where usually due to the strongest interaction sites of the mismatched lattices a mini-gap opens in the π-bands as seen for graphene on Ir(111) [211]. The fact that the linear dispersion of the π-bands is preserved is a clear indicator of massless Dirac fermions on the $C_{graphene}$-Fe-$C_{diamond}$ system. The result of shifting graphene's band structure by such a large amount is a hybridization of graphene antibonding π^*-bands with the metal substrate 3d-bands, opening a large bandgap in the π^*-band [197]. This has previously been shown in ARPES measurements for Co, Ni and Fe [266, 267]. The data presented in

figure 7.5 cannot reliably see this, however the location of the K-point and of the Fe3d states matches well with that seen in *Ref*.[266, 267] suggesting the same effect here.

Further increasing the temperature of the systems enables carbon to be ejected from the buffer layer as seen in figure 7.6. With the substrate held at a temperature of 530 °C for an hour, graphene islands ranging from ∼1 to 6 μm in size grew. It is apparent that at this temperature the growth is slow, and prone to rotational faults as evident by the LEED patterns of figure 7.6 for bi-layer and 4-layer graphene where the number of graphene layers was determined by the LEEM IV oscillations shown in figure 7.6. These rotational domains indicate that the graphene also consists of smaller domains. The growth appears to seed through defects in the buffer layer and grows vertically in small islands rather than laterally across the surface. The graphene areas formed were too small to reliably collect VPED constant energy slices (as the surrounding buffer layer would also contribute to the spectra) however the LEEM IV oscillations alone are a good indicator that the islands are made of weakly interacting graphene layers[69]. The graphene regions are free from Fe (which could possibly reside between the layers), as made evident by XPEEM imaging of the Fe3p core level (panel f of figure 7.6). The intensity of Fe3p photoelectrons electrons located in the buffer-layer region is due to the core level not being completely attenuated by the above graphene buffer layer.

By further increasing the temperature by 30 °C it was possible to cause larger areas to grow from the buffer layer. At this temperature an increase in the rate of lateral growth of the already formed islands was apparent. Accompanying this was the detachment of larger ∼25 μm regions from the buffer layer. The areas began as small seeds, which with

time grew into each other rather than under/over each other. This indicates that growth of the monolayer regions are in rotational registry with each other and simply merge together to form a quasi-free-standing monolayer graphene, for instance no evidence of grain boundaries between the merged monolayer areas was found. A sharp 1×1 LEED pattern for the monolayer area was seen across these regions which matches the underlying diamond 1×1 diffraction pattern (see Figure 5.13b) indicating that there is registry between the diamond substrate and graphene overlayer through the Fe-film. The intensity and sharpness of the (0,0) spot is another indicator of the quality of the graphene formed. The C1s photoelectron peak shown in figure 7.7d is located ∼284.6 eV and displays a very narrow FWHM of ∼0.6 eV yet more indication of high quality material, since the C1s displays large broadening (up to 1.1 eV) when defects in the material are created[268]

Panel e) of figure 7.7 shows constant energy slices (VPED) of the angular distribution of photoelectrons around the valence band of graphene. Again, due to the acceleration of electrons in the imaging column, the constant energy slice is capable of imaging the entire Brillouin zone. The images were recorded every 0.2 eV from -0.4 to 2 eV binding energy, and taken from the large quasi-free standing regions shown in figure 7.7a. The conical nature of the six Dirac-cones can clearly be seen when these images are stacked as shown. At the Fermi-level it is obvious that some of the Dirac-cones do not come to a point, this is due there still being some energy distribution across the image, an artefact of the hemispherical analyser of the system.

The I(E, K_{II}) slice shown in Figure 7.8 was extracted from an angular series after annealing the sample for 20 minutes at 560 °C before cooling to room temperature. The slice presented here is taken along the K-M-K direction of graphene's Brillouin zone as shown in the schematic to the right of the figure. Two data sets, one at higher binding energy, have been stitched together in order to show the full structure along this direction for both the buffer and quasi-free-standing graphene regions (second data set starts at $E_{binding}$=4.1 eV). The intensity of the two data-sets was normalised to the background intensity, away from any spectral features.

The strong n-type doping of the buffer layer is still visible as a shift of the K-point to ~2.6 eV. The energy at which the saddle of graphene's π-band or M-point is usually observed is ~2.6 - 3 eV below the K-point depending on the substrate interaction, usually described as a rigid shift in the band structure. Here, the M-point is located at ~4.7 eV which does not correspond to a rigid shift of the graphene band structure. It is not surprising that such large doping modifies the band structure and does not simply give a rigid shift. Also, the π* state of the doped graphene film does not appears to continue linearly below ~1.4 eV, clearly indicating the hybridization of the antibonding π^*-band with the Fe3d bands as seen for graphene on Ni, Co and Fe in *Refs.* [266, 267].

A second clear π-band is seen to intersect the Fermi level at K and K' shown in figure 7.8. This feature compares well with the π-band of quasi-free standing graphene on SiC(0001) substrates [137, 175]. The fact that the buffer layer is still visible (and at comparable intensity) indicates that the free-standing graphene islands are smaller in area than that of the incident photon beam (~300 μm spot size in this system) the resulting data is

therefore an average of the buffer-layer and smaller quasi-free-standing graphene regions. The π-bands shown in figure 7.8 appear broad; this is related to thermal broadening of energy of the emitted photoelectrons, which is quite large here as the measurements were performed at room temperature. Normally high resolution ARPES spectra are collected at low temperature in order to minimise the thermal broadening, however in the case of diamond substrates, cooling to below 120 K results in a freezing of the charge carriers and the substrate becomes too insulating to measure. A precise value of the binding energy at which the K-point is seen is difficult to aquire, however within the uncertainty of the thermal broadening the K-point certainly appears to approach very near the Fermi-level (±0.15 eV). As with the graphene present on the reconstructed diamond surface (See chapter 5 figue 5.12b) the distance between K-points is ∼1.6 $Å^{-1}$ which corresponds well to the size of the graphene Brillouin zone (where the distance of Γ–K is equivalent to that of K–K') of quasi-free-standing graphene grown on SiC(0001)[175], whilst providing more evidence of the lattice registry being carried from the diamond substrate through to the graphene.

7.4 Chapter conclusion

The growth of graphene on $C_{diamond}$(111) has been investigated by introducing the novel addition of thin Fe films that catalytically lower the temperature necessary to break the sp^3-carbon bonds of the substrate and transport the now free carbon atoms to the surface where they are able to recrystallise as sp^2-bonded graphene. Control and a good understanding of the growth process were gained through REES measurements performed in the home laboratory. However the comparably low surface sensitivity of the

technique when MgKα X-rays are used means that a reliable measurement of the amount of carbon present at the surface (and not in the uppermost layers of the Fe film) is difficult. In order to address this, the technique could be performed away from normal emission in order to improve the surface sensitivity, an experiment that as yet has not been performed.

Imaging of the system allowed for an investigation of the lateral formation of graphene on the surface. It was found that large areas which exceeded the field of view of the microscope were formed by annealing the diamond-Fe interface at 500 °C for extended periods. The smoothing monitored in LEEM for the surface indicates that presumably at this temperature a thermal equilibrium phase occurs where the graphene growth is self-terminating due to the lowering of the metal surface free energy. The electronic structure was investigated with ARPES, which revealed that the first graphene layer is strongly interacting with the substrate and displays an n-type doping which causes a non rigid shift in the bands with the K-point lying at ∼2.6 eV. Such large doping does not disturb the linear relationship of the bands around the K-point, Dirac fermions are therefore still assumed as the charge carriers for graphene on thin Fe films. LEEM IV measurements confirm that this layer lies close to the substrate however the magnitude of the oscillation implies that the layer is not bound to the substrate, its proximity to the Fe-layer is related to strong electrostatic forces at the Fe–graphene interface.

The creation of a stable and flat buffer-layer is emphasized as an important step in the production of large area graphene in this case. A small increase in temperature following

the growth of such a buffer layer results in the formation of small islands where vertical growth of the graphene dominates. At higher temperature, graphene emerging from the buffer layer grows predominantly in lateral directions and large areas of quasi-free-standing graphene at least ~25 μm were grown. This graphene showed sharp diffraction patterns and no sign of grain boundaries. From analysis of the band structure it was shown that the graphene shows comparable features to that of free-standing graphene produced via sublimation of Si from SiC(0001) surfaces. This opens up the possibility of controllable growth of graphene at industrially viable temperatures.

Chapter 8 – Related work

The application of a transition metal catalyst that lowers the activation temperature necessary to break the sp^3-carbon bonds in diamond and later form graphene, can also be applied to SiC surfaces[14]. A large body of investigations including; scanning tunnelling microscopy (STM) for real space investigations of the graphene quality, X-ray diffraction measurements to characterise the phase of the FeSi interlayer, as well as ARPES, XPS and LEED characterisation, were used to identify the quality of the grown material. Whilst complementary real-time photoelectron spectroscopy (REES), measurements allowed investigation of the evolving graphene growth.

8.1 – Monitoring the catalytic graphitisation of SiC substrates with REES

For this investigation, a SiC substrate type 6H-(0001) was first given a standard "RCA cleaning" procedure involving hydrofluoric acid (HF) to remove organic contaminants and surface oxides. Following this the substrate was subjected to 950 °C in vacuum annealing before Fe-deposition. Two experiments were conducted involving different Fe film thicknesses of ~1 nm and ~8 nm. During programmed linear anneal cycles (with the 1 nm film increasing to 920 °C), the C1s and $Fe2p_{3/2}$ core level photoelectron peaks were sequentially recorded every 4 seconds.

For the 8 nm film, the C1s photoelectron peak was completely attenuated by the Fe overlayer, allowing the intensity of the emerging graphene C1s component to be analysed. However as photoelectrons excited from the C1s level in this system have a kinetic energy of~970 eV they are still very detectable through the 1nm Fe-film. The formation of graphene can be monitored for such thin films however, due to the different binding energies of the C1s photoelectron peak for SiC and graphene, at 283.3 eV and 284.6 respectively. At a pass energy of 100 eV the C1s peak has a broad ~3 eV FWHM, therefore the growing graphene component will appear within the 'total' C1s photoelectron peak envelope. The intensity of this emerging component is therefore plotted for the thinner Fe film.

In both cases the annealing cycle was linear at a rate of 0.45 °C/s up to 800 °C for the 8 nm film, and 920°C for the 1 nm film. The sample was then held at this temperature for 7

minutes and then cooled slowly to room temperature. The resulting intensity plots are shown in figure 8.1a, along with higher resolution C 1s peaks following cooling in panel b).

8.1.1 Results

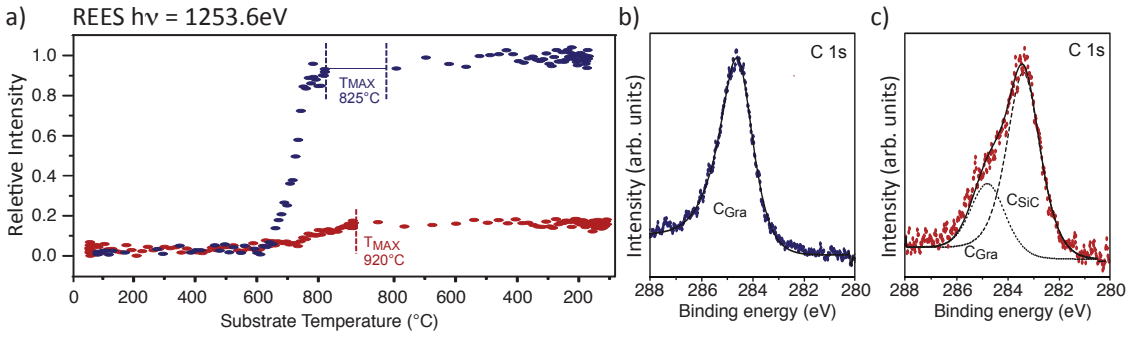

Figure 8.1 a) C1s core level peak intensity for a 1 nm Fe layer (red markers) and a 8 nm Fe layer (blue markers) during a temperature cycle between 20 °C and 825 °C or 920 °C for the thick and thin films respectively. The onset of graphitization for both layers is at 600 °C. b) C1s photoelectron peak of the grown graphene for the 8 nm Fe film. c) C1s photoelectron peak for the 1 nm Fe film. Two clear components are visible and correspond to the C1s peak from graphene and the C1s peak from SiC substrate.

8.2 Discussion and conclusion

For both cases an increase C1s photoelectron peak related to graphene, is seen at a temperature of 600°C. This temperature is less than half of that required graphitise the bare SiC surface at between 1600-1800 °C [14, 157], and allows graphene to be produced on SiC substrates at a much more industrially viable temperature. Interestingly the intensity of the C1s photoelectron peak related to graphene seems to saturate, even when annealed at 320 °C higher than the activation temperature. This indicates that in this Fe-SiC system, instead of the Fe layer acting as a true catalyst, which in the case of diamond continues to absorb carbon from substrate at elevated temperatures, the Fe-films catalytic effect is hindered as Si is accepted in its lattice. The resulting graphene-substrate interface is therefore $C_{graphene}$-FeSi. Analysis of the evaluation of the Si2p photoelectron peak also confirmed the formation of a second component to the peak at lower binding energies, confirming the formation of a silicide. This means that the

number of graphene layers formed can be controlled by the Fe-film thickness, where a thickness of 0.75 (±0.15) nm is expected to result in the formation of a complete graphene monolayer [14].

Chapter 9 – Thesis Summery

The primary aim of this work was to gain an understanding of the process of surface-graphitisation of diamond substrates. Both the clean diamond (111) surface and a metallized diamond (111) surface undergo graphitisation, however in the presence of a transition metal film the temperature required to graphitise the surface is reduced by almost half. Another advantage of the metal-film is that the rate of carbon detachment from the diamond surface can be controlled with temperature. In this work, both of these attributes have been taken advantage of in order to grow high quality graphene.

Initial investigation of the bare diamond surface was afforded through surface processing steps, designed to prepare the best surface for the ultra-thin films of Fe to be deposited onto. The requirement of a clean 1×1 surface allowed investigation of the reconstructed and the hydrogen terminated diamond surfaces. ARPES measurements of the clean reconstructed surface, recorded with the current technological sophistication of photon sources and analysers, allow for images of the band structure to be generated unlike any seen in the literature. Evidence towards the existence of metallic surface states on this surface hints towards original hypothesis of band gaps [88] being a result of the sample (or system) used in this early work and not truly representative of the actual electronic structure. The resulting Fermi-surface image categorically indicates the existence of three 2×1 rotational domains on the surface, as it agrees very well with Pandey's original theoretical calculations [92], which oppose the idea of a 2×2 surface reconstruction. A result that has not been demonstrated as yet in the literature was the graphitisation of diamond surfaces at ~1000 °C which, formed quasi-free-standing graphene regions on

the surface. ARPES measurements confirmed the nature of the π-band seen did in fact match that of graphene, which could indicate a method for directly producing the material on an insulating substrate.

Epitaxy was discussed in the literature review as a prerequisite of forming high quality graphene areas. For this reason an investigation of the epitaxy of ultra-thin films of Fe on the diamond (111) surface were undertaken. It was found that initial growth of the Fe-film matches well to the diamond substrate, however possibly strained as only a diffuse 1×1 diffraction pattern for the overlayer was seen. An obvious phase transformation occurs for the film when annealed to ~340 °C. In this work, as with others see *Refs.*[114, 262, 263], the phase transition is believed to be towards a bcc (110) Fe lattice. The effect on constraining such rectangular lattices on the hexagonal lattice of the substrate is however the formation of rotational domains, and models of the possible results have been presented. A definitive understanding of the phase transition is however not detailed and therefore requires further work, possibly involving STM characterisation.

The process of graphene growth was initially investigated with REES measurements, where precise control of the growth could be maintained by continuous evaluation of the $Fe2p_{3/2}$ and C1s photoelectron peaks. Further investigations involving spectroscopic imaging allowed for the true growth mode of graphene to be characterised. The activation temperature required to promote carbon to the surface was seen to be as low as 495 °C. The variation in activation temperature across the measurements performed indicates that the catalyst film thickness and rate of temperature increase play an

important role in the formation of high quality graphene. Large areas of graphene were created on this system, however the graphene is strongly interacting with the substrate, with a shift of ∼2.6 eV for the K-point to a higher binding energy. Quasi-free standing areas also followed formation of the first strongly interacting layer, showing that this growth process is capable of controllably producing bi-layer and multi-layer graphene stacks. A problem of some self-limiting methods of graphene production [198].

Finally, by applying the same catalytic processing to the surfaces of SiC 6H-(0001), graphene regions of high quality were grown at drastically reduced temperatures when compared to conventional sublimation of Si from SIC. The formation of the FeSi interlayer hinders the catalytic decomposition of carbon into its lattice, which eventually terminates the graphitisation process. This has been shown in REES analysis of the processing steps and indicates a further mechanism of control for the production of graphene, where an ultrathin Fe film of ∼0.75 nm is expected to yield precisely one monolayer of graphene.

Bibliography

1. Geim, A.K. and K.S. Novoselov, *The rise of graphene.* Nat Mater, 2007. **6**(3): p. 183-191.

2. Novoselov, K.S., A.K. Geim, S.V. Morozov, D. Jiang, Y. Zhang, S.V. Dubonos, I.V. Grigorieva, and A.A. Firsov, *Electric Field Effect in Atomically Thin Carbon Films.* Science, 2004. **306**(5696): p. 666-669.

3. Tannock, Q., *Exploiting carbon flatland.* Nat Mater, 2012. **11**(1): p. 2-5.

4. Gomez De Arco, L., Y. Zhang, C.W. Schlenker, K. Ryu, M.E. Thompson, and C. Zhou, *Continuous, Highly Flexible, and Transparent Graphene Films by Chemical Vapor Deposition for Organic Photovoltaics.* ACS Nano, 2010. **4**(5): p. 2865-2873.

5. Balandin, A.A., *Thermal properties of graphene and nanostructured carbon materials.* Nat Mater, 2011. **10**(8): p. 569-581.

6. Rumyantsev, S., G. Liu, M.S. Shur, R.A. Potyrailo, and A.A. Balandin, *Selective Gas Sensing with a Single Pristine Graphene Transistor.* Nano Letters, 2012. **12**(5): p. 2294-2298.

7. Wort, C.J.H. and R.S. Balmer, *Diamond as an electronic material.* Materials Today, 2008. **11**(1–2): p. 22-28.

8. Heggie, M.I., G. Jungnickel, and C.D. Latham, *The theory of CVD diamond growth.* Diamond and Related Materials, 1996. **5**(3–5): p. 236-241.

9. Markham, M.L., J.M. Dodson, G.A. Scarsbrook, D.J. Twitchen, G. Balasubramanian, F. Jelezko, and J. Wrachtrup, *CVD diamond for spintronics.* Diamond and Related Materials, 2011. **20**(2): p. 134-139.

10. Schwander, M. and K. Partes, *A review of diamond synthesis by CVD processes.* Diamond and Related Materials, 2011. **20**(9): p. 1287-1301.

11. Jungnickel, G., D. Porezag, T. Frauenheim, M.I. Heggie, W.R.L. Lambrecht, B. Segall, and J.C. Angus, *Graphitization Effects on Diamond Surfaces and the Diamond/Graphite Interface.* physica status solidi (a), 1996. **154**(1): p. 109-125.

12. Narulkar, R., S. Bukkapatnam, L.M. Raff, and R. Komanduri, *Graphitization as a precursor to wear of diamond in machining pure iron: A molecular dynamics investigation.* Computational Materials Science, 2009. **45**(2): p. 358-366.

13. Narulkar, R., S. Bukkapatnam, L.M. Raff, and R. Komanduri, *Molecular dynamics simulations of diffusion of carbon into iron.* Philosophical Magazine, 2008. **88**(8): p. 1259 - 1275.

14. Cooil, S.P., F. Song, G.T. Williams, O.R. Roberts, D.P. Langstaff, B. Jørgensen, K. Høydalsvik, D.W. Breiby, E. Wahlström, D.A. Evans, and J.W. Wells, *Iron-mediated growth of epitaxial graphene on SiC and diamond.* Carbon, 2012. **50**(14): p. 5099-5105.

15. Evans, D.A., O.R. Roberts, G.T. Williams, A.R. Vearey-Roberts, F. Bain, S. Evans, D.P. Langstaff, and D.J. Twitchen, *Diamond-metal contacts: interface barriers and real-time characterization.* Journal of Physics: Condensed Matter, 2009. **21**(36): p. 364223.

16. Evans, D.A., O.R. Roberts, A.R. Vearey-Roberts, D.P. Langstaff, D.J. Twitchen, and M. Schwitters, *Direct observation of Schottky to ohmic transition in Al-diamond contacts using realtime photoelectron spectroscopy.* Applied Physics Letters, 2007. **91**(13): p. 132114.

17. Fyfe, D.J., *The Surface Properties of Diamond and Cubic Boron Nitride*, in *Institute of Mathematics and Physical Sciences*2001, Aberystwyth University. p. 256.

18. Zakharov, A.A., A.Mikkelsen, and J.N. Andersen, *Recent advances in imaging of properties and growth of low dimensional structures for photonics and electronics by XPEEM.* Journal of Electron Spectroscopy and Related Phenomena, 2012. **185**(10): p. 417-428.

19. Siegbahn, K., *Electron Spectroscopy for Chemical Analysis (E.S.C.A.).* Philosophical Transactions of the Royal Society of London. Series A, Mathematical and Physical Sciences, 1970. **268**(1184): p. 33-57.

20. Kai, S., G. Ulrik, S. Hans, and O. Erik, *Angular Distribution of Electrons in ESCA Spectra from a Single Crystal.* Physica Scripta, 1970. **1**(5-6): p. 272.

21. Hüfner, S., *Photoelectron Spectroscopy: Principles and Applications*. Third Edition ed2003: Springer.

22. Hüfner, S., S. Schmidt, and F. Reinert, *Photoelectron spectroscopy--An overview.* Nuclear Instruments and Methods in Physics Research Section A: Accelerators, Spectrometers, Detectors and Associated Equipment, 2005. **547**(1): p. 8-23.

23. Berglund, C.N. and W.E. Spicer, *Photoemission Studies of Copper and Silver: Theory.* Physical Review, 1964. **136**(4A): p. A1030-A1044.

24. Steiner, P., H. Höchst, and S. Hüfner, *Analysis of the plasmon structure in XPS experiments of simple metals.* Physics Letters A, 1977. **61**(6): p. 410-412.

25. Pollak, R.A., L. Ley, F.R. McFeely, S.P. Kowalczyk, and D.A. Shirley, *Characteristic energy loss structure of solids from X-ray photoemission spectra.* Journal of Electron Spectroscopy and Related Phenomena, 1974. **3**(5): p. 381-398.

26. Hesse, R., P. Streubel, and R. Szargan, *Product or sum: comparative tests of Voigt, and product or sum of Gaussian and Lorentzian functions in the fitting of synthetic*

Voigt-based X-ray photoelectron spectra. Surface and Interface Analysis, 2007. **39**(5): p. 381-391.

27. Doniach, S. and M. Sunjic, *Many-electron singularity in X-ray photoemission and X-ray line spectra from metals.* Journal of Physics C: Solid State Physics, 1970. **3**(2): p. 285.

28. Mahan, G.D., *Excitons in Metals: Infinite Hole Mass.* Physical Review, 1967. **163**(3): p. 612-617.

29. Saloman, E.B., J.H. Hubbell, and J.H. Scofield, *X-ray attenuation cross sections for energies 100 eV to 100 keV and elements Z = 1 to Z = 92.* Atomic Data and Nuclear Data Tables, 1988. **38**(1): p. 1-196.

30. Scofield, J.H., *Hartree-Slater subshell photoionization cross-sections at 1254 and 1487 eV.* Journal of Electron Spectroscopy and Related Phenomena, 1976. **8**(2): p. 129-137.

31. C.J. Powel, *NIST- Electron effective attenuation database.*, A. Jablonski, Editor 2011.

32. Allen, M.J., V.C. Tung, and R.B. Kaner, *Honeycomb Carbon: A Review of Graphene.* Chemical Reviews, 2009. **110**(1): p. 132-145.

33. Roy, D. and D. Tremblay, *Design of electron spectrometers.* Reports on Progress in Physics, 1990. **53**(12): p. 1621.

34. Watts, J.F. and J. Wolstenholme, *An Introduction to Surface Analysis by XPS and AES*2003: Wiley.

35. SPECS. *Extended Range Channel Electron Multiplier (CEM)*. Available from: http://www.specs.de/cms/front_content.php?idcat=181.

36. Manning, P.P., N.J. Clague, I.W. Kirkman, F.M. Quinn, and P.J. Hicks, *A fast and flexible multichannel electron detector with parallel readout for photoelectron spectroscopy.* Nuclear Instruments and Methods in Physics Research Section A: Accelerators, Spectrometers, Detectors and Associated Equipment, 1997. **392**(1–3): p. 345-348.

37. Richter, L.J. and W. Ho, *Position-Sensitive Detector Performance and Relevance to Time-Resolved Electron-Energy Loss Spectroscopy.* Review of Scientific Instruments, 1986. **57**(8): p. 1469-1482.

38. Ladislas Wiza, J., *Microchannel plate detectors.* Nuclear Instruments and Methods, 1979. **162**(1-3): p. 587-601.

39. Langstaff, D.P., A. Bushell, T. Chase, and D.A. Evans, *A fully integrated multi-channel detector for electron spectroscopy.* Nuclear Instruments and Methods in Physics Research Section B: Beam Interactions with Materials and Atoms, 2005. **238**(1-4): p. 219-223.

40. Langstaff, D.P. and T. Chase, *A multichannel detector array with 768 pixels developed for electron spectroscopy.* Nuclear Instruments and Methods in Physics Research Section A: Accelerators, Spectrometers, Detectors and Associated Equipment, 2007. **573**(1–2): p. 169-171.

41. Zhu, X. and D.P. Langstaff, *Reduction of multiple triggering in counting detectors.* Nuclear Instruments and Methods in Physics Research Section A: Accelerators, Spectrometers, Detectors and Associated Equipment, 2009. **604**(1–2): p. 400-403.

42. W.S. Boyle, G.E.S., *Charged Couples Semiconductor Devices.* Bell Systems Technical Journal 1970. **49**(4): p. 587-593.

43. G.E. Smith, M.F.T., G.F. Amelio, *Experimental Verification of the Charged Coupled Semiconductor Device Concept.* Bell Systems Technical Journal, 1970. **49**(4): p. 593-600.

44. Brüche, E., *Elektronenmikroskopische Abbildung mit lichtelektrischen Elektronen.* Zeitschrift für Physik, 1933. **86**(7-8): p. 448-450.

45. Beamson, G., H.Q. Porter, and D.W. Turner, *Photoelectron spectromicroscopy.* Nature, 1981. **290**(5807): p. 556-561.

46. Recknagel, A., *Theorie des elektrischen Elektronenmikroskops für Selbststrahler.* Zeitschrift für Physik, 1941. **117**(11-12): p. 689-708.

47. Boersch, H., *Die Verbesserung Des Auflösungsvermögen usw.* Z. Tech. Phys, 1942. **23**: p. 2.

48. Koch, W., *Ein hochauflösendes Emissions-Mikroskop zur Sichtbarmachung von Oberflächen mit UV-ausgelösten Elektronen.* Zeitschrift für Physik, 1958. **152**(1): p. 1-18.

49. J. Chmelik, L.V., G. Marx, *Comparing cathode lens configurations for low energy electron microscopy*. Vol. 83. 1989, Reutlingen, ALLEMAGNE: Elsevier.

50. Telieps, W. and E. Bauer, *An analytical reflection and emission UHV surface electron microscope.* Ultramicroscopy, 1985. **17**(1): p. 57-65.

51. Tonner, B.P. and G.R. Harp, *Photoelectron microscopy with synchrotron radiation.* Review of Scientific Instruments, 1988. **59**(6): p. 853-858.

52. Locatelli, A., T.O. Menteş, M.Á. Niño, and E. Bauer, *Image blur and energy broadening effects in XPEEM.* Ultramicroscopy, 2011. **111**(8): p. 1447-1454.

53. Tonner, B.P., D. Dunham, T. Droubay, and M. Pauli, *A photoemission microscope with a hemispherical capacitor energy filter.* Journal of Electron Spectroscopy and Related Phenomena, 1997. **84**(1–3): p. 211-229.

54. Schmidt, T.H., *XPEEM with Energy Filtering: Advantages and first results from the SMART Project.* Surface Review and Letters, 2002. **09**(01): p. 223-232.

55. Marx, G.K.L., V. Gerheim, and G. Schönhense, *Multipole WIEN-filter for a high-resolution X-PEEM.* Journal of Electron Spectroscopy and Related Phenomena, 1997. **84**(1–3): p. 251-261.

56. Spiecker, H., O. Schmidt, C. Ziethen, D. Menke, U. Kleineberg, R.C. Ahuja, M. Merkel, U. Heinzmann, and G. Schönhense, *Time-of-flight photoelectron emission microscopy TOF-PEEM: first results.* Nuclear Instruments and Methods in Physics Research Section A: Accelerators, Spectrometers, Detectors and Associated Equipment, 1998. **406**(3): p. 499-506.

57. Oral, M., T. Radlička, and B. Lencová, *Effect of sample tilt on PEEM resolution.* Ultramicroscopy, 2012. **119**(0): p. 45-50.

58. Schmidt, T., H. Marchetto, P.L. Lévesque, U. Groh, F. Maier, D. Preikszas, P. Hartel, R. Spehr, G. Lilienkamp, W. Engel, R. Fink, E. Bauer, H. Rose, E. Umbach, and H.J. Freund, *Double aberration correction in a low-energy electron microscope.* Ultramicroscopy, 2010. **110**(11): p. 1358-1361.

59. Schmidt, T., A. Sala, H. Marchetto, E. Umbach, and H.J. Freund, *First experimental proof for aberration correction in XPEEM: Resolution, transmission enhancement, and limitation by space charge effects.* Ultramicroscopy, 2013. **126**(0): p. 23-32.

60. Tromp, R.M., J.B. Hannon, A.W. Ellis, W. Wan, A. Berghaus, and O. Schaff, *A new aberration-corrected, energy-filtered LEEM/PEEM instrument. I. Principles and design.* Ultramicroscopy, 2010. **110**(7): p. 852-861.

61. Tromp, R.M., J.B. Hannon, W. Wan, A. Berghaus, and O. Schaff, *A new aberration-corrected, energy-filtered LEEM/PEEM instrument II. Operation and results.* Ultramicroscopy, 2013. **127**(0): p. 25-39.

62. Elmitec. *Aberation correct SPELEEM*. 2012; Available from: http://www.elmitec.de/AC.php?Bereich=Highlights.

63. Specs, G., *The SPECS LEEM instrument: FE-LEEM P90.* 2013.

64. Bauer, E., *Low Energy Electron Microscopy and Normal Incidence Vleed*, in *Studies in Surface Science and Catalysis*, J. Koukal, Editor 1988, Elsevier. p. 26-36.

65. Bauer, E., *Photoelectron microscopy.* Journal of Physics: Condensed Matter, 2001. **13**(49): p. 11391.

66. Schmidt, T., S. Heun, J. Slezak, J. Diaz, K.C. Prince, G. Lilienkamp, and E. Bauer, *SPELEEM: Combining LEEM and Spectroscopic Imaging.* Surface Review and Letters, 1998. **05**(06): p. 1287-1296.

67. Woodruff, D.P., *Photoelectron diffraction for quantitative determination of adsorption structures on surfaces.* Physica B: Condensed Matter, 1995. **208–209**(0): p. 423-426.

68. Dupuy, J.C., A. Sibai, and B. Vilotitch, *Mirror Electron Microscopy (MEM): Work function and imaging of an electron beam biased junction of silicon (100).* Surface Science, 1984. **147**(1): p. 191-202.

69. Hibino, H., H. Kageshima, F. Maeda, M. Nagase, Y. Kobayashi, and H. Yamaguchi, *Microscopic thickness determination of thin graphite films formed on SiC from quantized oscillation in reflectivity of low-energy electrons.* Physical Review B, 2008. **77**(7): p. 075413.

70. Isberg, J., J. Hammersberg, D.J. Twitchen, and A.J. Whitehead, *Single crystal diamond for electronic applications.* Diamond and Related Materials, 2004. **13**(2): p. 320-324.

71. Fries, M.D. and Y.K. Vohra, *Properties of nanocrystalline diamond thin films grown by MPCVD for biomedical implant purposes.* Diamond and Related Materials, 2004. **13**(9): p. 1740-1743.

72. Blank, V., M. Popov, G. Pivovarov, N. Lvova, K. Gogolinsky, and V. Reshetov, *Ultrahard and superhard phases of fullerite C60: Comparison with diamond on hardness and wear.* Diamond and Related Materials, 1998. **7**(2–5): p. 427-431.

73. May, P.W., *Diamond thin films: a 21st-century material.* Chemisty and Biological Physics, Roy Soc, 2000. **358**(1766): p. 473.

74. Selschop, J.P.F., *Properties of Diamond.* Academic Press London, 1979.

75. Robertson, R., J.J. Fox, and A.E. Martin, *Two Types of Diamond.* Philosophical Transactions of the Royal Society of London. Series A, Containing Papers of a Mathematical or Physical Character, 1934. **232**(ArticleType: research-article / Full publication date: 1934 / Copyright © 1934 The Royal Society): p. 463-535.

76. Custers, J.F.H., *Unusual phosphorescence of a diamond.* Physica, 1952. **18**(8–9): p. 489-496.

77. Bundy, F.P., H.T. Hall, H.M. Strong, and R.H. Wentorf, *Man-Made Diamonds.* Nature, 1955. **176**(4471): p. 51-55.

78. Ashfold, M., P. May, C. Rego, and N. Everitt, *Thin film diamond by chemical vapour deposition methods.* Chem. Soc. Rev., 1994. **23**(1): p. 21-30.

79. Joe, R., T.A. Badgwell, and R.H. Hauge, *Atomic carbon insertion as a low-substrate-temperature growth mechanism in diamond CVD.* Diamond and Related Materials, 1998. **7**(9): p. 1364-1374.

80. Kawano, A., H. Ishiwata, S. Iriyama, R. Okada, S. Kitagoh, M. Watanabe, Y. Takano, T. Yamaguchi, and H. Kawarada, *Critical concentrations of superconductor to insulator transition in (111) and (001) CVD boron-doped diamond.* Physica C: Superconductivity, 2010. **470, Supplement 1**(0): p. S604-S607.

81. Tokuda, N., T. Saito, H. Umezawa, H. Okushi, and S. Yamasaki, *The role of boron atoms in heavily boron-doped semiconducting homoepitaxial diamond growth — Study of surface morphology.* Diamond and Related Materials, 2007. **16**(2): p. 409-411.

82. Lagrange, J.P., A. Deneuville, and E. Gheeraert, *Activation energy in low compensated homoepitaxial boron-doped diamond films.* Diamond and Related Materials, 1998. **7**(9): p. 1390-1393.

83. Kern, G., J. Hafner, and G. Kresse, *Atomic and electronic structure of diamond (111) surfaces. I. Reconstruction and hydrogen-induced deconstruction of the one dangling-bond surface (vol 366, pg 445, 1996).* Surface Science, 1998. **396**(1-3): p. 431-432.

84. Chu, C.J., M.P. D'Evelyn, R.H. Hauge, and J.L. Margrave, *Mechanism of diamond growth by chemical vapor deposition on diamond (100), (111), and (110) surfaces: Carbon-13 studies.* Journal of Applied Physics, 1991. **70**(3): p. 1695-1705.

85. Ghodbane, S., D. Ballutaud, F. Omnès, and C. Agnès, *Comparison of the XPS spectra from homoepitaxial {111}, {100} and polycrystalline boron-doped diamond films.* Diamond and Related Materials. **19**(5-6): p. 630-636.

86. ElementSix™. *Synthetic Diamonds*. 2013; Available from: http://www.e6.com/wps/wcm/connect/E6_Content_EN/Home/Materials+and+products/Single+crystal+synthetic+diamond/CVD+synthetic+diamond/.

87. Kern, G., J. Hafner, J. Furthmüller, and G. Kresse, *(2 × 1) reconstruction and hydrogen-induced de-reconstruction of the diamond (100) and (111) surfaces.* Surface Science, 1996. **352–354**(0): p. 745-749.

88. Graupner, R., M. Hollering, A. Ziegler, J. Ristein, L. Ley, and A. Stampfl, *Dispersions of surface states on diamond (100) and (111).* Physical Review B, 1997. **55**(16): p. 10841.

89. Ristein, J., *Chapter 2 Structural and electronic properties of diamond surfaces*, in *Semiconductors and Semimetals*, E.N. Christoph and R. Jürgen, Editors. 2004, Elsevier. p. 37-96.

90. Painter, G.S., D.E. Ellis, and A.R. Lubinsky, *Ab Initio Calculation of the Electronic Structure and Optical Properties of Diamond Using the Discrete Variational Method.* Physical Review B, 1971. **4**(10): p. 3610-3622.

91. Himpsel, F.J., J.F. van der Veen, and D.E. Eastman, *Experimental bulk energy bands for diamond using hv-dependent photoemission.* Physical Review B, 1980. **22**(4): p. 1967-1971.

92. Pandey, K.C., *New dimerized-chain model for the reconstruction of the diamond (111)-(2 × 1) surface.* Physical Review B, 1982. **25**(6): p. 4338-4341.

93. Pate, B.B., *The diamond surface: atomic and electronic structure.* Surface Science, 1986. **165**(1): p. 142.

94. Hamza, A.V., G.D. Kubiak, and R.H. Stulen, *The role of hydrogen on the diamond C(111)−(2 × 1) reconstruction.* Surface Science, 1988. **206**(1–2): p. L833-L844.

95. Phillips, J.C., *Theory of semiconductor surfaces.* Surface Science, 1975. **53**(1): p. 474-487.

96. Lander, J.J. and J. Morrison, *Low energy electron diffraction study of the (111) diamond surface.* Surface Science, 1966. **4**(3): p. 241-246.

97. Jungnickel, G., C.D. Latham, M.I. Heggie, and T. Frauenheim, *On the graphitization of diamond surfaces: the importance of twins.* Diamond and Related Materials, 1996. **5**(1): p. 102-107.

98. Derry, T.E. and N.W. Makau, *Carbon atom exchange between the diamond surface and lubricant during polishing.* Diamond and Related Materials, 2006. **15**(1): p. 160-163.

99. Kawarada, H., *Hydrogen-terminated diamond surfaces and interfaces.* Surface Science Reports, 1996. **26**(7): p. 205-206.

100. Shirafuji, J., Y. Sakamoto, A. Furukawa, H. Shigeta, and T. Sugino, *X-ray photoelectron spectroscopy analysis of plasma-treated surfaces of diamond films.* Diamond and Related Materials, 1995. **4**(7): p. 984-988.

101. Hamza, A.V., G.D. Kubiak, and R.H. Stulen, *Hydrogen chemisorption and the structure of the diamond C(100)-(2 × 1) surface.* Surface Science, 1990. **237**(1–3): p. 35-52.

102. Lurie, P.G. and J.M. Wilson, *The diamond surface: II. Secondary electron emission.* Surface Science, 1977. **65**(2): p. 476-498.

103. Bandis, C. and B.B. Pate, *Photoelectric emission from negative-electron-affinity diamond (111) surfaces: Exciton breakup versus conduction-band emission.* Physical Review B, 1995. **52**(Copyright (C) 2010 The American Physical Society): p. 12056.

104. Cui, J.B., R. Graupner, J. Ristein, and L. Ley, *Electron affinity and band bending of single crystal diamond (111) surface.* Diamond and Related Materials, 1999. **8**(2-5): p. 748-753.

105. Cui, J.B., J. Ristein, and L. Ley, *Electron Affinity of the Bare and Hydrogen Covered Single Crystal Diamond (111) Surface.* Physical Review Letters, 1998. **81**(Copyright (C) 2010 The American Physical Society): p. 429.

106. Diederich, L., O.M. KÜttel, P. Aebi, and L. Schlapbach, *Electron affinity and work function of differently oriented and doped diamond surfaces determined by photoelectron spectroscopy.* Surface Science, 1998. **418**(1): p. 219-239.

107. Ristein, J., *Electronic properties of diamond surfaces -- blessing or curse for devices?* Diamond and Related Materials, 2000. **9**(3-6): p. 1129-1137.

108. Rawles, R.E., S.F. Komarov, R. Gat, W.G. Morris, J.B. Hudson, and M.P. D'Evelyn, *Mechanism of surface smoothing of diamond by a hydrogen plasma.* Diamond and Related Materials, 1997. **6**(5-7): p. 791-795.

109. van Bouwelen, F.M., *Diamond polishing from different angles.* Diamond and Related Materials, 2000. **9**(3-6): p. 925-928.

110. Maier, F., M. Riedel, J. Ristein, and L. Ley, *Spectroscopic investigations of diamond/hydrogen/metal and diamond/metal interfaces.* Diamond and Related Materials, 2001. **10**(3-7): p. 506-510.

111. Muret, P., F. Pruvost, C. Saby, E. Lucazeau, T.A. Nguyen Tan, E. Gheeraert, and A. Deneuville, *Carbide contacts on homoepitaxial diamond films.* Diamond and Related Materials, 1999. **8**(2-5): p. 961-965.

112. Evans, S.a.N., M.R., *Cobalt-catalysed graphitisation of diamond studied by XPS.* J. Hard. Matt, 1990. **1**(2): p. 196.

113. Lurie, P.G. and J.M. Wilson, *The diamond surface: I. The structure of the clean surface and the interaction with gases and metals.* Surface Science, 1977. **65**(2): p. 453-475.

114. Kief, M.T. and W.F. Egelhoff, *Growth and structure of Fe and Co thin films on Cu(111), Cu(100), and Cu(110): A comprehensive study of metastable film growth.* Physical Review B, 1993. **47**(16): p. 10785.

115. Roberts, O.R., *The Application of Real-time Photoelectron Spectroscopy to Carbon Based Semiconductors.* Thesis submitted to Aberystwyth University, 2009.

116. Slonczewski, J.C. and P.R. Weiss, *Band Structure of Graphite.* Physical Review, 1958. **109**(2): p. 272-279.

117. Wallace, P.R., *The Band Theory of Graphite.* Physical Review, 1947. **71**(9): p. 622-634.

118. Peierls, R.E., *Bemerkungen über Umwandlungstemperaturen.* Helv. Phys. Acta, 1934. **7**: p. 2.

119. Landau, L.D., *Zur theorie der phasenumwandlungen II.* Phys. Z. Sowjetunion, 1937. **11**: p. 9.

120. Malard, L.M., M.A. Pimenta, G. Dresselhaus, and M.S. Dresselhaus, *Raman spectroscopy in graphene.* Physics Reports, 2009. **473**(5-6): p. 51-87.

121. Liu, H., Y. Liu, and D. Zhu, *Chemical doping of graphene.* Journal of Materials Chemistry, 2011. **21**(10): p. 3335-3345.

122. Park, H., J.A. Rowehl, K.K. Kim, V. Bulovic, and J. Kong, *Doped graphene electrodes for organic solar cells.* Nanotechnology, 2010. **21**(50): p. 505204.

123. Adam, S. and S. Das Sarma, *Transport in suspended graphene.* Solid State Communications, 2008. **146**(9-10): p. 356-360.

124. Adam, S., E.H. Hwang, and S. Das Sarma, *Scattering mechanisms and Boltzmann transport in graphene.* Physica E: Low-dimensional Systems and Nanostructures, 2008. **40**(5): p. 1022-1025.

125. Das Sarma, S., S. Adam, E.H. Hwang, and E. Rossi, *Electronic transport in two-dimensional graphene.* Reviews of Modern Physics, 2011. **83**(2): p. 407-470.

126. Mucciolo, E.R. and C.H. Lewenkopf, *Disorder and electronic transport in graphene.* Journal of Physics: Condensed Matter, 2010. **22**(27): p. 273201.

127. Bonaccorso, F., Z. Sun, T. Hasan, and A.C. Ferrari, *Graphene photonics and optoelectronics.* Nat Photon, 2010. **4**(9): p. 611-622.

128. Dlubak, B., M.-B. Martin, R.S. Weatherup, H. Yang, C. Deranlot, R. Blume, R. Schloegl, A. Fert, A. Anane, S. Hofmann, P. Seneor, and J. Robertson, *Graphene-Passivated Nickel as an Oxidation-Resistant Electrode for Spintronics.* ACS Nano, 2012. **6**(12): p. 10930-10934.

129. Zarea, M. and N. Sandler, *Quantum spin Hall phase in neutral zigzag graphene ribbons.* Physica B: Condensed Matter, 2009. **404**(18): p. 2694-2698.

130. Lee, C., X. Wei, J.W. Kysar, and J. Hone, *Measurement of the Elastic Properties and Intrinsic Strength of Monolayer Graphene.* Science, 2008. **321**(5887): p. 385-388.

131. Liu, F., P. Ming, and J. Li, *Ab initio calculation of ideal strength and phonon instability of graphene under tension.* Physical Review B, 2007. **76**(6): p. 064120.

132. Bae, S., H. Kim, Y. Lee, X. Xu, J.-S. Park, Y. Zheng, J. Balakrishnan, T. Lei, H. Ri Kim, Y.I. Song, Y.-J. Kim, K.S. Kim, B. Ozyilmaz, J.-H. Ahn, B.H. Hong, and S. Iijima, *Roll-to-roll production of 30-inch graphene films for transparent electrodes.* Nat Nano, 2010. **5**(8): p. 574-578.

133. Ratinac, K.R., W. Yang, S.P. Ringer, and F. Braet, *Toward Ubiquitous Environmental Gas Sensors—Capitalizing on the Promise of Graphene.* Environmental Science & Technology, 2010. **44**(4): p. 1167-1176.

134. Chen, D., H. Feng, and J. Li, *Graphene Oxide: Preparation, Functionalization, and Electrochemical Applications.* Chemical Reviews, 2012. **112**(11): p. 6027-6053.

135. Novoselov, K.S., V.I. Falko, L. Colombo, P.R. Gellert, M.G. Schwab, and K. Kim, *A roadmap for graphene.* Nature, 2012. **490**(7419): p. 192-200.

136. Trauzettel, B., D.V. Bulaev, D. Loss, and G. Burkard, *Spin qubits in graphene quantum dots.* Nat Phys, 2007. **3**(3): p. 192-196.

137. Forti, S., K.V. Emtsev, C. Coletti, A.A. Zakharov, C. Riedl, and U. Starke, *Large-area homogeneous quasifree standing epitaxial graphene on SiC(0001): Electronic and structural characterization.* Physical Review B, 2011. **84**(12): p. 125449.

138. Meyer, J.C., A.K. Geim, M.I. Katsnelson, K.S. Novoselov, T.J. Booth, and S. Roth, *The structure of suspended graphene sheets.* Nature, 2007. **446**(7131): p. 60-63.

139. V. Ariel, Natan, A. , *Electron Effective Mass in Graphene*, in *ArXiv e-prints* http://arxiv.org/abs/1206.61002012.

140. Ariel, V., *Effective Mass and Energy Mass Relationship*, in *ArXiv e-prints* http://arxiv.org/abs/1205.3995v12012.

141. Rössler, U., *Solid State Theory: An Introduction*2009: Physica-Verlag.

142. Castro, A.H.*e.a.*, *The electronic properties of graphene.* Reviews of Modern Physics, 2009. **81**: p. 109.

143. Deacon, R.S., K.C. Chuang, R.J. Nicholas, K.S. Novoselov, and A.K. Geim, *Cyclotron resonance study of the electron and hole velocity in graphene monolayers.* Physical Review B (Condensed Matter and Materials Physics), 2007. **76**(8): p. 081406-4.

144. Vozmediano, M.A.H., *Graphene: The running of the constants.* Nat Phys, 2011. **7**(9): p. 671-672.

145. Elias, D.C., R.V. Gorbachev, A.S. Mayorov, S.V. Morozov, A.A. Zhukov, P. Blake, L.A. Ponomarenko, I.V. Grigorieva, K.S. Novoselov, F. Guinea, and A.K. Geim, *Dirac cones reshaped by interaction effects in suspended graphene.* Nat Phys, 2011. **7**(9): p. 701-704.

146. Peres, N.M.R., *The electronic properties of graphene and its bilayer.* Vacuum, 2009. **83**(10): p. 1248-1252.

147. Novoselov, K.S., Z. Jiang, Y. Zhang, S.V. Morozov, H.L. Stormer, U. Zeitler, J.C. Maan, G.S. Boebinger, P. Kim, and A.K. Geim, *Room-Temperature Quantum Hall Effect in Graphene.* Science, 2007. **315**(5817): p. 1379-.

148. Wolfram-Demonstration-Projects. *Graphene Brillouin Zone and Electronic Energy Dispersion*. 2013; Available from: http://demonstrations.wolfram.com/GrapheneBrillouinZoneAndElectronicEnergyDispersion/.

149. McCann, E. and V.I. Fal'ko, *Landau-Level Degeneracy and Quantum Hall Effect in a Graphite Bilayer.* Physical Review Letters, 2006. **96**(8): p. 086805.

150. Yan, W., W.-Y. He, Z.-D. Chu, M. Liu, L. Meng, R.-F. Dou, Y. Zhang, Z. Liu, J.-C. Nie, and L. He, *Strain and curvature induced evolution of electronic band structures in twisted graphene bilayer.* Nat Commun, 2013. **4**.

151. Castro, E.V., K.S. Novoselov, S.V. Morozov, N.M.R. Peres, J.M.B.L. dos Santos, J. Nilsson, F. Guinea, A.K. Geim, and A.H.C. Neto, *Biased Bilayer Graphene: Semiconductor with a Gap Tunable by the Electric Field Effect.* Physical Review Letters, 2007. **99**(21): p. 216802.

152. Terrones, M., A.R. Botello-MÈndez, J. Campos-Delgado, F. LÛpez-Urìas, Y.I. Vega-Cant˙, F.J. Rodrìguez-Macìas, A.L. Elìas, E. MuÒoz-Sandoval, A.G. Cano-M·rquez, J.-C. Charlier, and H. Terrones, *Graphene and graphite nanoribbons: Morphology, properties, synthesis, defects and applications.* Nano Today, 2010. **5**(4): p. 351-372.

153. Hashimoto, A., K. Suenaga, A. Gloter, K. Urita, and S. Iijima, *Direct evidence for atomic defects in graphene layers.* Nature, 2004. **430**(7002): p. 870-873.

154. Ma, J., D. Alfè, A. Michaelides, and E. Wang, *Stone-Wales defects in graphene and other planar sp^{2}-bonded materials.* Physical Review B, 2009. **80**(3): p. 033407.

155. Kang, J., J. Bang, B. Ryu, and K.J. Chang, *Effect of atomic-scale defects on the low-energy electronic structure of graphene: Perturbation theory and local-density-functional calculations.* Physical Review B, 2008. **77**(11): p. 115453.

156. Botello-Méndez, A.R., F. López-Urías, E. Cruz-Silva, B.G. Sumpter, V. Meunier, M. Terrones, and H. Terrones, *The importance of defects for carbon nanoribbon based electronics.* physica status solidi (RRL) – Rapid Research Letters, 2009. **3**(6): p. 181-183.

157. First, P.N., W.A. de Heer, T. Seyller, C. Berger, J.A. Stroscio, and J.-S. Moon, *Epitaxial Graphenes on Silicon Carbide.* MRS Bulletin, 2010. **35**(04): p. 296-305.

158. de Heer, W.A., C. Berger, X. Wu, P.N. First, E.H. Conrad, X. Li, T. Li, M. Sprinkle, J. Hass, M.L. Sadowski, M. Potemski, and G. Martinez, *Epitaxial graphene.* Solid State Communications, 2007. **143**(1-2): p. 92-100.

159. Reina, A., S. Thiele, X. Jia, S. Bhaviripudi, M. Dresselhaus, J. Schaefer, and J. Kong, *Growth of large-area single- and Bi-layer graphene by controlled carbon precipitation on polycrystalline Ni surfaces.* Nano Research, 2009. **2**(6): p. 509-516.

160. Reina, A., X. Jia, J. Ho, D. Nezich, H. Son, V. Bulovic, M.S. Dresselhaus, and J. Kong, *Large Area, Few-Layer Graphene Films on Arbitrary Substrates by Chemical Vapor Deposition.* Nano Letters, 2008. **9**(1): p. 30-35.

161. Coleman, J.N., *Liquid Exfoliation of Defect-Free Graphene.* Accounts of Chemical Research, 2012. **46**(1): p. 14-22.

162. Dato, A., V. Radmilovic, Z. Lee, J. Phillips, and M. Frenklach, *Substrate-Free Gas-Phase Synthesis of Graphene Sheets.* Nano Letters, 2008. **8**(7): p. 2012-2016.

163. Chen, C., Q.-H. Yang, Y. Yang, W. Lv, Y. Wen, P.-X. Hou, M. Wang, and H.-M. Cheng, *Self-Assembled Free-Standing Graphite Oxide Membrane.* Advanced Materials, 2009. **21**(29): p. 3007-3011.

164. Cuong, T.V., V.H. Pham, Q.T. Tran, S.H. Hahn, J.S. Chung, E.W. Shin, and E.J. Kim, *Photoluminescence and Raman studies of graphene thin films prepared by reduction of graphene oxide.* Materials Letters, 2009. **In Press, Corrected Proof**.

165. Becerril, H.A., J. Mao, Z. Liu, R.M. Stoltenberg, Z. Bao, and Y. Chen, *Evaluation of Solution-Processed Reduced Graphene Oxide Films as Transparent Conductors.* ACS Nano, 2008. **2**(3): p. 463-470.

166. Matsunami, H. and T. Kimoto, *Step-controlled epitaxial growth of SiC: High quality homoepitaxy.* Materials Science and Engineering: R: Reports, 1997. **20**(3): p. 125-166.

167. Adamsky, R.F. and K.M. Merz, *Synthesis and crystallography of the wurtzite form of silicon carbide.* Zeitschrift für Kristallographie - Crystalline Materials, 1959. **111**(1-6): p. 350-361.

168. Feng, Z.C. and J.H. Zhao, *Silicon Carbide: Materials, Processing, and Devices*2004: Taylor & Francis.

169. Tsong, I.S.T. and L. Li, *Atomic structures of 6H-SiC (0001) and (0001) surfaces.* Surface Science, 1996. **351**(1): p. 141-148.

170. An, B., S. Fukuyama, and K. Yokogawa, *Graphitization of 6H SiC (0001) Surface by Scanning Tunneling Microscopy.* Japanese Journal of Applied Physics. **41**(Copyright (C) 2002 The Japan Society of Applied Physics): p. 4890.

171. Chang, C.S., I.S.T. Tsong, Y.C. Wang, and R.F. Davis, *Scanning tunneling microscopy and spectroscopy of cubic β-SiC(111) surfaces.* Surface Science, 1991. **256**(3): p. 354-360.

172. Owman, F. and P. Mårtensson, *The SiC(0001)6√3 × 6√3 reconstruction studied with STM and LEED.* Surface Science, 1996. **369**(1–3): p. 126-136.

173. Berger, C., Z. Song, T. Li, X. Li, A.Y. Ogbazghi, R. Feng, Z. Dai, A.N. Marchenkov, E.H. Conrad, P.N. First, and W.A. de Heer, *Ultrathin Epitaxial Graphite: 2D Electron Gas Properties and a Route toward Graphene-based Nanoelectronics.* The Journal of Physical Chemistry B, 2004. **108**(52): p. 19912-19916.

174. Starke, U. and C. Riedl, *Epitaxial graphene on SiC(0001) and SiC(0001–) : from surface reconstructions to carbon electronics.* Journal of Physics: Condensed Matter, 2009. **21**(13): p. 134016.

175. Emtsev, K.V., F. Speck, T. Seyller, L. Ley, and J.D. Riley, *Interaction, growth, and ordering of epitaxial graphene on SiC{0001} surfaces: A comparative photoelectron spectroscopy study.* Physical Review B, 2008. **77**(15): p. 155303.

176. Emtsev, K.V., F. Speck, T. Seyller, L. Ley, and J.D. Riley, *Interaction, growth, and ordering of epitaxial graphene on SiC{0001} surfaces: A comparative photoelectron*

spectroscopy study. Physical Review B (Condensed Matter and Materials Physics), 2008. **77**(15): p. 155303.

177. Watcharinyanon, S., L.I. Johansson, A.A. Zakharov, and C. Virojanadara, *Studies of Li intercalation of hydrogenated graphene on SiC(0001).* Surface Science, 2012. **606**(3–4): p. 401-406.

178. Riedl, C., C. Coletti, T. Iwasaki, A.A. Zakharov, and U. Starke, *Quasi-Free-Standing Epitaxial Graphene on SiC Obtained by Hydrogen Intercalation.* Physical Review Letters, 2009. **103**(24): p. 246804.

179. Watcharinyanon, S., C. Virojanadara, J.R. Osiecki, A.A. Zakharov, R. Yakimova, R.I.G. Uhrberg, and L.I. Johansson, *Hydrogen intercalation of graphene grown on 6H-SiC(0001).* Surface Science, 2011. **605**(17–18): p. 1662-1668.

180. Emtsev, K.V., A. Bostwick, K. Horn, J. Jobst, G.L. Kellogg, L. Ley, J.L. McChesney, T. Ohta, S.A. Reshanov, J. Rohrl, E. Rotenberg, A.K. Schmid, D. Waldmann, H.B. Weber, and T. Seyller, *Towards wafer-size graphene layers by atmospheric pressure graphitization of silicon carbide.* Nat Mater, 2009. **8**(3): p. 203-207.

181. Tanabe, S., M. Takamura, Y. Harada, H. Kageshima, and H. Hibino, *Quantum Hall Effect and Carrier Scattering in Quasi-Free-Standing Monolayer Graphene.* Applied Physics Express. **5**(Copyright (c) 2012 The Japan Society of Applied Physics): p. 125101.

182. Mattevi, C., H. Kim, and M. Chhowalla, *A review of chemical vapour deposition of graphene on copper.* Journal of Materials Chemistry, 2011. **21**(10): p. 3324-3334.

183. Hamilton, J.C. and J.M. Blakely, *Carbon segregation to single crystal surfaces of Pt, Pd and Co.* Surface Science, 1980. **91**(1): p. 199-217.

184. Shelton, J.C., H.R. Patil, and J.M. Blakely, *Equilibrium segregation of carbon to a nickel (111) surface: A surface phase transition.* Surface Science, 1974. **43**(2): p. 493-520.

185. Morgan, A.E. and G.A. Somorjai, *Low energy electron diffraction studies of gas adsorption on the platinum (100) single crystal surface.* Surface Science, 1968. **12**(3): p. 405-425.

186. Land, T.A., T. Michely, R.J. Behm, J.C. Hemminger, and G. Comsa, *STM investigation of single layer graphite structures produced on Pt(111) by hydrocarbon decomposition.* Surface Science, 1992. **264**(3): p. 261-270.

187. Sutter, P.W., J.-I. Flege, and E.A. Sutter, *Epitaxial graphene on ruthenium.* Nat Mater, 2008. **7**(5): p. 406-411.

188. Tanaka, T., A. Itoh, K. Yamashita, E. Rokuta, and C. Oshima, *Heteroepitaxial System of h-BN/Monolayer Graphene on Ni(111).* Surface Review and Letters, 2003. **10**(04): p. 697-703.

189. Oznuluer, T., E. Pince, E.O. Polat, O. Balci, O. Salihoglu, and C. Kocabas, *Synthesis of graphene on gold.* Applied Physics Letters, 2011. **98**(18): p. 183101-3.

190. Imamura, G. and K. Saiki, *Synthesis of Nitrogen-Doped Graphene on Pt(111) by Chemical Vapor Deposition.* The Journal of Physical Chemistry C, 2011. **115**(20): p. 10000-10005.

191. Li, X., W. Cai, J. An, S. Kim, J. Nah, D. Yang, R. Piner, A. Velamakanni, I. Jung, E. Tutuc, S.K. Banerjee, L. Colombo, and R.S. Ruoff, *Large-Area Synthesis of High-Quality and Uniform Graphene Films on Copper Foils.* Science, 2009. **324**(5932): p. 1312-1314.

192. Miniussi, E., M. Pozzo, A. Baraldi, E. Vesselli, R.R. Zhan, G. Comelli, T.O. Menteş, M.A. Niño, A. Locatelli, S. Lizzit, and D. Alfè, *Thermal Stability of Corrugated Epitaxial Graphene Grown on Re(0001).* Physical Review Letters, 2011. **106**(21): p. 216101.

193. Voloshina, E.N., Y.S. Dedkov, S. Torbrugge, A. Thissen, and M. Fonin, *Graphene on Rh(111): Scanning tunneling and atomic force microscopies studies.* Applied Physics Letters, 2012. **100**(24): p. 241606-4.

194. Kwon, S.-Y., C.V. Ciobanu, V. Petrova, V.B. Shenoy, J. Bareño, V. Gambin, I. Petrov, and S. Kodambaka, *Growth of Semiconducting Graphene on Palladium.* Nano Letters, 2009. **9**(12): p. 3985-3990.

195. Johann, C., T.N.D. Alpha, E. Martin, B. Carsten, W. Dirk, B. Niemma, J.M.z.H. Frank, G. Raoul van, P. Bene, and M. Thomas, *Growth of graphene on Ir(111).* New Journal of Physics, 2009. **11**(2): p. 023006.

196. Varykhalov, A. and O. Rader, *Graphene grown on Co(0001) films and islands: Electronic structure and its precise magnetization dependence.* Physical Review B, 2009. **80**(3): p. 035437.

197. Wintterlin, J. and M.L. Bocquet, *Graphene on metal surfaces.* Surface Science, 2009. **603**(10-12): p. 1841-1852.

198. Batzill, M., *The surface science of graphene: Metal interfaces, CVD synthesis, nanoribbons, chemical modifications, and defects.* Surface Science Reports, 2012. **67**(3–4): p. 83-115.

199. Addou, R., A. Dahal, P. Sutter, and M. Batzill, *Monolayer graphene growth on Ni(111) by low temperature chemical vapor deposition.* Applied Physics Letters, 2012. **100**(2): p. 021601-3.

200. Anna, M., G.N. Albert, and I.K. Esko, *The role of metal nanoparticles in the catalytic production of single-walled carbon nanotubes—a review.* Journal of Physics: Condensed Matter, 2003. **15**(42): p. S3011.

201. Sutter, P., C.V. Ciobanu, and E. Sutter, *Real-time microscopy of graphene growth on epitaxial metal films: role of template thickness and strain.* Small, 2012. **8**(14): p. 2250-7.

202. Wang, B., M.L. Bocquet, S. Marchini, S. Gunther, and J. Wintterlin, *Chemical origin of a graphene moire overlayer on Ru(0001).* Physical Chemistry Chemical Physics, 2008. **10**(24): p. 3530-3534.

203. Dedkov, Y.S., M. Fonin, U. R¸diger, and C. Laubschat, *Graphene-protected iron layer on Ni(111)*. Vol. 93. 2008: AIP. 022509.

204. Soldano, C., A. Mahmood, and E. Dujardin, *Production, properties and potential of graphene.* Carbon, 2010. **48**(8): p. 2127-2150.

205. Song, H.S., S.L. Li, H. Miyazaki, S. Sato, K. Hayashi, A. Yamada, N. Yokoyama, and K. Tsukagoshi, *Origin of the relatively low transport mobility of graphene grown through chemical vapor deposition.* Sci. Rep., 2012. **2**.

206. Zhou, H., W.J. Yu, L. Liu, R. Cheng, Y. Chen, X. Huang, Y. Liu, Y. Wang, Y. Huang, and X. Duan, *Chemical vapour deposition growth of large single crystals of monolayer and bilayer graphene.* Nat Commun, 2013. **4**.

207. Khomyakov, P.A., G. Giovannetti, P.C. Rusu, G. Brocks, J. van den Brink, and P.J. Kelly, *First-principles study of the interaction and charge transfer between graphene and metals.* Physical Review B, 2009. **79**(19): p. 195425.

208. Skriver, H.L. and N.M. Rosengaard, *Surface energy and work function of elemental metals.* Physical Review B, 1992. **46**(11): p. 7157-7168.

209. Giovannetti, G., P.A. Khomyakov, G. Brocks, V.M. Karpan, J. van den Brink, and P.J. Kelly, *Doping Graphene with Metal Contacts.* Physical Review Letters, 2008. **101**(2): p. 026803.

210. Sutter, P., M.S. Hybertsen, J.T. Sadowski, and E. Sutter, *Electronic Structure of Few-Layer Epitaxial Graphene on Ru(0001).* Nano Letters, 2009. **9**(7): p. 2654-2660.

211. Pletikosić, I., M. Kralj, P. Pervan, R. Brako, J. Coraux, A.T. N'Diaye, C. Busse, and T. Michely, *Dirac Cones and Minigaps for Graphene on Ir(111).* Physical Review Letters, 2009. **102**(5): p. 056808.

212. Fonin, M., *Spatial corrugation and bonding of single layer graphene on Rh(111)*, 2010: ArXiv e-print.

213. Vinogradov, N.A., K.A. Simonov, A.A. Zakharov, J.W. Wells, A.V. Generalov, A.S. Vinogradov, N. Martensson, and A.B. Preobrajenski, *Hole doping of graphene supported on Ir(111) by AlBr[sub 3].* Applied Physics Letters, 2013. **102**(6): p. 061601-5.

214. Homma, Y., Y. Kobayashi, T. Ogino, D. Takagi, R. Ito, Y.J. Jung, and P.M. Ajayan, *Role of Transition Metal Catalysts in Single-Walled Carbon Nanotube Growth in*

Chemical Vapor Deposition. The Journal of Physical Chemistry B, 2003. **107**(44): p. 12161-12164.

215. Senczyk, D., *Some polytypes of Fe7C3 carbides.* Phase Transitions, 1993. **43**(1-4): p. 153-156.

216. Xue, Y., B. Wu, Y. Guo, L. Huang, L. Jiang, J. Chen, D. Geng, Y. Liu, W. Hu, and G. Yu, *Synthesis of large-area, few-layer graphene on iron foil by chemical vapor deposition.* Nano Research, 2011. **4**(12): p. 1208-1214.

217. Vinogradov, N.A., A.A. Zakharov, V. Kocevski, J. Rusz, K.A. Simonov, O. Eriksson, A. Mikkelsen, E. Lundgren, A.S. Vinogradov, N. Mårtensson, and A.B. Preobrajenski, *Formation and Structure of Graphene Waves on Fe(110).* Physical Review Letters, 2012. **109**(2): p. 026101.

218. Woodruff, D.P. and T.A. Delchar, *Modern Techniques of Surface Science*1994: Cambridge University Press.

219. Hoffman, D., B. Singh, and J.H. Thomas, *Handbook of Vacuum Science and Technology*1997: Elsevier Science.

220. Lüth, H., *Solid Surfaces, Interfaces and Thin Films*2012: Springer London, Limited.

221. Bowers, B., *X-rays: their discovery and applications*1970: H.M.S.O.

222. Rousse, A., K.T. Phuoc, R. Shah, A. Pukhov, E. Lefebvre, V. Malka, S. Kiselev, F. Burgy, J.-P. Rousseau, D. Umstadter, and D. Hulin, *Production of a keV X-ray Beam from Synchrotron Radiation in Relativistic Laser-Plasma Interaction.* Physical Review Letters, 2004. **93**(13): p. 135005.

223. Seah, M.P. and W.A. Dench, *Quantitative electron spectroscopy of surfaces: A standard data base for electron inelastic mean free paths in solids.* Surface and Interface Analysis, 1979. **1**(1): p. 2-11.

224. Fuchs, M., R. Weingartner, A. Popp, Z. Major, S. Becker, J. Osterhoff, I. Cortrie, B. Zeitler, R. Horlein, G.D. Tsakiris, U. Schramm, T.P. Rowlands-Rees, S.M. Hooker, D. Habs, F. Krausz, S. Karsch, and F. Gruner, *Laser-driven soft-X-ray undulator source.* Nat Phys, 2009. **5**(11): p. 826-829.

225. Krause, M.O. and J.G. Ferreira, *K X-ray emission spectra of Mg and Al.* Journal of Physics B: Atomic and Molecular Physics, 1975. **8**(12): p. 2007-2014.

226. Andrea, D., *Probing the Electronic Structure of Complex Systems by ARPES.* Physica Scripta, 2004. **2004**(T109): p. 61.

227. Delchar, D.P.W.T.A., *Modern Techniques Of Surface Science (2nd Edition)*. Cambridge Solid State Science Series1994, Cambridge

228. SPECS, G. *Ultraviolet Source UVS 300*. 2013; Available from: http://www.specs.de/cms/front_content.php?idcat=121.

229. Willmott, P., *An Introduction to Synchrotron Radiation: Techniques and Applications*2011: Wiley.

230. Schott, G.A., *XI. On the electron theory of matter and on radiation.* Philosophical Magazine Series 6, 1907. **13**(74): p. 189-213.

231. Williams, R.H., G.P. Williams, C. Norris, M.R. Howells, and I.H. Munro, *Photoemission from gallium selenide using synchrotron radiation.* Journal of Physics C: Solid State Physics, 1974. **7**(2): p. L29.

232. MAXlab. *The MAX injector*. 2013; Available from: https://http://www.maxlab.lu.se/node/263.

233. ISA. *The 100MeV Microtron*. 2013; Available from: http://www.isa.au.dk/facilities/astrid/electrons/microtron.asp.

234. Weihreter, E., *Compact Synchrotron Light Sources*1996: World Scientific.

235. ISA. *ASTRID Technical Specification*. 2013; Available from: http://www.isa.au.dk/facilities/astrid/astrid-technical.asp.

236. MAXLab. *MAXII Technical Specifications*. 2013; Available from: https://http://www.maxlab.lu.se/node/277.

237. MAXLab. *MAXIII Technical Specifications*. 2013; Available from: https://http://www.maxlab.lu.se/node/276.

238. Sjöström, M., E. Wallén, M. Eriksson, and L.J. Lindgren, *The MAX III storage ring.* Nuclear Instruments and Methods in Physics Research Section A: Accelerators, Spectrometers, Detectors and Associated Equipment, 2009. **601**(3): p. 229-244.

239. Eriksson, M. *The MAXIV Synchrotron Light Source*. in *Proceedings of the 2nd International Particle Accelerator Conference*. 2011. San Sebastián, Spain.

240. Bianchi, M., *Electronic Structure and Electron Dynamics of the Topological Insulator Bi2Se3*, in *Department of Physics and Astronomy*2013, Aarhus University: Aarhus.

241. Jensen, B.N., S.M. Butorin, T. Kaurila, R. Nyholm, and L.I. Johansson, *Design and performance of a spherical grating monochromator used at MAX I.* Nuclear Instruments and Methods in Physics Research Section A: Accelerators, Spectrometers, Detectors and Associated Equipment, 1997. **394**(1–2): p. 243-250.

242. MAXlab. *Beamine I4 - Short Information*. 2013; Available from: https://http://www.maxlab.lu.se/beamlines/I4.

243. Nyholm, R., J.N. Andersen, U. Johansson, B.N. Jensen, and I. Lindau, *Beamline I311 at MAX-LAB: a VUV/soft X-ray undulator beamline for high resolution electron spectroscopy.* Nuclear Instruments and Methods in Physics Research Section A:

Accelerators, Spectrometers, Detectors and Associated Equipment, 2001. **467–468, Part 1**(0): p. 520-524.

244. MAXLab. *Beamline I311 Home*. 2013; Available from: https://http://www.maxlab.lu.se/beamlines/i311.

245. Schuegraf, K.K., *Handbook of thin-film deposition processes and techniques: principles, methods, equipment, and applications*1988: Noyes Publications.

246. Venables, J.A., G.D.T. Spiller, and M. Hanbucken, *Nucleation and growth of thin films.* Reports on Progress in Physics, 1984. **47**(4): p. 399.

247. Bauer, E., *Phänomenologische Theorie der Kristallabscheidung an Oberflächen. II.* Zeitschrift für Kristallographie - Crystalline Materials, 1958. **110**(1-6): p. 395-431.

248. Vossen, J.L. and W. Kern, *Thin Film Processes II*1991: Academic Press.

249. Wasa, K., M. Kitabatake, and H. Adachi, *Thin Film Materials Technology: Sputtering of Compound Materials*2004: Elsevier Science.

250. Swarbrick, J.C., J.B. Taylor, and J.N. O'Shea, *Electrospray deposition in vacuum.* Applied Surface Science, 2006. **252**(15): p. 5622-5626.

251. Forrest, S.R., *Ultrathin Organic Films Grown by Organic Molecular Beam Deposition and Related Techniques.* Chemical Reviews, 1997. **97**(6): p. 1793-1896.

252. Mattox, D.M., *Handbook of Physical Vapor Deposition (PVD) Processing*2010: Elsevier Science.

253. Rancourt, J.D., *Optical Thin Films: User Handbook*1996: SPIE Optical Engineering Press.

254. OMICRON. *EFM Evaporators*. 2013; Available from: http://preview.omicron.de/products/mbe_deposition/e_beam_evaporators/efm_2/media/efm_2_1.pdf.

255. Evans, S. and J.M. Thomas, *The Chemical Nature of Ion-Bombarded Carbon: A Photoelectron Spectroscopic Study of "Cleaned" Surfaces of Diamond and Graphite.* Proceedings of the Royal Society of London. A. Mathematical and Physical Sciences, 1977. **353**(1672): p. 103-120.

256. Rezek, B. and C.E. Nebel, *Electronic properties of plasma hydrogenated diamond surfaces: A microscopic study.* Diamond and Related Materials, 2006. **15**(9): p. 1374-1377.

257. Tectra. *The H-flux Atomic Hydrogen Source*. 2013; Available from: http://www.tectra.de/hydrogen.htm.

258. McFeely, F.R., S.P. Kowalczyk, L. Ley, R.G. Cavell, R.A. Pollak, and D.A. Shirley, *X-ray photoemission studies of diamond, graphite, and glassy carbon valence bands.* Physical Review B, 1974. **9**(12): p. 5268-5278.

259. G, T., Williams., *Monitoring in-situ processing of solid surfaces with real-time X-ray photoelectron spectroscopy*, in *Institute of Mathematics and Physics*2011, Aberystwyth University. p. 186.

260. Sque, S.J., R. Jones, and P.R. Briddon, *Structure, electronics, and interaction of hydrogen and oxygen on diamond surfaces.* Physical Review B, 2006. **73**(Copyright (C) 2010 The American Physical Society): p. 085313.

261. Speranza, G. and N. Laidani, *Measurement of the relative abundance of sp2 and sp3 hybridised atoms in carbon based materials by XPS: a critical approach. Part I.* Diamond and Related Materials, 2004. **13**(3): p. 445-450.

262. Allmers, T. and M. Donath, *Growth and morphology of thin Fe films on flat and vicinal Au(111): a comparative study.* New Journal of Physics, 2009. **11**(10): p. 103049.

263. An, B., L. Zhang, S. Fukuyama, and K. Yokogawa, *Growth and structural transition of Fe ultrathin films on Ni(111) investigated by LEED and STM.* Physical Review B, 2009. **79**(8): p. 085406.

264. Juan, A. and R. Hoffmann, *Hydrogen on the Fe(110) surface and near bulk bcc Fe vacancies: A comparative bonding study.* Surface Science, 1999. **421**(1–2): p. 1-16.

265. Young, M.B. and A.J. Slavin, *The adsorption of C2H4 on the Mo(110) surface and the evolution of the surface with temperature.* Surface Science, 1991. **245**(1–2): p. 56-64.

266. Varykhalov, A., J. Sanchez-Barriga, P. Hlawenka, O. Rader, *Massless Dirac fermions in epitaxial graphene on Fe(110)*, 2012: Arxiv e-print.

267. Varykhalov, A., D. Marchenko, J. Sánchez-Barriga, M.R. Scholz, B. Verberck, B. Trauzettel, T.O. Wehling, C. Carbone, and O. Rader, *Intact Dirac Cones at Broken Sublattice Symmetry: Photoemission Study of Graphene on Ni and Co.* Physical Review X, 2012. **2**(4): p. 041017.

268. Speranza, G. and N. Laidani, *Measurement of the relative abundance of sp2 and sp3 hybridised atoms in carbon-based materials by XPS: a critical approach. Part II.* Diamond and Related Materials, 2004. **13**(3): p. 451-458.